TOWARDS MRI-GUIDED CARDIOVASCULAR INTERVENTIONS

A Dissertation

Presented to

The Academic Faculty

By

Christina Elena Saikus

In Partial Fulfillment

of the Requirements for the Degree

Doctor of Philosophy in the

School of Biomedical Engineering

Georgia Institute of Technology / Emory University

Atlanta, Georgia

August 2011

TOWARDS MRI-GUIDED CARDIOVASCULAR INTERVENTIONS

Approved by:

Ajit P. Yoganathan, PhD
Department of Biomedical Engineering
Georgia Institute of Technology and Emory University

John N. Oshinski, PhD
Department of Biomedical Engineering
Georgia Institute of Technology and Emory University

Robert J. Lederman, MD
National Heart, Lung, and Blood Institute
National Institutes of Health

W. Robert Taylor, MD, PhD
Department of Biomedical Engineering
Georgia Institute of Technology and Emory University

Elliot R. McVeigh, PhD
Department of Biomedical Engineering
Johns Hopkins University

Date Approved: January 19, 2011

ACKNOWLEDGEMENTS

I am indebted to the many people who provided amazing opportunities and support throughout my graduate training.

My thesis committee members were all willing mentors and provided critical insight during this process in addition to serving as role models for their expertise and contributions in the fields of cardiovascular disease, biomedical engineering, and MRI. Dr. Yoganathan and my time in the CFM lab fostered a strong research foundation and work ethic while also providing continual guidance and support to pursue different research and professional opportunities. Dr. Lederman gave me the freedom to pursue a wide range of projects and continue my development as a physician scientist through the incredible experience at the NIH/NHLBI intramural research program. Dr. McVeigh's contributions in real-time cardiac MRI provided the foundation for much of this work and he continually offered important perspective and mentorship along the way. Dr. Oshinski stimulated much of my original interest in MRI when I first started in graduate school and was trying to ride a bike in the scanner and continued as a valuable member of my thesis committee. Dr. Taylor provided a critical view of this work from his clinical and research cardiology acumen which I can only hope to attain in addition to his tremendous mentorship to future MD/PhDs.

This work represents a part of a large collaborative effort that wouldn't have been possible without everyone at NHLBI, particularly in the Cardiovascular Interventions Program, LCE and Cardiovascular branches. Much time was spent with the "cleanroom" crew of Dr. Ozgur Kocaturk, Merdim Sonmez, Jamie Bell, Vincent Wu, and Ann Kim working on novel device ideas, creations and testing. Dr. Tony Faranesh constantly helped with all aspects of these research projects and most importantly reminded me the

importance of finishing this effort and providing a critical review of my work. Most of the pre-clinical experimental work presented was done with Drs. Kanishka Ratnayaka and Issi Barbash who served as tremendous clinical and research mentors. They were always willing help test devices out while tolerating my skepticism and commentary over the headsets during procedures. Drs. Michael Hansen and Andy Derbyshire readily shared their expertise about MRI, answered my many random imaging and scanner questions and really made the scanner feedback portion of this work possible. Drs. Peter Kellman, Doug Morris and Scott Chesnik never hesitated when I came with scanner or coil questions or trying to figure out how to build an electronic component I wanted to try. Kathy Lucas, Bill Schenke, and Victor Wright were critical to accomplishing the pre-clinical animal experiment aspect of this work. Laurie Grant and Annette Stine guided me through the clinic and the cath lab so I wouldn't completely forget everything I learned about medicine. Finally, Drs. Balaban and Arai and the many members of their groups were also valuable colleagues at NIH who provided valuable learning opportunities and additional demonstrations of strong research pursuits.

The Emory MD/PhD, Georgia Tech BME, and NIH GPP programs were instrumental in making this training possible by supporting me and working on all the logistics from the first time I walked into their offices when this was just an idea. Without their continual help in navigating this training path and supporting the pursuit of these unique opportunities, this would have never been possible.

Finally, outside of lab, friends and family have always been there to help me keep going along this long training path. This work is dedicated to my parents who always supported all of my academic pursuits and worked to make every opportunity available to me and my brother.

TABLE OF CONTENTS

LIST OF TABLES

LIST OF FIGURES

LIST OF EQUATIONS

LIST OF ABBREVIATIONS

Abbreviation	Definition
ASD	Atrial septal defect
bSSFP	Balanced steady state free precession
CT	Computed Tomography
EP	Electrophysiology
FOV	Field of view
iCMR	Interventional cardiovascular magnetic resonance
LV	Left ventricle, or Left ventricular
MRI	Magnetic Resonance Imaging
MIP	Maximum intensity projection
PW	Pulse width
RF	Radiofrequency
RV	Right ventricle, or Right ventricular
SAR	Specific absorption rate
SNR	Signal to noise

TE	Echo time
TIPS	Transjugular intrahepatic portosystemic shunt
TR	Repetition time
VSD	Ventricular septal defect

LIST OF SYMBOLS

Symbol	Definition
ω	Angular frequency ($2\pi f$)
σ	Conductivity
ε	Dielectric constant
ρ	Density
Θ	Flip angle
γ	Gyromagnetic ratio
B_1	RF Amplitude
λ	Wavelength

SUMMARY

Imaging guidance may allow minimally invasive alternatives to open surgical exposure. The inherent vascular and soft-tissue contrast of MRI make it an appealing imaging modality to guide cardiovascular interventional procedures where traditional X-ray is inadequate (no soft-tissue guidance) or undesirable (ionizing radiation exposure in pediatric or prolonged procedures). Advances in real-time MRI have made MRI guided procedures a realistic possibility. The MR environment, however, introduces additional challenges to the development of compatible, conspicuous and safe devices. These technical challenges require careful preclinical evaluation of applications for feasibility and safety.

The overall goal of this work was to enable selected MRI-guided cardiovascular interventional procedures by creating and testing MR conspicuous devices. In the first part of this work, we describe the development and evaluation of actively visualized devices for three distinct MRI-guided interventional procedures. The active needle construction provided distinct tip localization and orientation and positioning of the needle shaft with unique imaging signatures. Device image performance was evaluated for signal profiles, contrast, and accuracy and size of the marker signals using methodologies developed for a more standardized evaluation. In one application, a loopless antenna incorporated into the delivery cable, with reduced material artifacts, provided greater operator confidence for proper cardiac occluder device deployment and positioning under MRI. In another application, MRI guidance using a configurable, actively visualized positioning and delivery system enabled MRI-guided transjugular intrahepatic portosystemic shunting with an excimer laser.

The second aim examined the potential heating associated with using conductive devices inside the MR environment, and how to monitor and improve the safety of these devices. Phantom testing demonstrated the relative importance of device positioning and the highly interrelated nature of these factors on device heating. Internal temperature monitoring allowed us to efficiently characterize device profiles and enable continual temperature monitoring during simulated procedures. Inner temperature measurements consistently exceeded external values. *In vivo* and *in situ* measurements demonstrated a 50% reduction of measured heating from blood flow and thermoregulation. We then incorporated this temperature monitoring approach into a system to monitor device safety and provide dynamic scanner feedback control in order further to assure safe device use.

In the final part of this work, we demonstrated the ability of MRI guidance combined with custom active devices to enable traditional and complex cardiovascular access. Reduced field of view imaging improved MRI-guided jugular access and workflow to enable procedures to be performed fully in the MR suite. The active needle decreased the time and needle passes necessary for successful access and image guidance helped less experienced operators achieve proficiency on par with more experienced ones. We also demonstrated more novel and complex cardiovascular procedures in transabdominal hepatic vascular access and transthoracic direct cardiac access, planning the trajectory and performing and monitoring the procedure using MRI guidance.

In summary, this work started with the device design, creation and testing, then addressed the safety of these devices, and finally employed these custom devices to develop and evaluate novel pre-clinical MRI-guided interventions. Together this

represents a comprehensive approach to help enable novel -guided cardiovascular interventional procedures.

CHAPTER

1

PROJECT OVERVIEW

1.1 Introduction

Magnetic resonance imaging (MRI) provides superior soft-tissue visualization and functional information without ionizing radiation exposure. Advances in real-time MRI provide such images with little latency and introduce the potential for MRI-guided interventions. Minimally-invasive cardiovascular procedures, to be performed as alternatives to surgery, are attractive but push the limits of X-ray guidance, particularly in treatments for structural heart disease, occluded or inaccessible vasculature, and electrophysiologic disorders. Real-time MRI offers unique imaging guidance for these interventions as well as greater procedural planning and evaluation.

Commercial devices typically used for procedures under X-ray, however, are largely incompatible in the MR environment or lack a distinct appearance during MR imaging. Compatible and clearly visualized devices must be developed to bring interventional cardiovascular MRI towards the clinical realm. With suitable devices in hand, clinically-relevant workflows and imaging approaches can be implemented in pre-clinical investigations to evaluate the feasibility and performance of MRI-guided procedures.

1.2 Overview

*We **hypothesized*** that MRI guidance coupled with clearly visible devices can provide the operator with greater information to perform routine and complex cardiovascular procedures using endovascular or minimally-invasive approaches. Our ***long-term aim*** is to enable clinical implementation of interventional cardiovascular MRI in suitable target applications. In this work, our ***objective*** was to develop and safely to employ uniquely visualized devices and imaging techniques for select MRI-guided cardiovascular interventions.

1.3 Specific Aims

The objective of this proposal was completed through the following *specific aims*:

SA 1: <u>Develop and Evaluate Clearly Visualized Devices for MRI-Guided Cardiovascular Interventions</u>

To facilitate MRI-guided interventions, we developed devices with embedded radiofrequency coils or antennas which provide unique imaging device signatures under MRI. Loop and loopless coils were incorporated into device designs and construction to permit desired MRI visualization while maintaining necessary mechanical and operating characteristics for the procedure. Device performance was evaluated first *in vitro* and then *in vivo* during iterative deployment in pre-clinical feasibility experiments of MRI-guided cardiovascular interventions such as percutaneous access, vascular interventions, and cardiac device placement.

SA 2: <u>Examine Device and Operating Factors for Interventional MRI Safety and Implement Improved Testing and Monitoring with Scanner Feedback Control to Enhance Safety</u>

In this aim, we examined the factors influencing radiofrequency induced heating in complex devices to develop appropriate device and operational considerations. Phantom testing looked at factors such as system components, placement in the phantom and scanner, and imaging parameters. To gain a better understanding of safety during realistic use and contributions of perfusion, we assessed device heating during *in vivo* and *in situ* animal studies with minimal device modification to allow real-time temperature monitoring. This knowledge helped to create more realistic device testing protocols, determine suitable

device and working parameters, and ultimately develop a safety monitoring and control system.

SA 3: Combine Conspicuous Devices and Procedure Development in an Important Preclinical Application: Real-Time MRI-Guided Cardiovascular Access

We developed an imaging and procedural approach for real-time MRI-guided vascular access using reduced field of view imaging to permit interventions to be performed wholly in the interventional MR suite. Outcomes of procedure efficiency were used to compare actively and passively visualized needles and varied operator experience during jugular vein access in swine. We also pursued targeted approaches to important alternative cardiovascular access routes such as percutaneous transabdominal hepatic vascular access and transthoracic direct cardiac access under MRI guidance in pre-clinical animal experiments.

CHAPTER

2

BACKGROUND[1]

2.1 Image-guided cardiovascular interventions

Reduced invasiveness in mechanical therapies is intended to reduce the danger and morbidity of surgical access and exposure, yet accomplish the objectives of surgical interventions. These ongoing trends could enable earlier evaluation and subsequent intervention to help reduce patient morbidity and mortality.

Image guidance for cardiovascular procedures began in the early to mid-1900s to gather new anatomic and physiologic cardiovascular data when X-ray was first used for confirmation and guidance of cardiac diagnostic catheterizations (1). X-ray helped operators to guide devices such as guidewires and catheters to the heart first for physiological (hemodynamic) and anatomic (angiographic) diagnosis and then later for treatment using angioplasty, stenting, and other endovascular procedures. Today, diagnostic cardiac catheterizations are routinely performed to gather anatomic and physiological cardiovascular information and many catheter-based interventions are available. The patient is subjected, however, to renal toxic dye, while the patient and staff are both exposed to ionizing radiation.

---

[1] *Selections published in Saikus and Lederman, Interventional Cardiovascular Magnetic Resonance (iCMR): A New Opportunity for Image-Guided Interventions JACC Imag 2009, 2: 1321-1331.*

In addition to coronary and peripheral artery interventional procedures, treating more complex conditions like aortic aneurysm disease, valvular disease, and other congenital and structural cardiac abnormalities has now become part of some interventionists' repertoire. For many of these procedures, X-ray fails to provide adequate visualization of target structures, monitoring of procedural steps and evaluation of outcomes. While X-ray angiography provides high temporal and spatial resolution, it is limited to projection views of vessels or cardiac chambers filled with radio-opaque dye, providing little information on critical 3D orientation and relationships of soft-tissue entities. Structures of interest like myocardial tissue, valves, or inaccessible or occluded vessels remain nearly invisible.

To further pursue such procedures with minimally invasive techniques, alternative visualization of these anatomic structures and physiologic information is necessary to replace surgical exposure. Substitute imaging technologies can help to determine appropriate treatment strategies and provide adequate guidance and monitoring to the operator throughout the procedure.

2.2 Magnetic Resonance Imaging

Magnetic resonance imaging (MRI) provides a unique combination of excellent soft-tissue contrast, multi-planar views, and functional monitoring capabilities without the ionizing radiation exposure associated with X-ray and CT. Clinical MRI is still a relatively young imaging modality but is widely deployed for diagnostic imaging. MRI has become the imaging method of choice for many orthopedic soft tissue conditions and the diagnosis and monitoring of neurologic diseases.

Cardiac MRI can provide a comprehensive examination of cardiac structure, functional parameters such as wall motion, blood flow, myocardial scar, and tissue perfusion (2). In addition, vascular MR imaging with time-of-flight angiography can delineate blood vessels without gadolinium-based contrast agents. Gadolinium can be administered to provide improved contrast-enhanced angiograms. Unlike more static targets imaged for orthopedic or neurologic applications, cardiac and respiratory motion presents an additional challenge for imaging in the thoracic cavity.

MRI primarily produces its signal from the behavior of hydrogen protons in response to their local electromagnetic environment. Multispectral MR imaging is possible using other resonant nuclei such as sodium or fluorine but far less commonly used due to lower available signal levels and specialized hardware requirements. The high static magnetic field, B0, is typically produced by a superconducting electromagnet at strengths of 1 Telsa (T), or 10,000 Gauss (Earth's magnetic field <1 Gauss, standard refrigerator or iron magnet ~ 50-100 Gauss). Permanent magnets are used in some systems under 1 Telsa, such as open-magnet configurations, but most clinical scanners are closed-bore 1.5T or 3T systems. The high magnetic field produces a net magnetic moment when the small hydrogen nuclei act as magnetic dipoles and align with the field typically oriented along longitudinal plane, usually the long-axis of the scanner.

An electromagnetic transmit coil is use to generate a magnetic field, B1, perpendicular to B0 and deposit radiofrequency energy to excite the nuclei and tip the magnetization off the longitudinal axis. The protons tipped toward the transverse plane precess, or rotate, at the Larmour frequency (64 MHz for hydrogen in 1.5T) inducing a current in receiver coils which eventually provides the MR signal. Since B0 is not completely homogeneous and there are spin-spin interactions, there is a loss of phase coherence in the precessing protons so the signal is referred to as a free induction

decay (FID) and loss of the signal typically described by T2 or T2* decay time constants. Eventually, the spins will tend to recover to their initial position aligned along B0, a process known as relaxation and often measured by T1, or recovery of longitudinal magnetization.

To localize the signal in space and create an image, gradient coils are used to provide magnetic field gradients along the in-plane and slice-select orientations. Slice selection generally employs a gradient applied during the RF pulse to selectively excite that slice for two-dimensional acquisitions and allows arbitrary slice positioning. In-plane localization is typically provided by frequency and phase encoding in the different directions. Frequency-encoding utilizes the application of a gradient which causes the protons to precess at slightly different frequencies depending on the net field they experience at their individual spatial locations. Phase-encoding alters the phase of the protons with higher gradients producing larger defined shifts in phase coherence. Multiple phase-encoding steps are necessary for localization in the second direction. This data is collected in k-space where each point encompasses the signal from the entire image field under a given gradient field condition. This can be converted into image space with an inverse Fourier transformation to produce the final MR image.

2.3 Real-time MRI

While most cardiac MRI involves gated examinations to isolate or resolve cardiac or respiratory motion and to enhance signal-to-noise, real-time MRI is of interest for patients with irregular rhythms where gating may not be feasible or for rapid imaging necessary to guide invasive procedures. Accurate image acquisition, reconstruction, and display with overall short latency times is not a simple feat in MRI but critical for

guiding interventions in real-time. Steady-state free precession (SSFP, often referred to as TrueFISP, FIESTA, FFE) is commonly used in cine cardiac imaging and during real-time iCMR procedures due to its excellent blood to tissue myocardial contrast and potential high temporal resolution. Parallel imaging with multiple receiver coils and associated reconstruction to appropriately combine the information from each coil (3-5) has enabled rapid imaging acquisition for cardiac and real-time imaging. Coupled with advances in computing power using multiple processors for efficient reconstruction of imaging data, real-time MRI is available with image display updates at 10 frames per second. Other imaging operations such as myocardial tagging and blood flow visualization are also possible in real-time.

Custom real-time MRI interfaces reconstruct and display these images and accommodate interventional procedures (6,7). Multiple slices can be acquired and 3D viewers can provide the operator relative location and orientation of the different views. Prior MR imaging can also be incorporated with individual slices, cine acquisitions, or MR angiograms serving as roadmaps within the real-time display to complement the constantly updating views. Several scanner manufacturers also have begun to implement their own commercial interfaces. Foot pedals and other remote controls have been employed to give the in-room interventionist control over imaging planes but most interventional MRI procedures currently require a second scan operator to alter other image acquisition parameters.

Using cross-sectional rather than projection imaging techniques, quickly locating a structure or device can be more difficult if part or all of the device is out of plane. X-ray operators are accustomed to projection views where the entire anatomy or device is visible in the field of view irrespective of its position in the third direction. Independent coloring of multiple active device channels and device-only projection views help indicate

device position (6). Several additional algorithms to quickly locate and display active MR devices and their 3D positioning and automatically update scan parameters have been developed to facilitate this aspect of iMRI procedures (8-10). Projection tracking approaches may also help further clarify passive device positioning (11).

2.4 Interventional Cardiovascular MRI (iCMR)

iCMR aims to leverage the advantages of MR imaging to enable routine and complex cardiovascular interventions with greater anatomic information and without ionizing radiation exposure. There are numerous applications for cardiovascular medicine (catheter-based endovascular, structural heart disease, surgery, pediatrics and electrophysiology) where MRI-guided procedures could have a significant impact in the near-term.

2.4.1 Catheter-Based Endovascular Interventions

MRI offers one of the few available means to image vessel lumen and wall features in addition to the vascular tree and branching using intrinsic contrast mechanisms. Interest in atheroimaging to evaluate vessel morphology and plaque characteristics fueled much of the early work in iCMR. Kantor et al. first described internal receiver coils for high-resolution intracardiac 31P NMR (12). Others soon developed local endovascular coils aimed to image arterial wall composition with improved SNR and resolution (13,14). Flow and motion, however, still remain significant challenges to high-resolution MR vessel images with realistic scan times *in vivo*.

Vascular interventions such as angioplasty and stenting under MRI can reduce radiation and iodinated contrast exposure compared to X-ray procedures and may allow unique monitoring for serious complications such as vessel wall dissection or perforation. Despite a dearth of commercial devices, numerous endovascular procedures have been pursued in pre-clinical studies and select clinical implementations. Coronary catheterization and stenting have been performed under MRI guidance in healthy animals (15-17), but clinical MRI lacks sufficient spatial or temporal resolution to guide meaningful coronary interventional procedures.

Larger peripheral vessels such as aorta and iliac arteries are more suitable targets for MRI-guided procedures. Iliac angioplasty and stenting was performed in early human studies by Manke et al. (18). Renal artery stenting has been conducted solely under MRI in an animal renal stenosis (19). MRI-directed tubular endografts have repaired porcine abdominal aortic aneurysms (20), porcine thoracic aortic dissection (21) after distinguishing true- and false-lumens; and stent angioplasty for aortic coarctation (22). A clinical pilot study successfully demonstrated MRI-assisted angioplasty for aortic coarctation in combination with X-ray (23).

2.4.2 Beyond the Vessels

MRI could allow catheter-based procedures to escape the traditional confines of vascular lumens. Completely occluded vessel segments, such as in chronic total occlusions (CTO), are virtually invisible in x-ray angiography where contrast cannot enter the obstructed lumen. MRI guidance will identify the mural contour of the occluded vessel and help guide recanalization while avoiding perforation. Recanalization of an animal model carotid CTO using a custom active MRI device was significantly more

successful than X-ray guided alternatives (24). Newer devices are being developed that clearly indicate the device position during recanalization (25).

Extra-anatomic bypass, directly connecting two otherwise unconnected vascular structures, is a unique application that might be performed without surgery because of MRI guidance. In a hybrid X-ray/MR approach to transjugular intrahepatic portosystemic shunt (TIPS) procedures, MRI helped reduce the number of needle passes needed to connect the hepatic to portal vein within the liver (26). Mesocaval puncture is an alternative portocaval trajectory enabled by MRI and custom-designed needle devices (27). A non-surgical Blalock-Taussig subclavian-pulmonary shunt is a tantalizing potential application of this technology.

MRI display of critical anatomy may have value for structural heart disease interventions. MRI has guided needle (28) and laser (29) atrial septal puncture and delivery of nitinol closure devices for atrial septal defects (30-32) in swine. MRI may enhance positioning (with regard to myocardial fibrous skeleton and coronary arteries) of transcatheter (33) and transapical (34) aortic valve implants in swine, and allows immediate evaluation of valve performance and flow. Hybrid imaging guidance is under development using an adjacent “MRI-friendly” X-ray fluoroscope at the edge of the magnet (35).

The development of novel biologic treatments for cardiovascular disease will require accurate methods of delivery and following treatment. Procedures targeting soft-tissue structures like the myocardium for biopsy, local drug delivery, or future gene and cellular therapies are performed under X-ray with limited knowledge of the borders of cardiac chambers or contours of myocardial targets. MRI guidance provides not only tissue and device visualization for accurate targeting during delivery (36,37), but unique

MR contrast mechanisms and additional agents can be incorporated in treatments to track their distribution (38). In preclinical animal studies, several groups have demonstrated successful delivery of cell and gene products to myocardial targets (39-41).

2.4.3 Pediatrics

Pediatric patients have much to benefit from MR guided interventional procedures. Children with congenital heart disease often require multiple catheterizations to monitor physiological parameters and for treatment that might avoid or delay open heart surgery. Each interventional procedure, however, is offset by the risk for unobserved complications and possible long-term consequences from x-ray exposure. Children, already more susceptible to radiation exposure, often require protracted interventions, increasing potential risk for chromosomal abnormalities and carcinogenesis (42). For medical staff, occupational x-ray exposure risks malignancy and cataracts (43) while protective lead garments risk chronic orthopedic injury (44).

Diagnostic catheterizations and EP procedures have been performed in pediatric and adult patients with congenital heart disease using a CO_2-filled balloon-tip catheter for visualization in a combined MR/X-ray suite (45). MRI-guided catheterization has further provided more accurate assessment of total or split pulmonary vascular resistance in patients (46,47). Beyond diagnostics, MRI might enhance treatment of structural pathology in children and adults with congenital heart disease. Interventions for structural abnormalities such as ventricular septal defect (VSD) could benefit from improved visualization of the septal defect and close procedural monitoring. Preclinical MRI-guided pulmonary artery and valve stenting (48) suggests percutaneous pulmonary

valve replacement (49) might be feasible under MRI. Most recently, MRI-guided pulmonary valve balloon dilatation was reported with 2 clinical cases, one adult and one pediatric, using a passively visualized guidewire (50). Test occlusion of a Fontan repair fenestration under real-time MRI has also recently been demonstrated (51).

2.4.4 Electrophysiology

MRI might offer one-stop visualization of cardiac surfaces being mapped, monitoring of ablation, and assessment of ablation lesions. Compared with ablation under direct surgical exposure, catheter ablations of atrial fibrillation or ventricular-tachycardia are lengthy and complex, most likely because of inadequate targeting and visualization of ablation lesions. MRI might have value beyond the baseline roadmaps now widely imported into electroanatomic mapping systems (52). Of particular appeal is the ability to conduct MRI thermometry during myocardial ablation, to determine the spatial extent of thermal injury (53), or the ability to assess subacute injury by imaging edema or myocardial contrast enhancement (54,55). MR-compatible cardiac monitoring and ablation systems have made MRI-guided EP procedures possible (56-58). Recently, initial clinical feasibility of real-time MRI-guided EP studies with cardiac mapping was demonstrated in 2 patients (59).

2.5 Multi-modality Guidance

X-ray combined with MRI, referred to as coregistration or XFM (X-ray fused with MRI), overlays previously-acquired MR images to assist interventionists during difficult X-ray fluoroscopy procedures. In this way, procedures enjoy the wide array of X-ray

compatible catheter equipment and additional 3D information about target vascular structures afforded by prior MRI. This multi-modality approach has been used clinically in high-risk myocardial free wall biopsy (60). XFM also enabled targeted endomyocardial injections (61) and a complex repair of membranous ventricular septal defects (VSDs) with significantly decreased fluoroscopy times in pre-clinical animal studies (62). Clinical EP studies have long gleaned valuable information from this hybrid approach with MRI roadmaps in electroanatomic mapping systems (52).

2.6 Interventional MRI in Other Clinical Disciplines

Several other clinical disciplines have embraced interventional MRI to guide critical procedures. Most enjoy targets that are relatively accessible, immobile, or require short, straight needle devices. Neurosurgeons routinely use pre-procedural MRI with stereotactic frames for biopsies and resections; many conduct intraoperative MRI to guide, for example, tumor margins (63). Biopsy is also conducted under MRI for potential liver, breast, and prostate malignancies (64). Tumor cryo- and radiofrequency ablation benefit from MRI guidance which allows interactive thermal imaging (65). MRI also enhances orthopedic biopsies, injections and other therapies (66). Many of these applications have fueled additional development of local imaging coils and MR-compatible manipulators and robotics (67).

2.7 Interventional MRI Devices

The same mechanisms which provide the unique image contrast in MRI also make most devices commonly used in X-ray procedures either invisible or unacceptable

for use during iCMR procedures. Metallic cores or braiding present in many devices for pushability and torquability can cause imaging artifacts and potentially obscure entire anatomic areas. Purely polymer products aren't visible unless modified and often lack requisite mechanical performance. Many of the MRI-guided procedures described above have used custom devices since MR-compatible commercial device availability is limited. These interventional MRI devices are typically classified by the mechanism by which they are visualized in imaging and the need for connection to the scanner hardware: Passive, Semi-active, and Active. Figure 2.7.1 shows an example of the MR appearance for each of these different device visualization strategies which are described in more detailed below and summarized in Table 2.7.1.

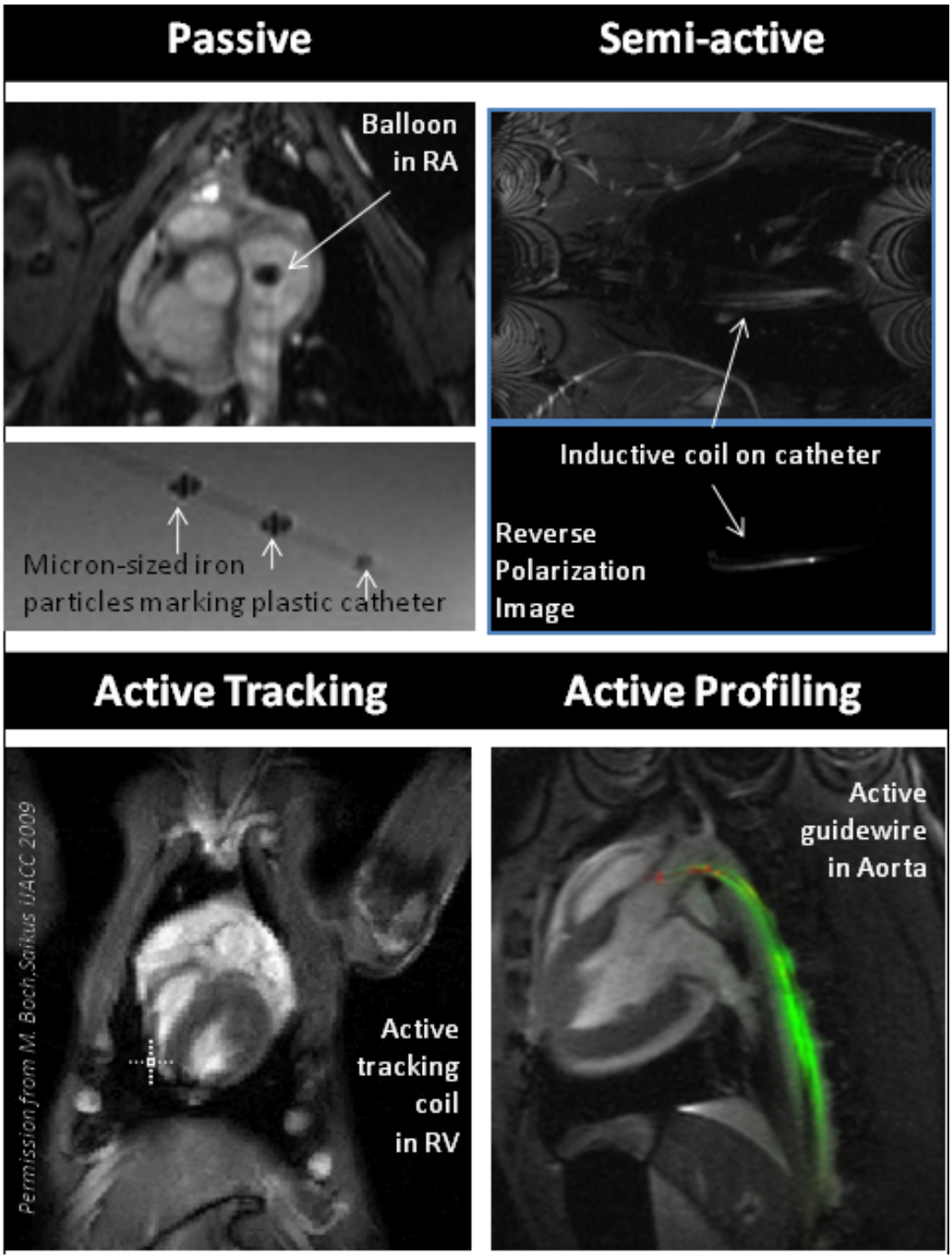

Figure 2.7.1 Device appearance in MRI with different visualization strategies: Passive, Semi-active, and Active Tracking and Profiling.

2.7.1 Passive Devices

Passive devices generally rely on material properties to visualize devices during MR imaging. Magnetic susceptibilities, or how the material responds to a magnetic field, of various materials can cause small regions of inhomogeneities in the main magnetic field producing signal voids appearing as dark regions on images and often referred to as negative contrast. Positive contrast can be generated using agents such as T1 shortening agents to alter the local signal which will appear brighter than it would otherwise. Many initial passive devices used polymer catheters with ferromagnetic (68) or paramagnetic coatings or rings (69,70) to produce negative or positive contrast, respectively. Other catheters with CO_2-filled balloons (71) or filled with more unique contrast agents such as 19-F (72) and hyperpolarized 13-C (73) with multi-spectral detection have also been explored. The length of these passive devices can be made visible by coating the entire device but a large portion of the catheter volume may be occupied by these fillers which are not always readily apparent. Off-resonance imaging techniques (74,75) is attractive to improve the specificity of the signal during imaging but can limit anatomic imaging. Recently, several groups have developed sophisticated non-metallic passive guidewires with specially formulated polymers and constructions such as micropultrusions to mimic the mechanical properties of their metallic X-ray counterparts with thin super paramagnetic iron oxide markings for visualization (76,77). These passive approaches avoid many of the RF safety concerns discussed below and often provide a simpler approach to device construction. A key limitation of these passive approaches, even using off-resonance imaging techniques, is uniquely identifying the device “signature” during imaging. Uncertainty about device position and orientation during MRI-guided procedures, is a critical limitation that impacts safety, effectiveness and acceptance.

2.7.2 Active Devices

Active devices for interventional MRI incorporate small coils or antennas on independent channels connected to the scanner for device tracking (78) or visualization to provide clear device identification. Device tracking requires special tracking sequences to locate the tracking coil in 3D space with the device position and path then marked on prior or interspersed images. Active device “imaging” or “profiling” enables unique visualization of the device profile on MR images acquired in real-time, in the specific context of surrounding anatomy. Many of the early coil designs for atheroimaging evolved into active devices such as catheters and guidewires with loop and loopless (79) antenna designs that could be uniquely visualized under MRI and used to facilitate iCMR procedures. It is challenging to incorporate the requisite electrical and mechanical components in appropriately-sized designs while maintaining the functionality operators expect.

2.7.3 Semi-Active Devices

Semi-active devices typically contain circuit elements such as inductively-coupled resonantors (position markers) that do not require long transmission lines or connection to the scanner but may be more visible than passive devices. Through mutual inductance the signal around the inductively-coupled coil can be picked up by the other receiver coils. These markers can be incorporated on the distal end of catheters (80,81) but the catheter appearance is then limited to this region. Further optical tuning (82,83)

or signal separation (84) techniques still may be required to firmly distinguish these devices from background tissue or artifact.

Table 2.7.1 Visualization Methods of Interventional MRI Devices (adapted from (85,86))

Approach	*Technology*	*Advantages*	*Disadvantages*	*Examples*
Passive markings	Visible based on intrinsic materials properties Negative contrast: local susceptibility of paramagnetic materials Positive contrast: coating with T1-shortening agents	Simple, inexpensive Can be used in combination with other approaches Can use imaging techniques ("white marker") to create positive contrast from negative Certain devices commercially available (needles)	Non-specific catheter "signatures" "Compatible" conductive wires can heat Must not contain ferrous braids Cannot automatically track the device	Gadolinium-filled balloon dilatation catheters. Non-braided angiography catheters Polymer guidewires(77)
Active "imaging", "profiling"	Incorporate MRI antennas Resonant RF coils attached directly to the scanner which can be visualized in normal real-time imaging	Highly conspicuous Catheters can be depicted in color Versatile imaging approaches including projection-mode	Complex, expensive Conductive wires can heat Blurry profile compared with X-ray catheters Dipole designs have poor distal tip visibility	Surgi-Vision *Intercept* 0.030" dipole guidewire coil Boston Scientific *MRI Stilletto* endomyocardial injection system
Active "tracking"	Incorporate MRI antennas Coil position determined with device tracking sequences for 3D location of coil	Simple, inexpensive Marker points can be tracked without imaging, to increase speed or reduce heating Marker points can be used to automate scan plane adjustments	No real-time MRI Requires specialized tracking sequences Catheter locations are computer-synthesized on image Conductive wires can heat	MGH / General Electric electroanatomic mapping and MRI system (87)
Inductive-coupling	Resonant RF coil coupled to other receiver coils	Requires no physical connection Reverse polarization mode may display unique device signature	Embeds electronics that might interfere with mechanical performance (*i.e.* on stents) Low flip angle compromises imaging	Essen wireless stents (88) and catheters (81)
Direct currents	Direct current in coil creates controllable field distortion	Simple Controlled artifacts confer specificity	No imaging Heating of transmission lines when employed	Fiberoptic-detuned tracking coil (82)
Multispectral devices	Coatings with materials incorporating other nuclei that can be imaged and identified in MRI	Non-proton MRI species can be displayed in different colors from target tissue Passive imaging that does not require transmission lines or embedded electronics	Additional hardware required for exciting and detecting the alternate compounds Hyperpolarized ^{13}C requires constant replenishment using specialized generator hardware	^{19}F catheter tracking (72) ^{13}C catheter tracking (73)

2.8 MRI Safety

Each of the electromagnetic fields that enable MR imaging must be considered to avoid potential safety risks for procedures and medical devices in the interventional MRI environment. The static magnetic field (B0) can exert tremendous force and torque on ferromagnetic objects, drawing them into the bore (89). As a result, instruments, monitoring equipment, and other implements used near MRI scanners must be non-magnetic or properly labeled and secured to avoid creating dangerous projectiles in the room. Thorough patient screening is a critical component to ensure MRI safety and exclude patients that have embedded metal from older implants or exposure to metal filings or shrapnel that may be subject to these forces or experience increase RF deposition and heating. The impact of exposure to high magnetic fields, particularly regular exposure for staff, has also been debated (90).

Magnetic field gradients (Gx, Gy, and Gz) for spin localization and the pulsed electromagnetic RF field (B1) used to flip the spins down to the transverse plane produce rapidly changing electromagnetic fields. Conductive loops oriented perpendicular to pulsed or changing magnetic fields can develop induced currents according to Faraday's law of electromagnetic induction and produce resistive, or Joule, heating. The induced voltage from the time-varying magnetic flux increases with increasing loop area, number of loops, and rate of change and strength of the magnetic field (Equation 2.8.1).

Equation 2.8.1. Induced voltage on a conductor loop in a changing magnetic field

$$\boldsymbol{V = -N\frac{\Delta(BA)}{\Delta t}}$$

V = induced voltage
N = number of turns
B = magnetic field
A = area of coil

Reducing or avoiding induction loop heating is a main rationale behind recommendations for patients to avoid crossing arms or legs and for staff to assure cables for coils or ECG monitoring do not form loops (91). A resonant loop can further contribute to the heating observed (92). Non-looped conductors also can experience eddy current formation which produces an opposing magnetic field in accordance with Lenz's law in addition to inductive heating. Current formation increases with increasing applied field strengths, conductivity of conductors, and rate of changes of the magnetic field.

Physiologically, the rapid application and switching of magnetic field gradients are most commonly associated with patient nerve stimulation which limits the applicable slew rate, or rate at which they reach their final value (93). Cardiac stimulation is possible but the threshold is much higher. Acoustic noise generated by vibration of these gradient coils and nearby metallic structures can be reasonably overcome through the use of hearing protection and MR-compatible communication systems. The applied high RF transmit power may cause tissue heating due to the induced eddy currents in the body (94). The RF energy is primarily absorbed at the surface where tissue heating potential would be highest and minimal towards the center (95). Specific absorption rate (SAR) is the measure typically used to describe the RF power deposited to a mass of tissue (in watts/kilogram) and is usually given for whole-body average measurements (WB-SAR) but power can locally focused and deposited depending on the environment producing SAR hotspots. Power limitations and FDA guidance for MRI scanning and implant compatibility have traditionally considered temperature increases of 1°C in the head, 2°C in the trunk, and 3°C in the extremities to not have any expected adverse effects in people with normal thermoregulation. This is largely based on the normal daily temperature fluctuations, tolerable increases in core temperature and levels considered

for heat stroke (41°C) and local heating of >41°C that may cause tissue damage with extended (20 min – 1 hour) application (96).

Conductive implants and devices can focally concentrate the induced electric fields and cause local increases in current density and SAR with corresponding tissue or phantom heating (97). The production of standing waves can arise in devices with impedance mismatches with reflection at the transition points and constructive addition of the induced currents on the conductor. Devices with lengths near a half-wavelength may experience resonant effects and act as linear antennas, coupling with the parallel electric field and producing high induced potentials (Equation 2.8.2) and voltage dissipation near the device ends and/or interface transitions leading to local SAR hotspots and heating (92,98-100).

Equation 2.8.2. Induced voltage on a wire in an electric field.

$$V = \int_0^{\ell} \vec{E} \bullet d\vec{\ell}$$

V = induced voltage on wire
E = E field
ω = angular frequency
l = wire length

Several approaches for active devices and implants in MRI have targeted the electrical properties or effective electrical length of the transmission lines to reduce shield currents and standing waves seen at resonant lengths. High impedance cables can limit the degree of RF current supported. Quarter-wave coaxial chokes can incorporated into coaxial transmission lines to limit shield, or common-mode, currents by presenting a high impedance on the outer surface of the conductor without impacting the differential-mode signal (101). Alternatively to incorporating a choke into the cable itself, “floating” current traps tuned to the Larmour frequency can be used to minimize shield currents (102). Long dipole antennas utilize 1:1 baluns in accompanying circuitry to

produce a high-impedance for the shield currents. Transformers present yet another option to block unwanted shield currents by transmitting signal via inductive coupling and breaking up the cable into short non-resonant lengths (103) and have been recently incorporated into an active EP catheter with highly resistive wires for the ECG monitoring (104). Additional approaches explored include a Bazooka coil which also inductively couples the signal (105) and use of a Q-spoiling dielectric to reduce tip heating (106). Many of these approaches, however, have been difficult to incorporate in small devices or may cause heating in other device locations.

Replacing conductive transmission lines with optical fiber can avoid unwanted interactions between the cables and RF electric field. Optical connections have been used previously to selectively detune coils for better localization of inductively coupled signals (83). More recently, an optical transmission system for an active MRI device was developed with continued work to appropriately miniaturize the technology for use in clinically useful designs (107). Size restrictions, again, have limited deployment of these technologies for clinical devices.

2.9 Clinical Significance

Real-time MRI guidance could enhance cardiovascular procedures that are currently guided by different imaging modalities, and it could enable novel minimally invasive procedures. Prolonged x-ray exposure, such as during catheter repair of congenital heart defects, could be avoided. Procedures that currently require surgical exposure, such as extraanatomic vascular bypass, might be possible with a wholly catheter-based approach because of the soft-tissue imaging afforded by MRI. Imaging of tissue, rather than X-ray guided positioning with limited anatomic information, might enhance ablation therapy for cardiac rhythm disorders. Soft-tissue targets can be approached with percutaneous approaches with monitoring in multiple views and greater anatomic context not currently afforded by ultrasound. For these procedures ultimately to impact patient care, appropriate devices must be available and tested to ensure safety and performance and allow development and evaluation of these procedures in pre-clinical studies.

This work combined several critical elements to bring MRI-guided cardiovascular interventions closer to the clinical realm. This first aim tackled the unavailability of compatible devices for interventional MRI with unique signal profiles which are necessary to clearly locate and follow them in real-time MRI guided procedures. The development of devices for several different cardiovascular interventions demonstrated how different coil designs and visualization approaches can be leveraged to improve the visibility of devices and implants while maintaining the requisite handling for the procedure.

The second aim addressed MRI safety for active device design and use where long metallic components or conductors may experience radiofrequency induced heating

but studies of complex devices are limited. Heating studies in the second part of this work examined various factors influencing heating and more clinically realistic scenarios with correlates between phantom and *in vivo* testing in large animal models. This helped identify appropriate device and operating parameters to ultimately develop safety monitoring approaches for initial clinical testing.

The final aim addressed direct percutaneous vascular access inside the interventional MRI system, which would be an attractive alternative to access in the X-ray system followed by transfer to the MRI system and permit procedures to be performed completely in the MRI suite. In this aspect of the work, we provided the requisite devices, imaging and procedure approaches to enable a pre-clinical evaluation for MRI-guided vascular access in swine. To allow more complex minimally-invasive cardiovascular procedures, percutaneous transhepatic vascular access and direct transthoracic cardiac access were demonstrated in swine under MRI guidance for trajectory planning and procedural guidance with active devices.

CHAPTER

3

ACTIVE DEVICE DEVELOPMENT

3.1 Introduction

Most devices currently available for limited interventional MRI procedures are visualized passively. Typically they are visible as dark artifacts, or negative contrast, due to (a) water displacement, (b) the different magnetic susceptibilities relative to water, causing small local inhomogenities in the B0 static magnetic field, and (c) radiofrequency (RF) inhomogeneity (108). These devices can be difficult to clearly identify in imaging as other fluctuations in signal intensity, complex anatomic boundaries, and artifacts can show similar appearances, particularly in highly dynamic anatomies such as the heart.

Active devices aim to produce a unique imaging signature by incorporating small local coils or antennas connected to the scanner for device tracking (78) or visualization ("profiling"). While tracking can provide 3D device positioning, it is typically limited to small coil locations and requires tracking sequences interleaved with real-time anatomic imaging. Device visualization allows simultaneous display of device positioning and shape with real-time imaging and more closely represents the device appearance operators have in other modalities. Cross-sectional imaging techniques, in contrast to projection imaging, introduce additional device visualization requirements as the entire device profile may not always be in plane or visible.

Loop and loopless (79) coil constructions are used for internal coils and active visualization techniques which could be incorporated into active device design (Table 3.1.1). Loop coils like solenoids typically create more localized signal intensity profiles that fall off rapidly from the coil. Loopless designs which represent a half-dipole antenna can provide signal along linear devices but distal signal at the tip typically is limited. Combined coil implementations can provide the construction and signal profile advantages of both, but may be limited by coupling of the different channels.

Table 3.1.1. Loop and loopless antenna designs

	Loop	Loopless Ocali 1997
Antenna Correlate	Loop Antenna 	Half-wave dipole 
Signal profile	Usually discrete coil location	Can provide signal along length of device
Radial Sensitivity	$1/r^2$ - $1/r^4$	1/r
Construction/Size	Typically wire loop and transmission line 	Inner and outer conductor coaxial construction 
Detuning strategy	Parallel resonant circuit activated by PIN diode to produce high impedance	Quarter-wave transformation to junction from short at PIN diode

Compact coaxial constructions are possible with loopless constructions where the whip, or extended inner conductor, serves as one λ/4 pole of the antenna with the shield of the outer conductor serving as the other (Figure 3.1.1).

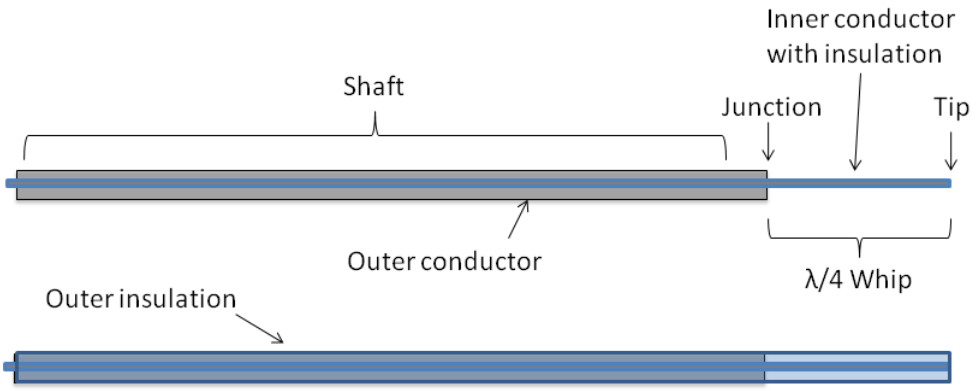

Figure 3.1.1. Schematic of loopless antenna design.

These coil designs represent the inductors in an RLC (resistor-inductor-capacitor) circuit tuned to resonate at 64 MHz to receive the signal from the local precessing protons and impedance matched for maximum power transfer and minimal reflection (Figure 3.1.2). Detuning during transmit occurs with high impedance across a capacitor gap in the loop coil and at the junction of a loopless design to prevent coupling to the transmit coil, induced current flow from the high applied power and local flip angle amplification.

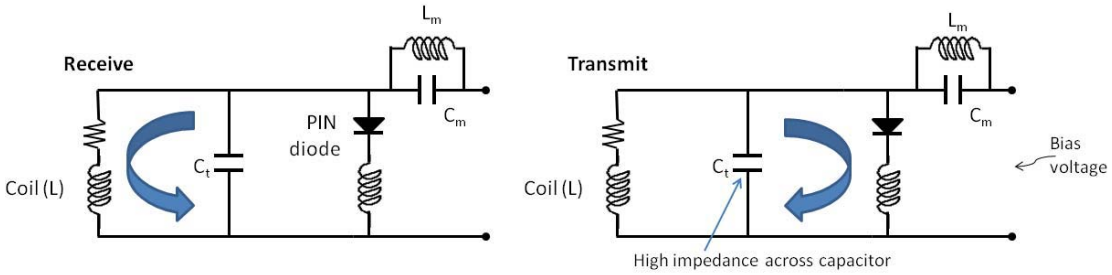

Figure 3.1.2. Representative RLC circuit with tune, match, and decoupling components.

Because device size limitations often preclude local tuning and matching of the coil on the device body itself, remote matching is usually employed but necessitates small transmission lines in the antenna construction which can negatively impact signal performance.

Active device visualization is also unique compared to X-ray devices where the device appearance comes from X-ray attenuation. The local coils in MRI devices receive their signal from their local environment and the device construction may also impact device and anatomic imaging.

Considerations for device visualization must be balanced with the mechanical properties necessary to accomplish the desire procedure. Device size cannot be dramatically increased to accommodate incorporated coils which would necessitate larger access and limit device positioning. Insulation is critical to protect the coils or separate components of the conductive structure. With the additional layers necessary for coil insulation, however, the device may become more rigid. Material type and thickness must also be selected to have adequate pushability for advancement, restoring force for deflection and appropriate torquability for rotation.

In this work, we developed actively visualized devices to enable pre-clinical feasibility studies of three MRI-guided cardiovascular interventional procedures. For MRI-guided percutaneous access, an active needle was needed to allow clear tip and tract localization. To facilitate cardiac occluder device delivery under MRI guidance, improved visibility of the device deployment was necessary. In evaluating the use of an excimer laser for extra-anatomic bypass such as TIPS, means to direct the laser and visualize curvature and trajectories were lacking. For each of these applications, we hypothesized that incorporating active visualization strategies in the device design could

provide the necessary device appearance for the given procedure while maintaining or enhancing the requisite mechanical performance. We also recognized that methods were necessary to evaluate the device imaging performance for a more systematic evaluation of device appearance under MRI which could impact procedure guidance.

3.2 Active Needle

For MRI-guided percutaneous procedures, specific tip location is critical as well as visualization along the needle. MRI-compatible needles are available in non-magnetic metal alloys which are visible under MR due to water displacement and the different magnetic susceptibilities of metals relative to water, causing small local inhomogenities in the B0 magnetic field, and radiofrequency (RF) inhomogeneity (108). Rapid identification of these needles can be difficult particularly in areas of variable signal intensity. For longer trajectories, identifying the angle and positioning of the needle is also challenging.

Instantaneous knowledge of needle position angulation is critically important in cardiovascular applications. Cardiovascular access typically also utilizes a needle with unobstructed lumen to allow bleed-back to confirm access and guidewire passage for sheath exchange. For smooth advancement through the skin and soft-tissue during access, the needle construction must be robust. To facilitate MRI-guided cardiovascular access, we developed an “active” MRI antenna-needle with an open-lumen, distinct tip appearance and indicators of depth and trajectory, for enhanced MRI visibility. We then evaluated the device imaging appearance with regards to tip localization and shaft marker accuracy.

3.2.1 Methods

Active Needle Design and Construction

The needle design aimed to incorporate active profiling to delineate the tip clearly while maintaining the desired mechanical properties (size, open-lumen, smooth

advancement) to allow the device to be used *in vivo* for cardiovascular applications. An 18-gauge MRI-compatible needle base, initially a commercially available 15cm *Inconel* 625 needle (EZ-EM, Lake Success, NY USA) and then a custom ground Nitinol needle, was modified to incorporate a loop antenna along its length. In order to create a unique device "signature" appearance, areas of greatest signal intensity were produced with tighter copper wire (0.003" coated wire, California Fine Wire, Grover Beach, CA) coil windings around the insulated needle separated by **unequal** distances, starting just proximal to the tip (at the end of the bevel) and at 1, 3, 6, 10 and 15 cm away to provide distinguishable marker points. Thermoplastic elastomer (*Pebax*) covering maintained a smooth transition on the outer surface from needle bevel to coil without a significant increase in outer diameter (<5Fr, 1.67mm) to allow smooth skin entry as seen in Figure 3.2.1.

Figure 3.2.1. Active needle with close up of tip uncovered (A) and covered (B). Needle with coaxial extension and circuit box seen in (C).

To allow its free movement, the needle was connected initially to its remote tuning and matching circuitry via a 1-meter long coaxial cable extension. The needle was impedance matched to 50 ohms at 63.67 MHz (Larmor frequency for 1.5T) for maximum power transfer, used in receive-only mode, and detuned during RF transmission with a

PIN diode and parallel resonant circuit to limit coupling with the high power RF transmit which may cause non-uniform excitation and potential device heating. To eliminate the small coaxial cable and place the circuitry immediately at the needle to improve signal quality, localize detuning circuitry to the end of the coil, and enable the use of a larger shielded and trapped cable proximally, a version of the needle with circuitry embedded in a handle was also produced (Figure 3.2.2).

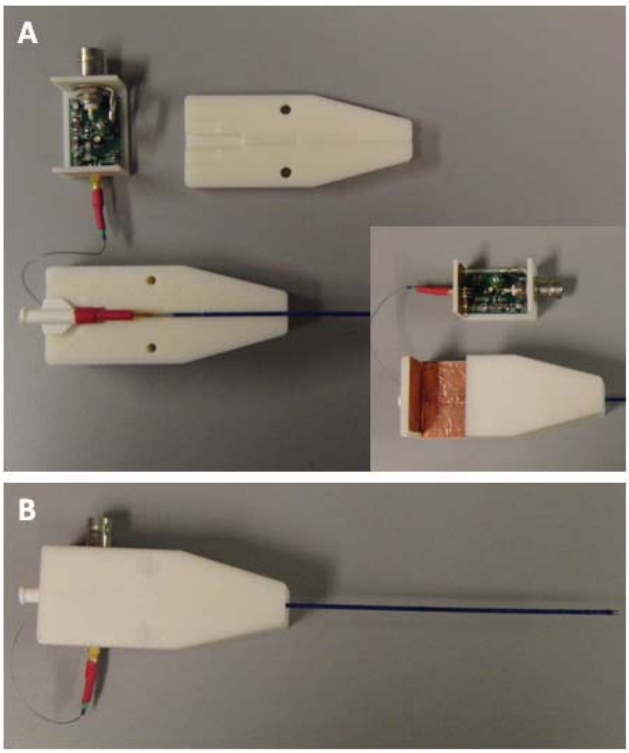

Figure 3.2.2. Active needle with circuitry in handle.

Imaging Evaluation

All imaging and interventional procedures were performed in a short, wide bore 1.5T MRI scanner (Espree, Siemens Medical Solutions, Erlangen, Germany) with

surface receive coils in addition to the independent active device channels. The active needle and associated active devices (such as active guidewires) were connected to separate scanner receiver channels via a preamplifier box. High resolution phantom images were acquired using 2D (TR/TE 3.92/1.96ms, flip angle 45º, field of view 340x170mm, matrix 256x128, slice thickness 5mm) and 3D (FOV 340x340, matrix 484x484, slab slice thickness 1mm, displayed as maximum intensity projection) balanced steady-state free precession (bSSFP) sequence. Real-time bSSFP imaging (TR/TE 3.67/1.23ms, slice thickness 6mm, flip angle 45°, matrix 192x144) used a separate real-time reconstruction and display system (6) and was performed during phantom testing and *in vivo* animal experiments. The active needle signal was displayed as a color overlay on the anatomical grayscale images in the real-time reconstruction system.

In Vitro Needle Imaging Characterization

In vitro testing was conducted in water phantoms under various conditions that may be experienced during *in vivo* use using the sequences described above. To evaluate needle appearance changes during different orientations with respect to B0, the needle was fixed in place at the proximal end within a rectangular phantom that could be aligned parallel and perpendicular to B0. Imaging was also performed with a stylet and guidewire occupying the device lumen test the possibility of signal cancellation or other unfavorable coupling.

Signal-to-noise (SNR) maps to examine the device signal profile were generated using a single magnitude image of the device only channel. The noise was calculated from a user-selected “noise-only” region outside the device and phantom and corrected

for the number of active channels (109,110). Contrast to background imaging was compared for the active needle with and without the active channel on with the device oriented parallel and perpendicular to B0. The minimum signal level was taken for the highest negative contrast value while the maximum signal level was used for positive contrast and compared to the average background signal.

To characterize the accuracy of coil visualization in determining needle location, we recorded coil marker appearance along the device and measured tip and centerline deviations. The device centerline and tip location were determined by fixing the needle in a custom plexiglass holder with small water channels providing MR visible distance markings (Figure 3.2.3).

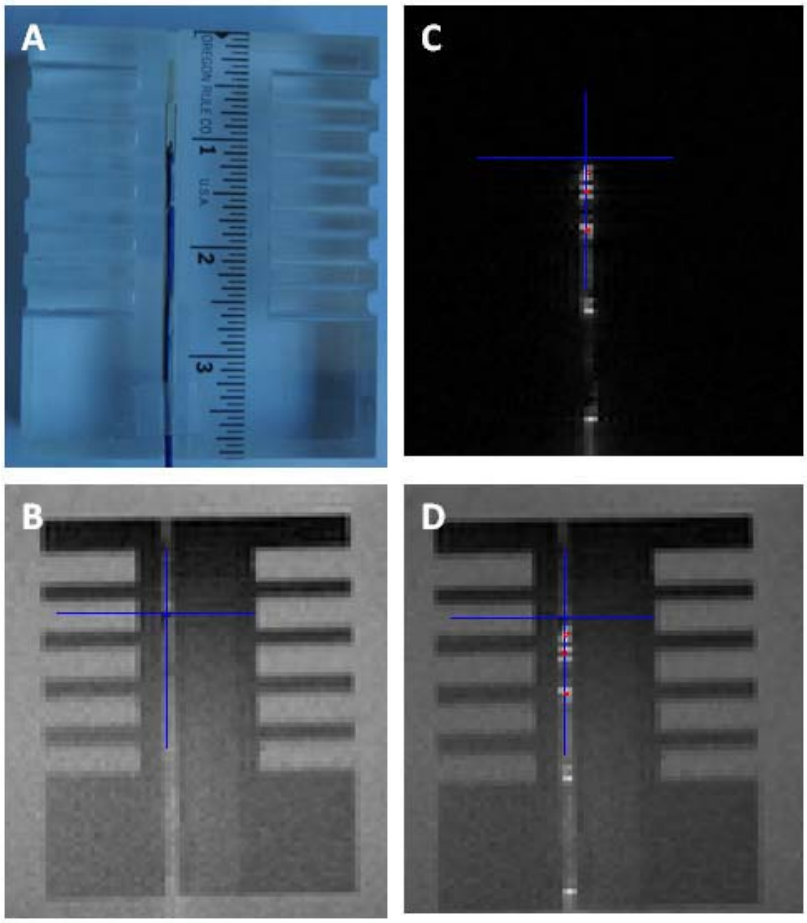

Figure 3.2.3. Device in holder with centerline and tip locations indicated by blue lines and centroids of coil signal in red.

Marker locations were determined by the centroid of the marker points after threshold segmentation (Figure 3.2.4). The differences between the set tip position and visible tip position and deviation of signal intensity at the tip from the device centerline were calculated. Signal widths also were measured for the marker points along the center of the marker point and characterized by the full width half maximum where the signal fell to 50% of the maximum level.

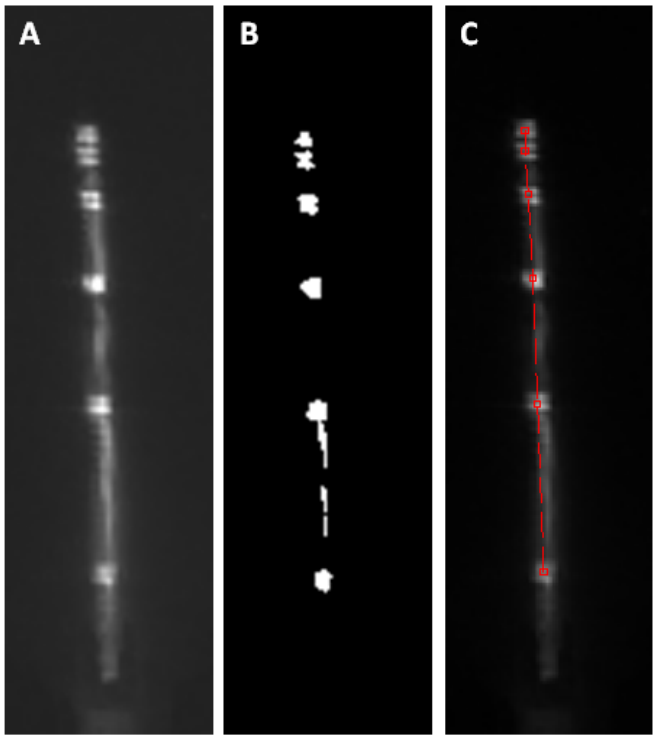

Figure 3.2.4. 3D maximum intensity projection image of needle signal (A) with thresholding (B) and centroid calculation (C) of marker points.

3.2.2 Results

Device Construction and Imaging Evaluation

Needle construction and circuitry produced distinct points of increased signal intensity in phantom images corresponding to the prescribed spacing along the length of the needle. A minimum spacing of 0.5 cm between tightly wound segments provided distinct markers that could be identified with the device parallel or perpendicular to B0. These points were visible despite changes in needle artifact size and appearance which is seen along with a SNR map in Figure 3.2.5. Maximum SNR values exceeded 100.

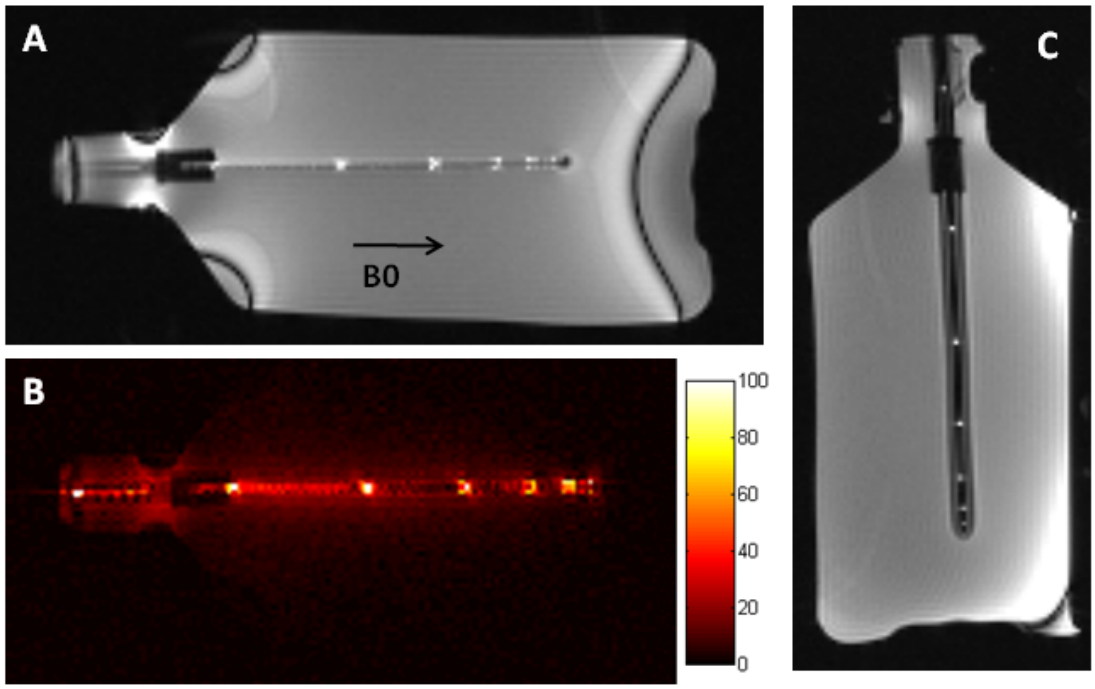

Figure 3.2.5. Active needle signal with parallel (A) and perpendicular (C) to B0. Device only SNR map shown in (B).

The signal from the needle was also apparent when the needle was used with an accompanying MR-compatible stylet, passive nitinol guidewire, and active guidewire which could displace the inner water and signal source (Figure 3.2.6).

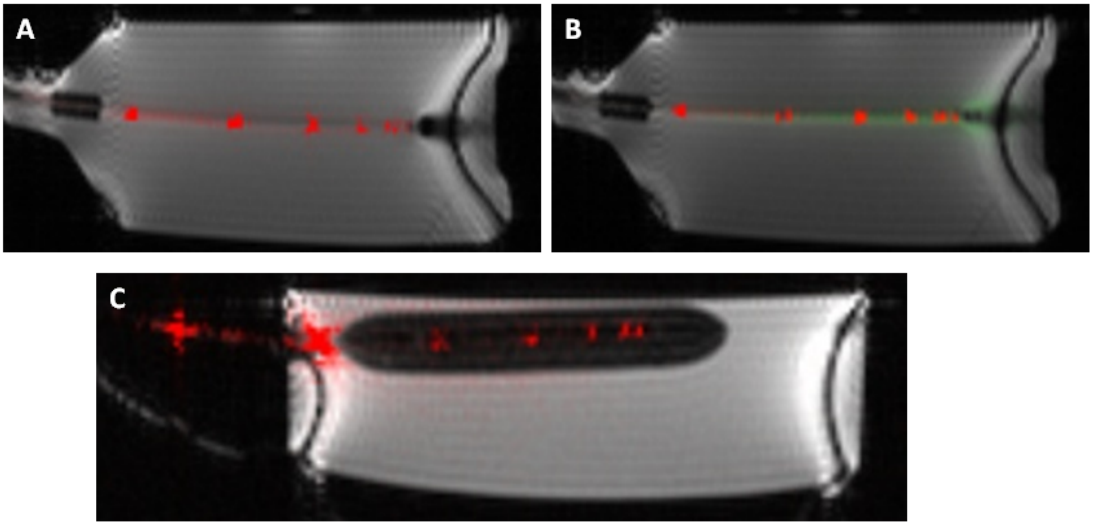

Figure 3.2.6. Active needle signal seen in red with nitinol stylet (A), active guidewire (B – wire in green), and simulated lower signal tissue with needle in a hot dog and gain turned up (C).

In the water phantom, the active signal provided 2 to 2.5-fold increase in signal compared to background. With the needle parallel to B0 and the device channel off, the passive artifact is very narrow and only produced a small decrease in signal. With the needle perpendicular to B0, the artifact is much broader and caused a decrease over 8-fold while the active signal had similar intensity (Figure 3.2.7 and Table 3.2.1).

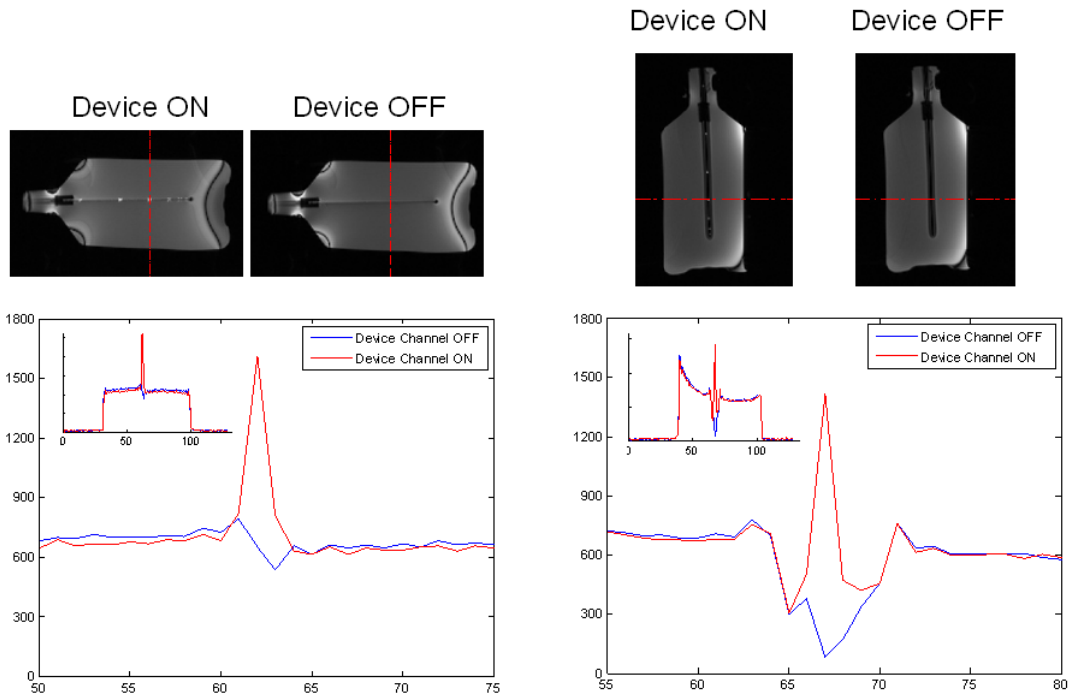

Figure 3.2.7. Signal intensity profiles (a.u.) for needle oriented parallel (left) and perpendicular (right) to B0 with and without device channel active.

Table 3.2.1. Relative signal and contrast values for active needle and corresponding passive needle artifact.

	Needle Parallel	Needle Perpendicular
Average Background Signal	649.6	677.6
Minimum OFF	535	83
Relative Negative Contrast	1.2	8.2
Maximum ON	1614.0	1414.0
Relative Positive Contrast	2.5	2.1

In quantitative measures of coil positioning and targeting accuracy, the active needle coil started 3.5 mm from the end of the needle bevel which resulted in a difference of 4.2 mm from the centroid of the most distal marker signal to the bevel end. The coils closely represented the true device centerline with centroids that deviated from

the actual needle central lumen by less than 0.5 mm (average for distal 3 points: 0.2 mm, range: 0-0.38 mm). The distance between the marker points measured by MRI were within 5% of the actual marker separation (average: 2.35%, range: 0.6-5%). In considering the entire marker width, the signal width for half-maximum intensity with the needle parallel to B0 was 2.8mm compared to the actual device width of under 1.7mm (Figure 3.2.8).

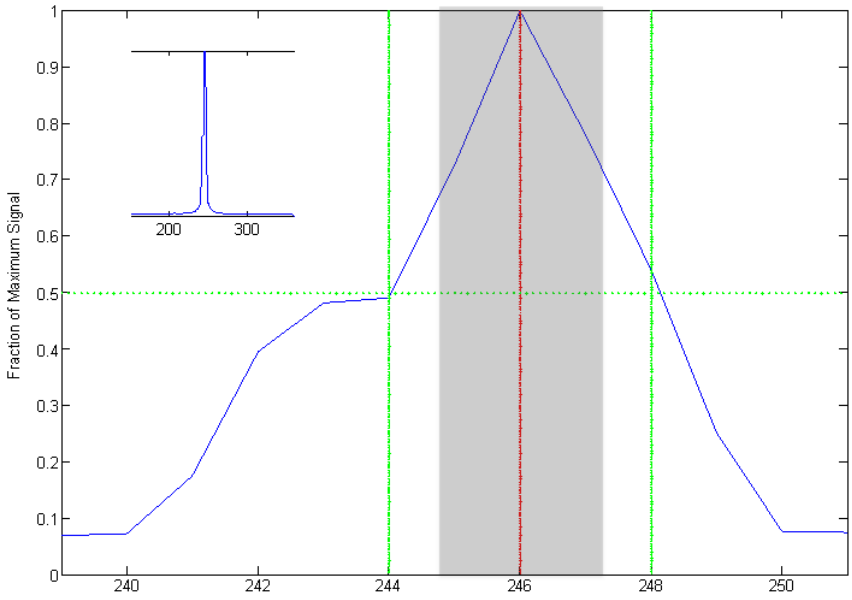

Figure 3.2.8. Active needle Signal Profile with half-maximum (green lines) and needle appearance (gray) shown.

3.2.3 Discussion

We have developed an active needle with distinct markers of needle position, trajectory and insertion depth. The device construction also maintained a smooth profile for entry into the skin and central lumen available for blood return, pressure, aspiration,

and guidewire use. The active needle allows rapid and clear device localization for percutaneous interventional MRI procedures with its distinct signal and image signature. The use of special MRI techniques like device-only projection for easy identification of device position and automated device finding and scan-plane prescription modes are also possible (6,111).

Commercially available non-magnetic metal needles in materials such as Titanium (*e.g.* In Vivo, others), *Inconel* 625 (*e.g.* EZ-EM), and other special alloys (*e.g.* Somatex) can appear in MRI larger than the actual device size and vary widely with exact needle composition, magnet field strength, orientation of the needle relative to B0, and imaging sequence (108,112,113). As a result, the appearance of these passive needles may not accurately represent the actual needle location, making it unreliable or unsafe for targeting of small lesions. Moreover, the needle susceptibility artifacts can be relatively large compared with vessel size, particularly when trajectories perpendicular to B0 are attempted (114). Even with the larger needle artifacts the active signal helped more closely locate the actual device position and tip location. We employed a nitinol needle body to try to further reduce the passive artifact appearance. Alternate non-metallic materials may be superior for visualization but at the expense of shaft-strength and sharp cutting edges in thin-walled needles.

Larger carbon fiber needle cannulas (14G and 18G) previously had been commercially available having significantly smaller artifacts than titanium equivalents (115) but also used an inner metal stylet for entry. A smaller carbon-fiber-reinforced plastic puncture needle was developed by Fraunhofer Institute for Production Technology (IPT) and is now available in Europe through RadiMed (Germany). The MR visibility of these carbon alternatives, however, may actually be insufficient for our application without any modifications or additional metal stylet to make them more

apparent during imaging (116). Other passive needle designs with specialized coatings also have been investigated to provide more precise tip location (117).

Active visualization as displayed in this work could be incorporated into these non-metallic designs for greater visualization with little needle base artifact and further improve the safety profile by eliminating the metallic base if an appropriately size composite needle becomes available. We demonstrated this by constructing a sample device using the small RadiMed needle base. The needle is very difficult to see even in phantom imaging without any modification but the imaging markers were clearly visible with the active modification (Figure 3.2.9).

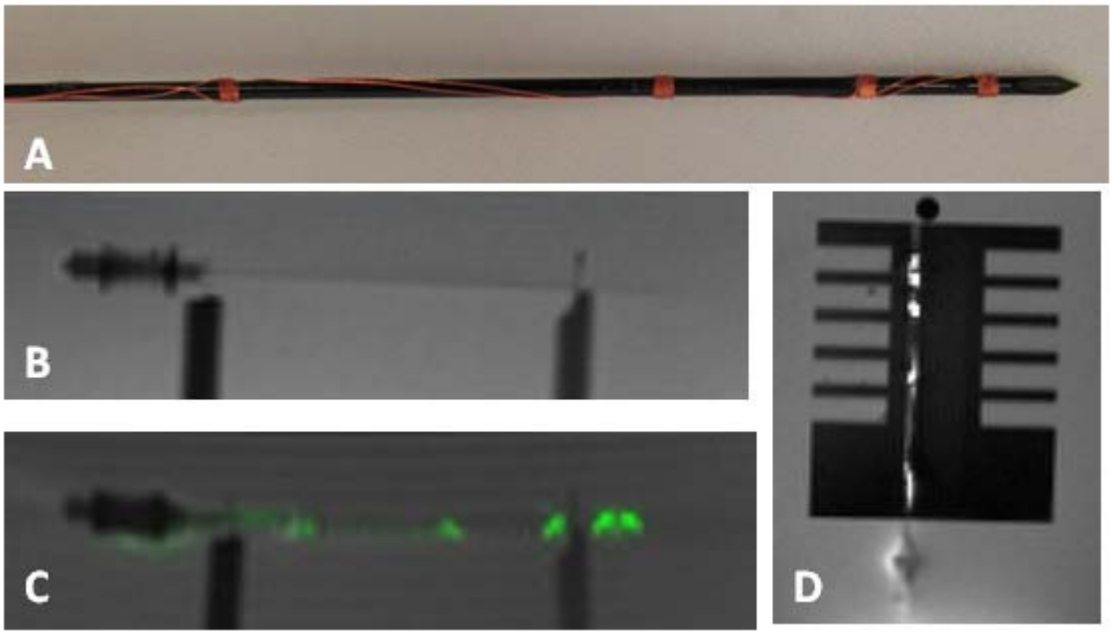

Figure 3.2.9. Active needle w/carbon fiber base construction (A). MR imaging of needle alone (B) and with active signal visible in (C) and (D).

While the needle handle was a little bulky in this demonstration to accommodate the currently used circuitry, the circuit components could be included in a much smaller needle hub. Incorporating the circuitry in the base of the device and using the non-metallic needle base could further improve the safe design of the device.

Other investigators have applied a needle stylet designed with a tip tracking coil in a novel PEEK and ceramic tip construction which was used for targeting liver cysts and MR-guided cholecystostomy (118,119). Tip tracking, however, requires independent acquisitions with tracking sequences where only the tip location and path is marked on prior or interspersed images. In cases where the needle may curve or take trajectories through critical structures, identifying the entire location on simultaneously acquired imaging may be necessary to improve procedure safety. Our approach to active imaging or profiling of a device provides the unique device signature on simultaneous real-time images. Stylets are less useful in cardiovascular applications where back-bleeding, pressure-monitoring, and ready guidewire access through an open lumen are considered important. The outer coating of the exterior coil was robust to skin entry and additional coatings could be used to reduce the friction and facilitate needle entry through the skin.

We assessed the active device profile as well as accuracy of the signal location to guide the requisite intervention. The marker signal closely reflected the actual device location with some discrepancy between the tip location and actual bevel, restricted by physical limits on distal placement of hand-wound coils. The signal width was also slightly greater than the actual device size. Decreasing the wire size could reduce this but at the expense of overall signal loss, and of greater manufacturing challenges of the more fragile small diameter wire. A grooved needle base may also be possible to embed the coils, reducing both physical and signal profiles. This also could be

addressed with image post-processing and device channel display properties. For example, sharper device delineation is provided in the real-time reconstruction and display system by squaring of the device channel signal (6).

In summary, we have presented a robust active needle design that provides clear tip and shaft visualization, and versatility for *in vivo* applications. Extensive demonstration and discussion of the *in vivo* utility of the active needle is presented in Chapter 5 on MRI-Guided Cardiovascular Access. Standardization of this approach to device signal evaluation will be helpful in characterization and assessment of MRI performance of a range of actively visualized devices including guidewires and catheters.

3.3 Active Cable

Non-surgical catheter-based device approaches are increasingly applied to treat a range of structural heart diseases. Such procedures could benefit from the anatomic context and dynamic information provided by MRI but the commercial devices typically used are often incompatible in the MR environment and small implants or target structures can be difficult to visualize. For atrial and ventricular septal occluder device delivery, the main component of these devices consists of a nitinol mesh where the disks appear as small signal voids on MR imaging without significant artifacts. Release of these nitinol occluder devices, which are attached by a screw to their delivery cable, requires a defined torque maneuver of the delivery cable. The delivery system which utilizes stainless steel mating screws produces sizable artifacts which completely obscure the device in imaging (Figure 3.3.1).

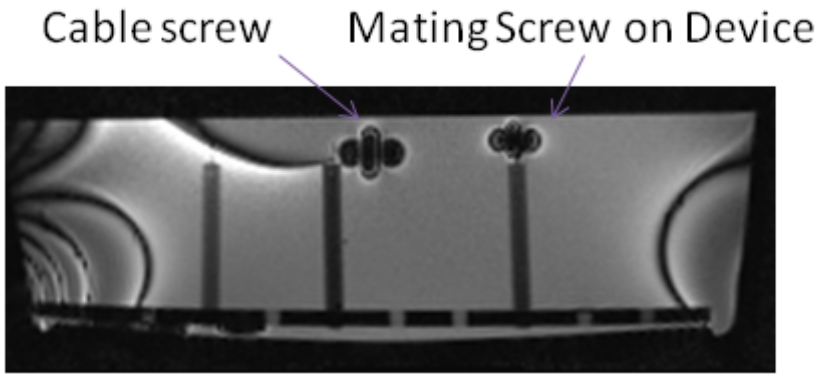

Figure 3.3.1. Commercial VSD occluder and delivery cable with stainless steel mating screws.

To improve MRI visibility during device deployment, the visibility of the disks is necessary while minimizing the image artifacts. This would enable the operator to better

visualize device deployment and positioning, taking advantage of MRI soft-tissue depiction to enhance procedural conduct and success. In addition, the delivery system must maintain its ability to reliably advance the disks and release the device upon deployment. We hypothesized that visualization of the occluder device deployment under MRI could be improved through the use of an active delivery cable where the implant, when attached, also becomes part of the active device. We tested this hypothesis in phantom testing and in a novel series of minimally invasive applications being developed in the laboratory, in which we treat structural heart disease directly through the walls of the chest and the heart in a beating heart without surgical incisions or exposure.

3.3.1 Methods

Active Cable Design and Construction

To improve the visibility of passive implant deployment, an active delivery cable was created comprising a loopless antenna. For device advancement and torquability, a nitinol inner conductor was used. The nitinol construction produces minimal MR artifacts and provides a superelastic core that is less prone to kinking while still providing sufficient pushability and torquability of the device. It was connected via laser welding to the mating screw for attachment of atrial and ventricular septal defect closure devices and vascular plugs and then insulated (Figure 3.3.2). A nitinol hypotube served as the outer conductor.

Figure 3.3.2. Inner rod of loopless construction with attached microscrew and occluder device.

A titanium mating screw was used on the cable to avoid the significant artifacts caused by stainless steel elements of the commercial delivery construction. Figure 3.3.3 shows cables with titanium and stainless steels screws and the sizable reduction in artifact.

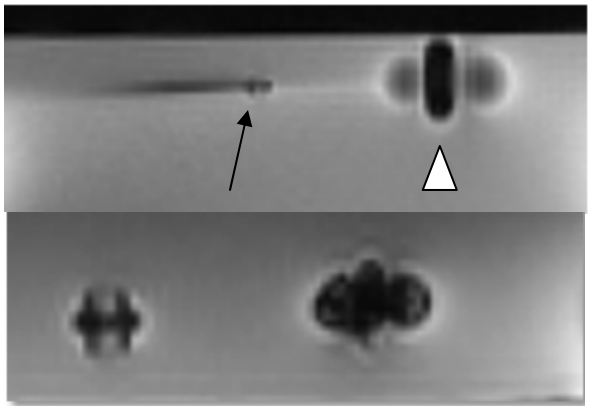

Figure 3.3.3. MR imaging artifacts of titanium replacement (left - arrow) and original stainless (right – arrowhead) microscrew on delivery cable (top) and VSD occluder device (bottom).

The cable performance was evaluated using off-the-shelf VSD occluder devices which retained the stainless steel microscrew and devices that were specially constructed with titanium replacements to further reduce artifacts (Figure 3.3.3). With the artifact removed, the borders of the unconstrained nitinol devices are recognized from their passive characteristics in a phantom.

Several additional design modifications were employed to ensure the mechanical handling and utility of the device. The nitinol core and hypotube were adjusted in both diameter to affect stiffness and torquability and length depending on the device delivery and target anatomy. For example, in transthoracic procedures, a shorter cable was developed and tuned accordingly with a handle designed to secure the circuitry and allow torquability with a rotating adaptor at the proximal connection (Figure 3.3.4). This enabled the device to be used by a single operator in closure of cardiac defects and helped address the additional connection requirements necessitated by active device use and protect the device connection during normal use and rotation.

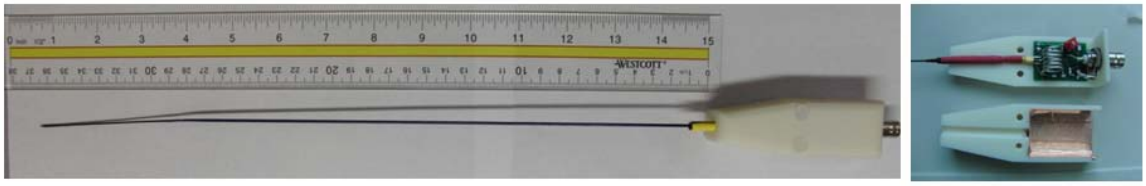

Figure 3.3.4. Example of shortened cable and incorporated circuitry designed to facilitate operator use.

Electrical characteristics and imaging evaluation

Reflection (S11) measurements were made with the cable alone and with the device attached. The cable was tuned and matched with the device attached to maximize signal. The signal profile was evaluated in the different deployment states: no device, device fully sheathed, 1-disk released, and 2-disks released.

In vivo demonstration

In addition to signal evaluation in saline phantoms, the active cable performance was evaluated during *in vivo* use for MRI-guided transthoracic VSD closure and left ventricular access closure and ASD occluder delivery in swine. Animal experiment protocols were approved by the institutional animal care and use committee, according to contemporary NIH guidelines.

3.3.2 Results

Electrical characteristics and *In vitro* imaging

Attaching the device to the cable changed the electrical characteristics and the antenna could be tuned and matched (closest to 50 ohms resistance - real component of impedance - with no reactance – imaginary component of impedance - at 64 MHz) specifically for the case of an attached device (Table 3.3.1).

Table 3.3.1. Differences in signal intensity and impedance of cable with and without device attached

	w/o Device		w/8mm Device	
Signal Profiles	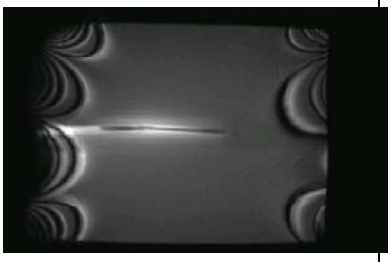		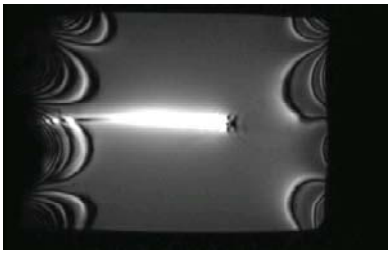	
Impedance Measurements (Ohms)	**Resistance**	**Reactance**	**Resistance**	**Reactance**
Air	5	15	5	16
Tip submerged in saline	13	17.5	15	12
Junction submerged	12.5	25	20	30
With Tuning Circuit	28	38	49	2

In extending the whip of the loopless antenna by attaching the device and tuning the cable accordingly, signal was also present all the way up to the device which increased the contrast of the passive implant artifact during deployment. This is seen in Figure 3.3.5 which shows the various deployment states and one-disk deployment can be clearly seen with the occluder devices that still possessed the stainless steel screw and those with the titanium replacements.

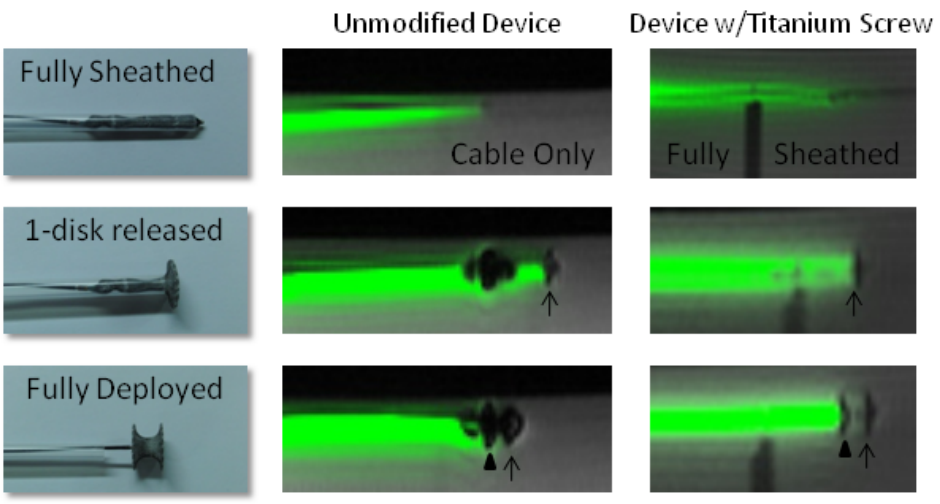

Figure 3.3.5. Device deployment states and corresponding phantom images with active delivery cable and unmodified commercial device and device with titanium screw. Arrow indicates distal disk with arrowhead pointing at the proximal disk.

In vivo demonstration

The active cable provided the operator necessary visualization for confident VSD and ASD device deployment under MRI guidance. The cables were able to reach their intended target, advance the disks appropriately from the delivery sheath, and release the device with reasonable rotation applied. Figure 3.3.6 shows the short cable in use for transthoracic VSD closure (120) where the pediatric cardiologist could clearly visualize LV disk signal void in both views with passive disk appearance contrasted against the active cable signal that goes up to the disk edge.

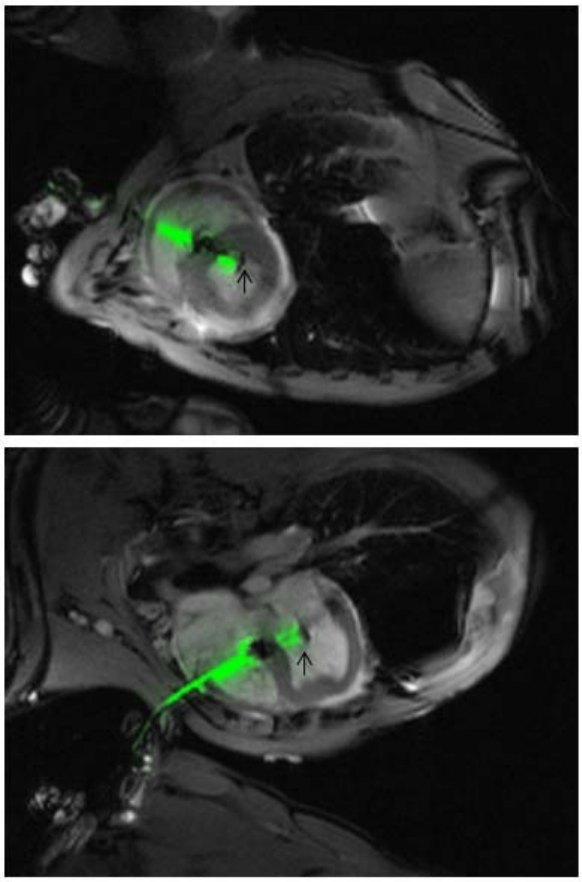

Figure 3.3.6. Left ventricle disk (arrow) release evident during transthoracic VSD device deployment.

Figure 3.3.7 shows an example of where the operator felt resistance when pulling the LV disk back towards the septum but the imaging with active cable signal showed that the device was caught in subvalvular structures and not opposed to the septum so it was resheathed and properly redeployed. This was not as readily apparent with the device channel inactive.

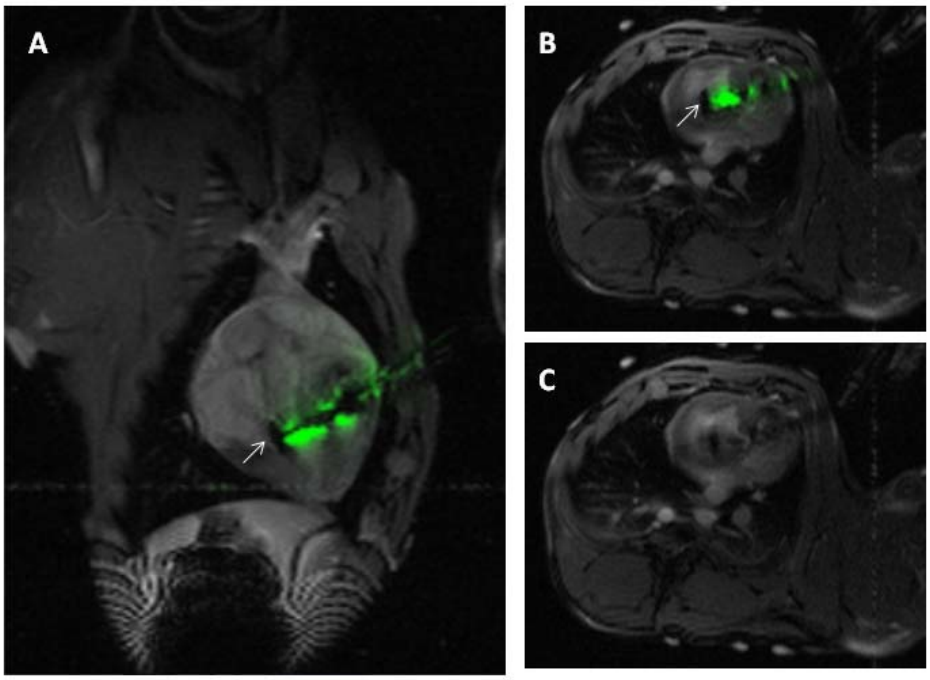

Figure 3.3.7. Proximal disk (arrow) caught on subvalvular structures seen in angled coronal view in (A) and clearly not opposed to interventricular septum in short axis (B). This is less readily apparent without the active device signal (C).

During experiments to evaluate the feasibility of VSD occluder device deployment to close percutaneous left ventricular apical large sheath access (121), the cable signal helped the cardiologist confirm that the proximal disk was opposed to the endocardial surface and the epicardial disk was positioned within the pericardial space before the device was released (Figure 3.3.8). This positioning is critical to ensure that the device is securely in place and pericardial entrapment doesn't cause tension on the ventricular wall or residual bleeding.

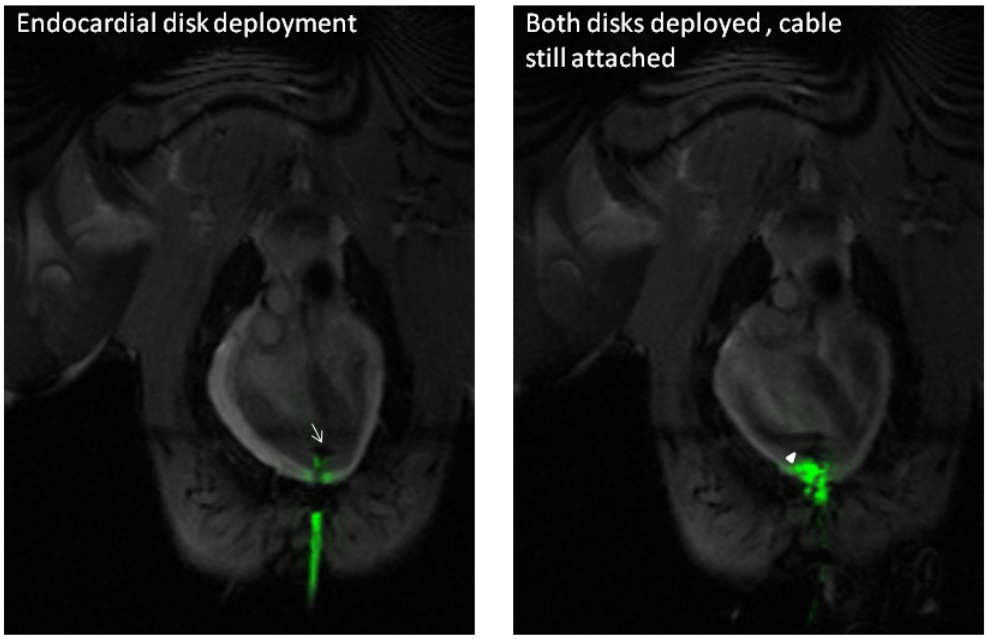

Figure 3.3.8. Endocardial (arrow) and epicardial (arrowhead) disk deployment clearly seen in LV apical access closure with active cable and modified device.

A longer, more flexible active delivery cable also enabled ASD closure with a commercial device from a transfemoral approach which is shown in Figure 3.3.9. The commercial ASD occluder positioning and disk deployment was enhanced with the active cable signal. Similar longer, more flexible cable designs could also enable transfemoral VSD occlusion and vascular plug delivery.

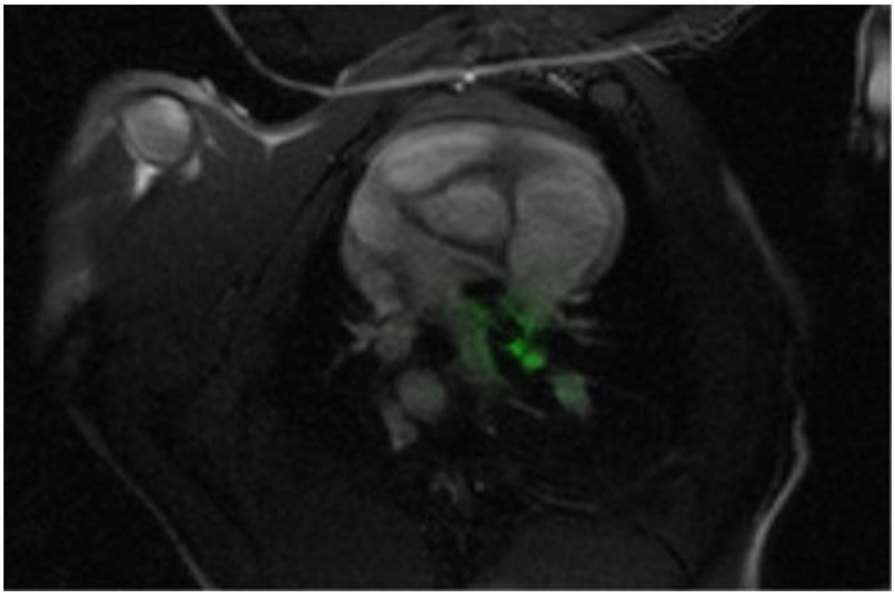

Figure 3.3.9. Device in place in atrial septum prior to release from the cable.

3.3.3 Discussion

Operators had much greater confidence in device position, state, delivery, and deployment compared to previous *in vivo* trials without the active cable. Proper deployment and positioning of the first disk is critical and the increased visibility of this disk allowed the operator to ensure it was properly opposed to the intended structure and take full advantage of the soft-tissue imaging afforded by MRI.

Incorporating the device as part of the loopless antenna and appropriate tuning helped provide signal all the way to the distal disk whereas loopless antennas normally have signal drop-off towards the tip which was seen when the device was not connected. With the motion and varying signal in the heart, this was essential for clear determination of distal disk release and placement.

Compared to the commercial delivery cable, our cable typically had similar stiffness at the distal end where the nitinol rod extended as the whip and increased stiffness proximally where the additional nitinol hypotube served as the outer conductor for the loopless antenna construction. This did not seem to impact performance and in some instances made the devices easier to deploy by providing increased proximal pushability. Release of the device with the modified delivery system with handle and rotatable connector was not as constrained by attachment to the scanner necessary for active

While the titanium parts replacement largely eliminated the artifacts associated with the device delivery system, they do present some additional challenges compared to stainless steel. Titanium is much harder to machine than stainless steel, particularly with small components such as these screws, and companies with these capabilities are limited. The less common use of the material compared to stainless steel and more complex processing make this option more expensive. Furthermore, in these threaded parts, there is concern over increased risk of defective parts or stripping the screw threads since the hardness and stiffness may be less and the weight-to-strength benefit of titanium cannot be appreciated in such small parts. However, this risk still exists with stainless steel microscrews given the small size of the thread features and caution must be taken during device use to mitigate this risk. For general application of these devices, the benefits of less impacted future MRI imaging studies following implantation and the material and manufacturing limitations would have to be considered,

We also pursued imaging techniques to reduce the impact of the device artifact to enable use of commercial implants if device modification is undesirable. We tried to improve the implant appearance in those that retained the original screw by testing sequences which are less susceptible to artifacts by using short echo times and

refocusing pulses (spin echo) as seen in Figure 3.3.10. Distal disk release appearance is highly dependent on the size of device and corresponding length of elongation in the sheath which provides a natural separation between the screw causing the artifact and the released disk. The fully deployed device appearance was improved with the turbo spin echo (TSE) imaging, but artifact impact was similar or worse using gradient recalled echo (GRE) real-time compared with SSFP techniques. Other ultra-short TE imaging or specialized approaches to reduce metal artifacts (122) could also be used but may not be suitable for real-time guidance for device deployment.

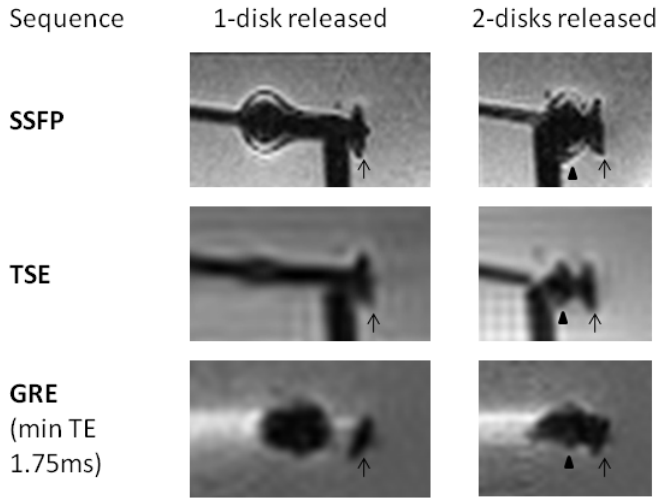

Figure 3.3.10. Imaging deployment of unmodified (stainless-steel-containing) commercial devices with different sequence parameters. Distal disk marked by arrow and proximal disk with arrowhead.

In summary, the custom active delivery cable, with or without substitution of steel elements of the nitinol occluder device, allowed and enhanced performance of MRI-guided device positioning in phantom and *in vivo*. This enabled a completely new family

of pre-clinical interventional cardiovascular procedures, namely direct transthoracic cardiac access and repair of heart defects.

3.4 Active Configurable Laser Delivery System

A transjugular intrahepatic portosystemic shunt (TIPS) procedure creates a direct connection between the hepatic and portal veins to reduce portal hypertension and associated conditions like life-threatening variceal hemorrhage. Early use of TIPS was shown to reduce morbidity and mortality compared with rescue procedures in patients with cirrhosis and variceal bleeding (123). TIPS creation is performed clinically under X-ray guidance. Connecting the hepatic and portal veins can take more than 50 needle passes, because the target portal vein is difficult to visualize under angiography. MRI guidance for TIPS can provide clear visualization of hepatic and portal vein structures without exogenous contrast which may help reduce procedure length, x-ray exposure and risk of significant complications especially extracapsular, subcapsular, and biliary bleeding (Figure 3.4.1).

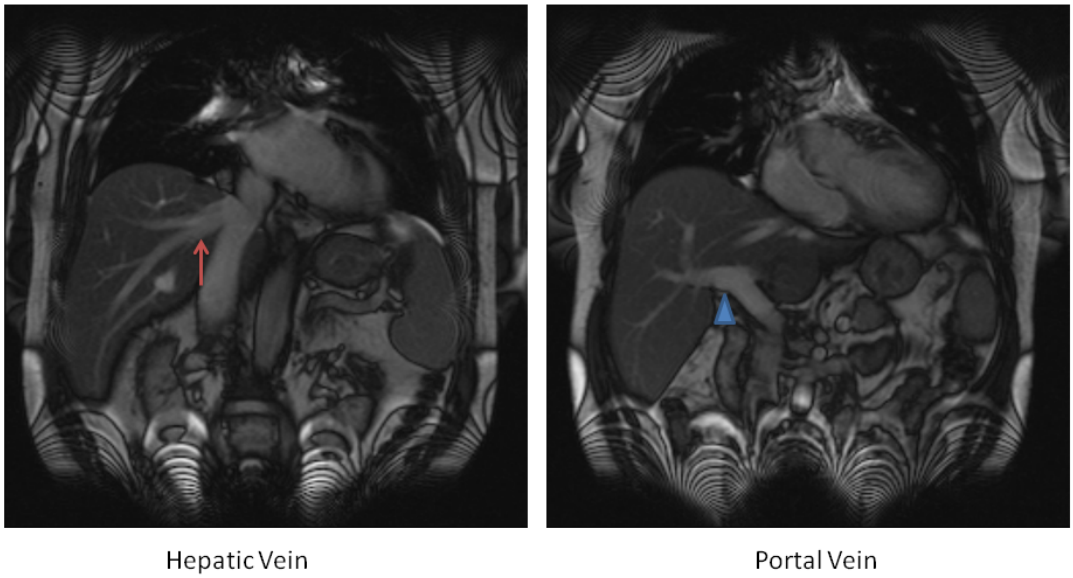

Figure 3.4.1. MRI imaging of hepatic and portal veins. Vessels are apparent without need for exogenous contrast administration.

This procedure has been demonstrated in patients using hybrid MR/X-ray systems but device visualization under MRI was limited, and much of the procedure was performed using the in-magnet X-ray system (26). Clinically, TIPS is typically performed with needle catheters or stylets. Needle attempts may be difficult in patients because of rigid fibrotic livers of cirrhosis. Applying a vessel crossing system with an energy source could provide a more controlled and effective passage while minimizing regional damage and hazard.

An energy source such an excimer laser could be used to accomplish these traversals, but this method requires additional positioning and support for advancement in order to achieve the desired trajectory. Preliminary experiments in excised liver tissue indicated that the mechanical properties of the active laser alone were not sufficient to perform the TIPS procedure without an additional delivery system. The active laser lacks the stiffness to maintain a straight trajectory through the liver parenchyma when advanced by the operator.

The anatomical relationship between the hepatic vein and the portal vein requires the ability to direct and steer the active laser into the proper position in the vasculature and then through the liver parenchyma. The system must first access the hepatic vein branch from the IVC with a rightward deviation and then reorientated almost completely anteriorly to pass to the desired portal vein branch. In initial testing, long active needle designs with polymer shafts were difficult to position and did not have the necessary shaft stiffness for advancement. Preliminary testing of the laser alone for liver passage showed that it could not be positioned and advanced without sufficient back support to keep it from buckling or veering off-target. Therefore, a delivery system was

developed to provide back-up support to the laser as well as the necessary curvature and visualization to direct the laser into the hepatic vein and towards the portal vein. We then tested the feasibility of this method to perform the TIPS procedure under real-time MRI guidance using actively visualized excimer laser and delivery system.

3.4.1 Methods

The active delivery system design incorporated two insulated concentric nitinol hypotubes, each with a unique curvature which also formed the inner and outer conductors of a loopless antenna to provide both signal to indicate the laser positioning curvature and highly configurable positioning. The curvature in the nitinol tubing was instilled under mechanical stress during annealing. Curvatures were selected to achieve the necessary curve reach and advancement for the target anatomy while also permitting ready resheathing of the inner tube. Hypotube size was selected to allow shape processing and adequate mechanical handling. When increased curvature and more torquability was required, the wall thickness of the inner tube was increased to prevent kinking with the greater curvature and also provided more shaft support and torque responsiveness during rotation. This was balanced with not selecting too great of a wall thickness where the inner tube could not be easily resheathed by the outer tube due to loss of flexibility. The inner hypotube could be advanced and withdrawn as well as rotated within the outer hypotube as necessary to modify the curvature of the inner hypotube and entire system (Figure 3.4.2).

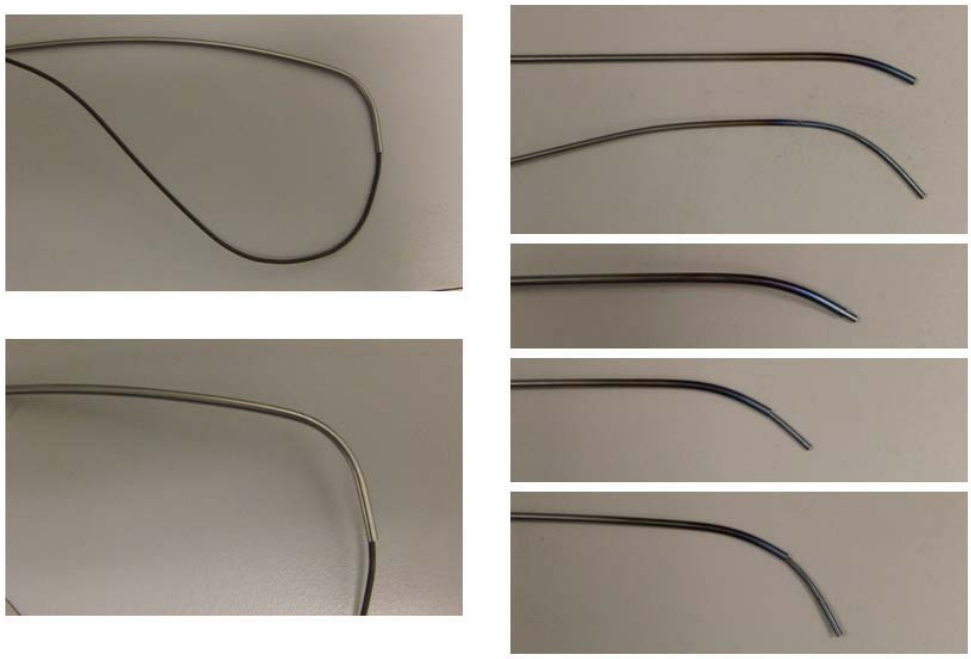

Figure 3.4.2. Nitinol hypotube constrained in the desired positioning before annealing (left column) and then the shape retention seen after (right). The hypotubes could then be placed inside one another and variably deployed.

After annealing, the inner (0.062” ID, 0.072” OD) and outer (0.104” ID, 0.112”OD) nitinol hypotubes were insulated with PTFE liners and thermoplastic (PEBAX) exterior insulation to form the components of the loopless antenna and enable smooth movement of the two tubes relative to each other. Connection at the proximal end used a flexible, adjustable connector to tolerate the variable positioning of the two parts. Each tube also had its own adapter to allow independent flushing of the two parts of the system. The inner lumen of the delivery system was 0.057” and the outer diameter of the entire system was 0.120” (<10 Fr). An MRI-compatible excimer laser catheter was modified to include a single loop channel at the distal tip enabling active visualization under real-time MRI (Spectranetics, Colorado Springs, CO). The outer diameter of the

excimer laser was 0.045” (4 French compatible). The entire system with the variable deployment states and laser exiting from the tip is shown in Figure 3.4.3.

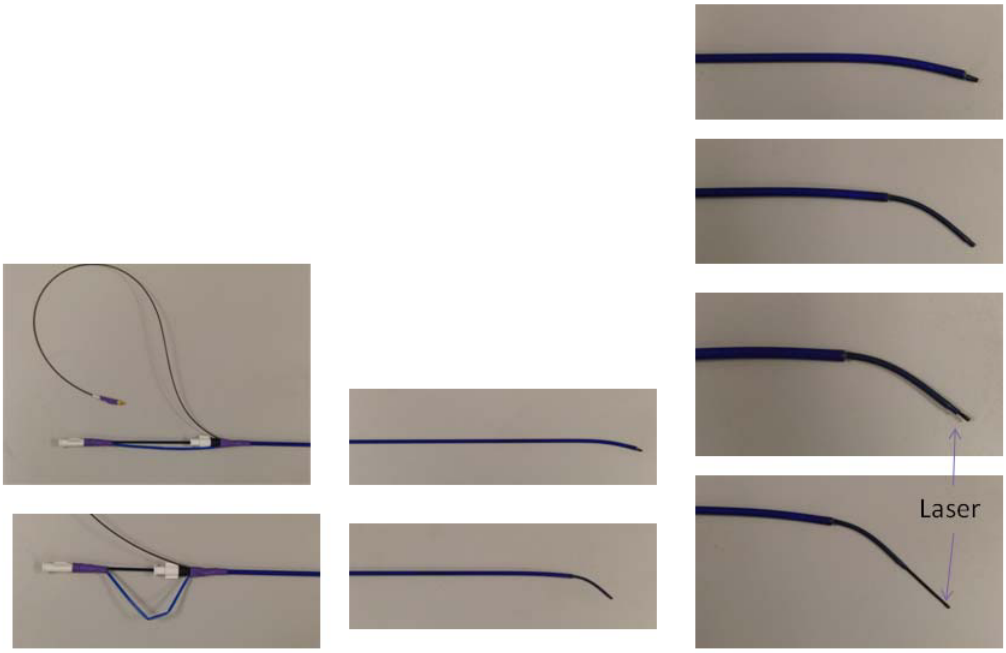

Figure 3.4.3. Complete system with flexible connector and variable states with laser deployed.

The excimer laser and delivery system were each connected to scanner receive channels via tuning, matching and decoupling circuitry and a multi-channel preamplifier box. Device signal with the laser was first evaluated in saline phantoms and in an *ex vivo* liver. Mechanical device performance was tested for vessel traversal in *ex vivo* liver tissue. An *in vivo* feasibility study of laser-mediated hepatic to portal puncture in swine under real-time MRI guidance demonstrated both device visualization and functional performance.

3.4.2 Results

The configurable system enabled the operator to vary the amount of curvature as well as easily alter shape by rotating the inner tube relative to the outer one to produce C and S-shaped configurations (Figure 3.4.4). The system could be delivered to the liver with the inner tube retracted and then deployed and rotated to reach the target site.

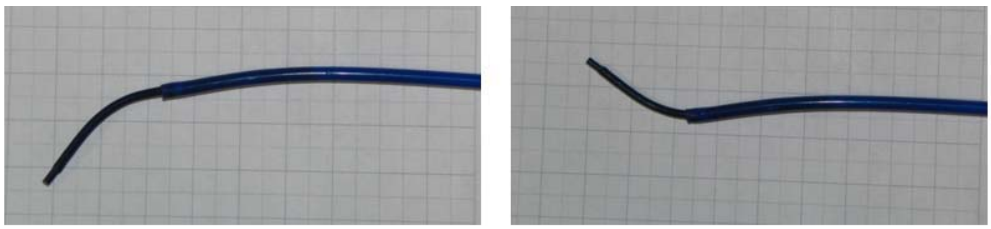

Figure 3.4.4. Rotation of the inner hypotube allows C and S-shaped curvatures.

In phantom imaging, the device curvature was clearly visible with an increase in signal when the inner sheath was extended and the loop coil on the laser providing the necessary tip signal for full device visualization (Figure 3.4.5).

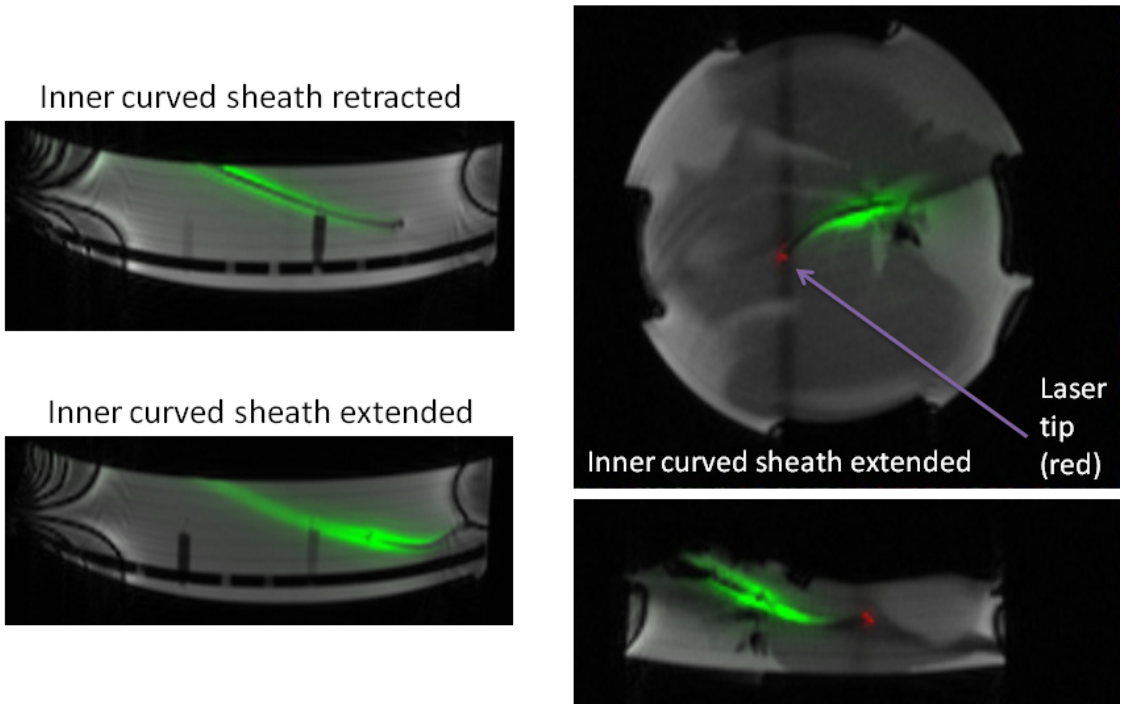

Figure 3.4.5. Phantom and ex vivo liver imaging of the active delivery system and laser.

During the *in vivo* feasibility study in swine, the delivery system was able to direct and provide back-up support to the laser which successfully burned through the hepatic vein wall, the liver parenchyma and into the portal vein (Figure 3.4.6). The system was delivered with the inner tube sheathed until the liver was reached and the necessary curvature released by advancing the inner tube. To alter the direction of the curvature, the inner tube was easily rotated and positioned appropriately. First, the system was angled to the right and positioned into the right hepatic vein branch and then the inner tube rotated anteriorly to aim towards the target portal vein branch. The configurable system and advanced imaging guidance enabled a novice operator to successfully perform this extremely complex interventional procedure. The system was tested with both advancing the laser alone and advancing the entire system during laser application.

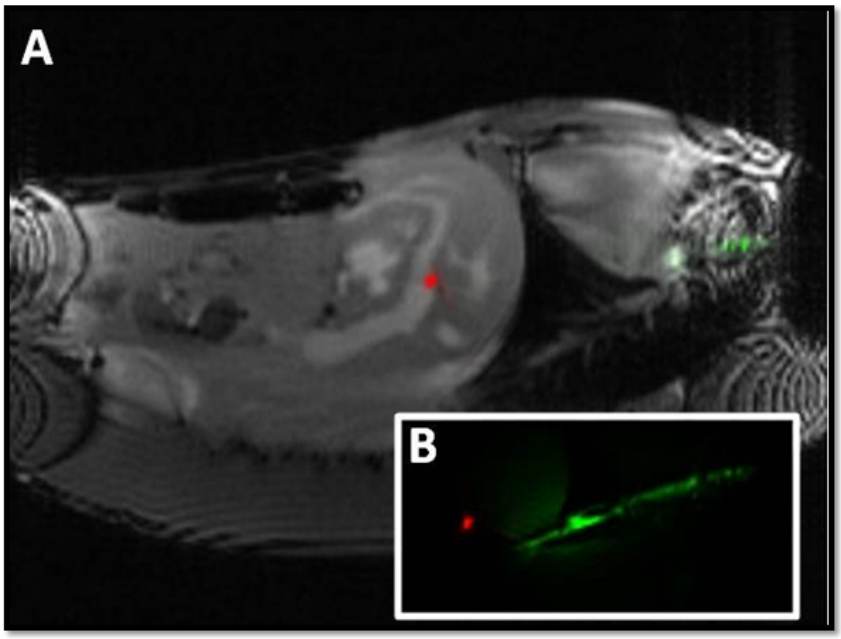

Figure 3.4.6. Accessing the portal vein in vivo. Laser enter portal vein (A) with projection mode image of delivery system to indicate the orientation (B).

3.4.3 Discussion

The excimer laser and delivery system facilitated targeted passage from the hepatic to portal veins with minimal resistance in naïve swine liver. Additional testing in fibrotic livers is necessary. The ability to rotate the inner hypotube relative to the outer hypotube proved invaluable during the *in vivo* demonstration because it enabled quick alteration of the device position to achieve the desired angulation and trajectory.

While the delivery system loopless design had limited signal at the distal tip as is typical of loopless antennas, the loop coil at the distal end of laser provided complimentary signal for complete device visualization. Signal along the device shaft

was appreciable when the inner tube was retracted but increased as expected with advancement of the inner component that effectively created the whip of the loopless antenna. For procedures that may traverse low signal areas between vascular targets such as in the mediastinum, internal signal sources might be necessary for proper laser tip position and angulation.

In summary, we developed a configurable, loopless active MRI guiding catheter to work in tandem with an active loop-coil-tipped excimer laser catheter. We used these together to conduct a TIPS procedure in healthy swine. Of note, the MRI vessel guidance and enhanced conspicuity and satisfactory mechanical performance of these image-guided catheter devices allowed even a novice non-physician operator successfully to conduct a highly specialized vascular interventional procedure. This system provides a visible, controllable and adaptable approach to vessel and tissue passage that could be used for other novel MRI-guided examples of extra-anatomic bypass such as a Blalock-Taussig aorto-pulmonary shunt.

3.5 Chapter Summary and Contributions

In this chapter, we have presented distinct devices to enable three different types of MRI-guided cardiovascular interventional procedures. Each device design incorporated considerations for device utility and MRI visibility. Each were evaluated in phantom testing and then during *in vivo* procedure feasibility animal studies. The active needle provided distinct tip and shaft visualization within a robust construction that permitted the studies described in Chapter 5. The active delivery cable incorporated the device into the active antenna design and permitted cardiac implant delivery with greater operator confidence in device deployment and positioning. The active laser delivery system provided the necessary support and positioning for the active laser catheter to permit initial feasibility trials of TIPS, an example of extra-anatomic bypass facilitated by MRI guidance. A thorough evaluation of the device signal performance also was developed and performed which could be applied to future devices.

CHAPTER

4

INTERVENTIONAL MRI SAFETY

4.1 Introduction

A comprehensive approach to evaluating device heating is necessary to determine the parameters under which these devices with conductive components can be used safely in the MR environment and without risk to the patient or operator. The numerous variables that can influence heating in the MR environment and the complexity of the devices make it difficult to employ electromagnetic (EM) simulations and necessitate extensive experimental testing for validation. Most of the observations on device heating in MR examined bare or simple insulated wires and/or limited insertion lengths in disparate phantoms filled with different media and show differing results (124).

Current standards focus on conservative device positioning in extreme horizontal off-sets with devices aligned parallel in high local E-field regions that may never be encountered during constrained clinical procedures (125). In endovascular cardiac procedures, devices are limited to the vasculature in passing from peripheral vascular entry (access) points and thereafter to the central vessels and the heart. Trajectories from femoral access follow the centrally located, in both right-left and anterior-posterior aspects, aortic and caval vessels. Limited information is available on actual device heating in larger animal models which would more closely represent the clinical use scenario. Table 4.1.1 outlines the advantages of the different methods to investigate potential heating as well as their shortcomings.

Table 4.1.1. Different approaches to evaluating MRI device heating risk.

	Utility	***Shortcomings***
EM simulation	Identify key parameters for device design Inform phantom testing process for areas of maximum heating Human simulation possible in multiple configurations	Difficult to simulate complex device constructions with many simplifications and assumptions necessary SAR distribution does not necessarily = heating Device and human simulations must be validated Computation time and expense in model development
Phantom testing	Investigate important variables identified and relative influences on heating and signal Test device prototypes for heating profiles	Phantom geometry doesn't represent animal or human (shape, assymetry, E-field distribution) Typically test "worst-case" positioning not reflective of actual use Significant externalized wire portion can impact results
Animal testing	Temperature measurements during simulated normal use Observe influence of perfusion with *in vivo* and *in situ* measurements	Animal shape does not represent human anatomy and may impact corresponding E-field distribution and conditions of use Procedures are dynamic and positioning of devices can be highly variable
Initial clinical trials	Continual temperature monitoring and potential scanner feedback during use to ensure patient safety and determine appropriate operating conditions Need physiological data to evaluate human simulations	May not experience range of possible positioning in all cases

In this work, we started with testing in gel phantoms to characterize the heating potential of our active interventional devices and determine the critical testing parameters as well as improved evaluation methods. Animal studies provided an *in vivo* comparison of device heating potential during typical use and the additional reduction of heating from blood flow and thermal regulation. Finally, we implemented an approach for device monitoring and dynamic scanner feedback control to further assure active device safety.

4.2 Components of Active Device Safety

In this section, we explore the heating characteristics of our devices in phantom studies with initial *in vivo* correlates. Eddy currents induced in the phantom lead to high E-field and local SAR distributions which have been demonstrated in EM calculation and simulations (126). Horizontal off-set and depth positioning first were tested to correlate the level of device heating observed in these high E-field regions and contrasted with more realistic device positioning. Critical insertion lengths, or resonant lengths, may not occur at half-wavelengths near 25cm for dielectric of the phantom with each device construction. The devices contain varied electric conductors and coils and are differentially insulated along the wire length which can alter the effective dielectric and electrical length of the wire. The device and placement variability may also impact the points that may experience the most heating. We also investigated potential approaches to limit RF interactions such as RF shielding to see if it could limit the interactions with the exposed wire and a floating trap to try to suppress unwanted shield currents on the external wire and examine their effects on heating.

4.2.1 Methods

Phantom Design

Phantom testing was conducted using a 72 cm x 42 cm x 19 cm rectangular acrylic phantom (Acrylic Custom Works, Rockville, MD) filled to 9cm with a polyacrylic acid (PAA) gel formulation (30L distilled water, 1.32 g/L NaCl (Sigma-Aldrich, St. Louis, MO), 10 g/L PAA (Sigma-Aldrich 436364) in accordance with ASTM standard 2182-02 and subsequent 09 revisions (125) . This provides a gel with similar conductivity and

dielectric properties as tissue with the gel limiting convective heat transfer. Access points were drilled in the end wall at 0, 2.5, 7.6, and 12.7 cm offsets. A polypropylene pegboard with 2.5 cm grid spacing (Pegboard with 9/32" holes, McMaster-Carr, Robbinsville, NJ) was secured to the bottom of the phantom. Acrylic rods (5/16" extruded acrylic rod, McMaster-Carr, Robbinsville, NJ) were cut to varying heights (2, 4, 6, 8 cm) and machined to fit the peg board and with a groove at the top. Flat nylon washers (#12 screw size, McMaster-Carr, Robbinsville, NJ) were affixed into the grove of the top of the rod with Epoxy and used to keep the device on the support pegs. For a given trajectory, the pegs were placed at least every 10 cm but not at a point of temperature measurement. A consistent patient registration was used for the scanning with the phantom including an entered weight of 200 pounds and minimum age of 18 years for no restrictions on scanner power output.

Using this pegboard and rod system to secure the device location in the phantom, we investigated different device positioning by varying horizontal offsets (distance from horizontal isocenter), depths (from bottom of the phantom) and insertion lengths (length of guidewire in phantom from entry point to tip). The center of the phantom was placed in the isocenter of the magnet with shifts of the phantom along the *z*-axis of the magnet also tested to examine the effect of varying isocenter. The phantom also incorporated modifications including a hollow acrylic v-shape (Acrylic Custom Works, Rockville, MD) to simulate the groin region and femoral vessel phantom (Lake Forest Anatomicals, Lake Forest, IL). The phantom set-up is shown in Figure 4.2.1.

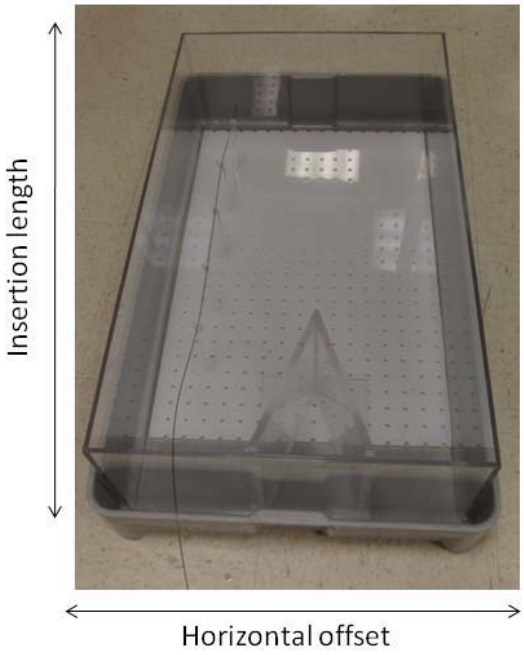

Figure 4.2.1. Heating phantom including a V-shape with wire secured with pegboard and rods.

Temperature Measurement

Temperature measurements were performed using fiber-optic temperature measurement systems with either white-light polarization interferometry sensors (FOT-M temperature sensor, FISO, Quebec, CN) or semi-conductor band gap technology with a Gallium arsenide crystal (OTG-M170, OpSens, Quebec, CN). Significantly smaller sensors currently are available with the semiconductor-based sensor as small as 62 micron for the sensor with an 80 micron signal transmission fiber. The larger temperature sensors were initially attached to the exterior of the guidewire at key transition points using small rubber O-rings (McMaster-Carr, Robbinsville, NJ) to keep the sensors close to the device without the use of an adhesive which could damage the device and/or sensor. Smaller sensors were attached with thin-walled heat shrink

(Advanced Polymer, Salem, NH) for testing in the anatomic configurations and initial testing *in vivo* in swine. Corresponding signal conditioners were connected to a personal computer running the appropriate acquisition software. Post-processing of the temperature data was performed to determine baseline temperatures, increase from baseline, and rates of increase. Results are normalized to the maximum heating observed in a trial to observe trends and reduce variability between absolute guidewire measurements which may have been dependent on the particular guidewire build and small variations in temperature sensor placement.

Device Testing Conditions

The devices tested for this analysis were mainly one or two channel 0.035" active guidewires with a tip coil and loopless antenna construction in the shaft (127). Prior to testing, the guidewires were marked with a silver permanent marker to indicate the varying insertion lengths to be tested and improve device placement reliability. The phantom was similarly marked to indicate tip position for a given insertion length. Active devices were connected to the scanner via their tune, match and decoupling circuitry, a coaxial cable, and then preamplifier box. Non-magnetic coaxial cables were tested in varying lengths. Additionally, a coaxial cable was constructed with a quarter-wave coaxial choke using a triaxial cable and shorting the two shields a quarter-wave from the open end to form a high impedance block there to shield currents on the cable.

Alterations to the externalized guidewire (portion not submerged in the phantom) were also tested for their impact on device heating on a 1m long guidewire. A PVC cylinder was covered with RF shielding material (Magmedix, Fitchburg, MA) and placed over the external portion of the guidewire. A floating trap which could be slid over the

guidewire was constructed from concentric copper tubes (McMaster-Carr, Robbinsville, NJ) with one end shorted with a conductive flat washer (McMaster-Carr, Robbinsville, NJ) and the other end tuned to 64 MHz with non-magnetic capacitors (ATC, Huntington Station, NY).

SAR Measurements and Applied Power Comparison

Given the reported variability of SAR measurements for various scanners (128), whole-body SAR calorimetry measurements were performed to confirm the SAR values reported by the scanner in accordance with NEMA standard test protocols (129). A similarly sized phantom as that used for the device testing was insulated with 2.5 cm thick polyurethane foam insulation (McMaster-Carr, Robbinsville, NJ). Only NaCl was added to achieve the desired conductivity without gel since this test examines the temperature rise of the entire volume. The sequence was run for 2 hours to generate sufficient heating for measurement. SAR was calculated using a specific heat capacity (Cp) of 4186 J/kg-C for the saline fill and Equation 4.2.1.

Equation 4.2.1. SAR Calorimetry Measurement

$$SAR = C_p \frac{\Delta T}{\Delta t}$$

Scanner reported SAR, B1rms and power applied during scanning of a phantom, large swine and normal human subjects were compared to identify appropriate testing conditions for phantom studies relative to values for animal and human imaging. Animal experiment protocols were approved by the institutional animal care and use committee,

according to contemporary NIH guidelines. Human scanning was performed in accordance with IRB approved protocol.

Realistic Positioning and Initial *In vivo* Testing

Since the edge of the phantom represents a high E-field environment that may not be experienced in vivo for the intended application of our devices, we tried to identify the level of heating expected in vivo and realistic positioning in the phantom. Initial *in vivo* measurements in swine were made with the temperature sensors attached to the guidewire (2 at the tip and 1 at the junction) with heat shrink as described earlier (Figure 4.2.2).

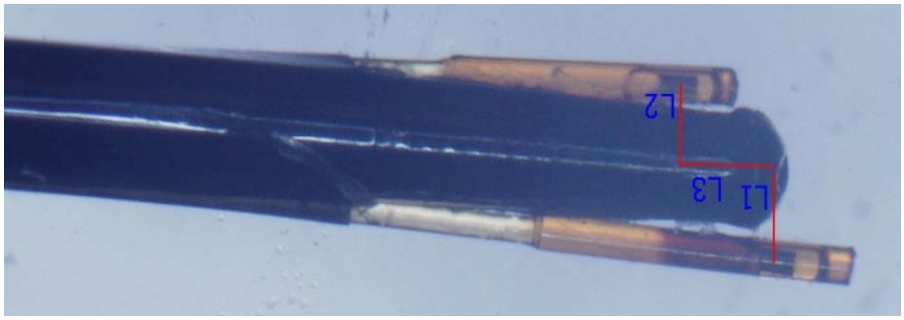

Figure 4.2.2. Fiber-optic temperature sensors attached to the tip of the 0.035" guidewire.

Similar positioning was also modeled in the phantom and compared with extreme horizontal off-set for the same guidewire. The wires were positioned, baseline temperature acquired, and scanned for the same period of time in the different scenarios.

4.2.2 Results

Horizontal Offset and Depth

Significant asymmetry was observed in device heating on either side of the phantom which correlates with the asymmetric phantom current distribution. On what would be the patient right side of the phantom in a head-first, supine positioning, higher heating was seen with device placement closer to the bottom of the phantom compared to shallower positioning. Similar offsets on the left-side of the phantom produced considerably higher heating than seen on the right with the peak seen instead at the shallower depths. Figure 4.2.3 shows different in heating for wire positioning on the right and left sides of the phantom with varying wire depth.

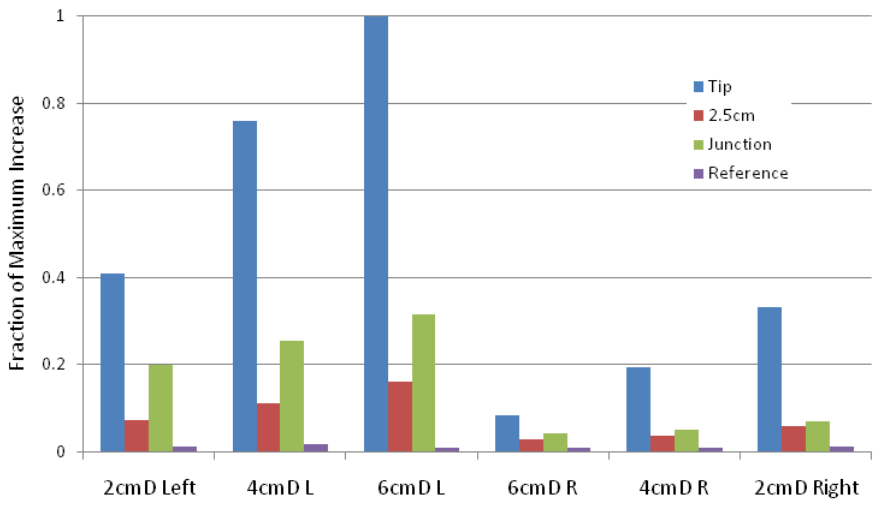

Figure 4.2.3. Influence of phantom side and depth on wire heating.

Insertion Length and Points of Device Heating

Peak heating at the tip for the guidewires tested was seen at insertion lengths between 30 and 40cm with the wire aligned along the z-axis of the bore. These insertion length trends were observed both at extreme horizontal offsets in the phantom as well as along the midline of the phantom with measurements made with increased power deposition to get achieve appreciable heating. The level of heating was highly dependent on the exact wire placement and multiple measurements were made trying to place the wire at the same insertion length and maximum value measured could vary up to about 20%. Other regions of the guidewire such as the hypotube junction did not necessarily have maximum heating at the same insertion lengths as the tip which is seen in Figure 4.2.4.

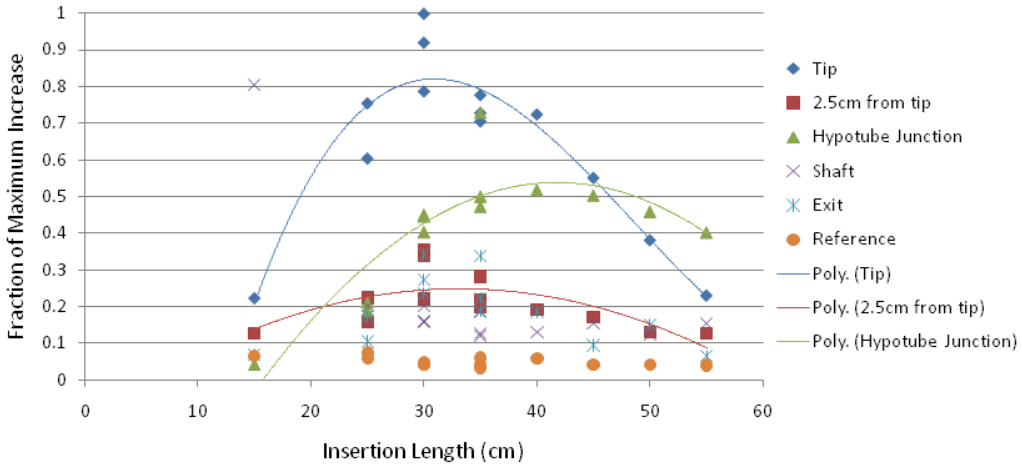

Figure 4.2.4. Varying insertion length for a given depth and horizontal off-set.

Isocenter

Moving the phantom along the z-axis of the scanner bore by adjusting the table position so the center of the phantom was changed relative to the isocenter of the magnet also influenced the level of heating observed. The isocenter position that produced the maximum heating was related to the given insertion length (Figure 4.2.5).

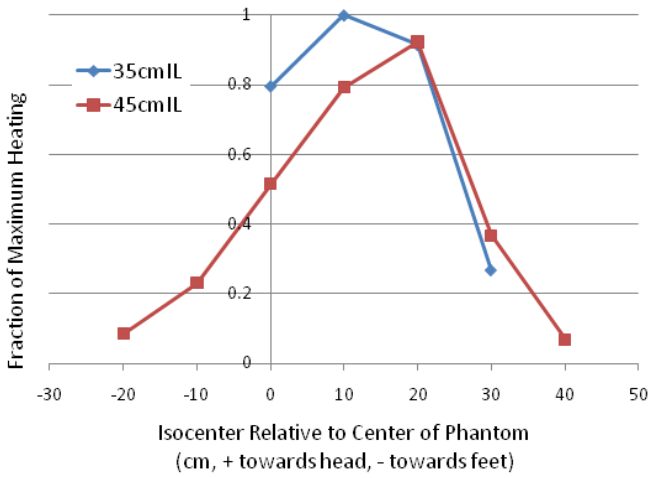

Figure 4.2.5. Impact of isocenter positioning for different insertion lengths.

Coaxial Extension Cable

Coaxial cable initially was used to connect the device circuit box to the preamplifier box. Varying the length and properties of this cable altered the level of tip heating observed. One length of wire was not beneficial for all guidewires and positioning nor did heating reduce as wires got progressively longer or shorter. There appeared to be particular lengths which may produce some reduction in heating but the response was unpredictable. The choked triaxial cable produced slightly lower heating than an equivalent length coaxial cable when used in the orientation with the trap distal.

Figure 4.2.6 shows the heating curves for a guidewire unmoved during acquisitions with only changes in the coaxial cable length.

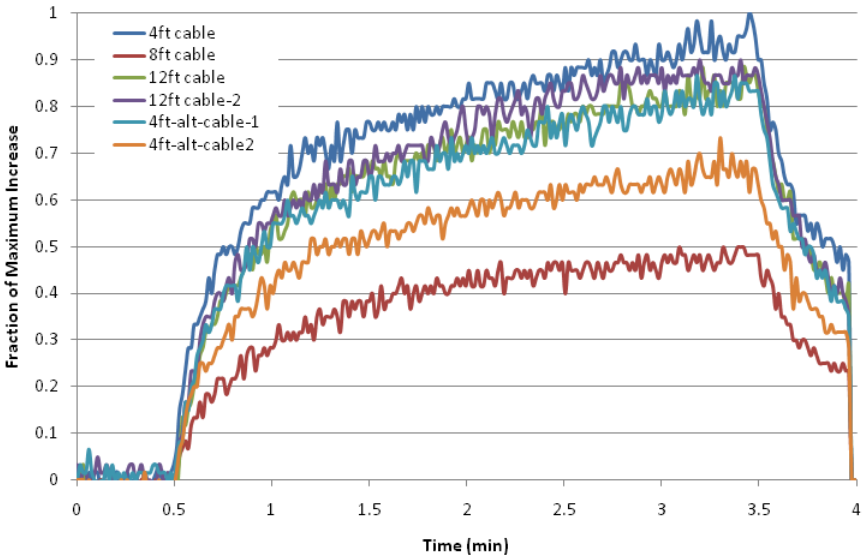

Figure 4.2.6. Relative tip heating for varying lengths of coxial extension cable.

Externalized Guidewire

The RF shield and floating trap did not have an appreciable effect on wire heating for the 1-m long wire. When the externalized wire was brought in contact with the edge of the bore, increases in heating were intermittently observed but difficult to reproduce with similar device positioning.

Applied Power

Scanner reported SAR values correlated with calorimetry measured values once the coil files for the preamplifier box were appropriately corrected. In power comparisons we performed, B1rms estimations reported by the scanner were similar for the same sequence and duration in the phantom and human but WB-SAR and power deposited values differed (Table 4.2.1). The average power deposited (Watts) was approximately two-thirds for the phantom than the values observed in animal and human subjects scanned for comparison. The B1rms values were highest for the sample swine experiments.

Table 4.2.1. Scanner Reported Power Indicators for Phantom and Human subject.

RT SSFP sequence 45º FA (3 slices)	Whole Body SAR (W/kg)	$(B1rms)^2$ (uT^2)	Average Power Measured by Scanner (W)
Human Subject (200 lb) Chest landmark	1.19	7.47	158.27
Phantom Center landmark	0.80	7.40	92.56
Pig (125 lbs) Chest landmark	1.09	8.32	148.17

Anatomic Positioning

Anatomic positioning and initial in vivo testing in similar configurations demonstrated the dramatic difference in level of heating observed under theses circumstances compared to the “worst-case” phantom positioning. The wire was placed

across the iliac bifurcation representing a very superficial positioning and half-loop configuration which could represent one of the more clinically relevant “worst-case” positioning. Observed heating was less than a 1/20th of the maximum at the extreme off-set. Figure 4.2.7 shows images or photos the various positioning compared and the relative levels of device heating. A considerable difference (~30%) in the two temperature sensors was also observed particularly for the higher heating levels.

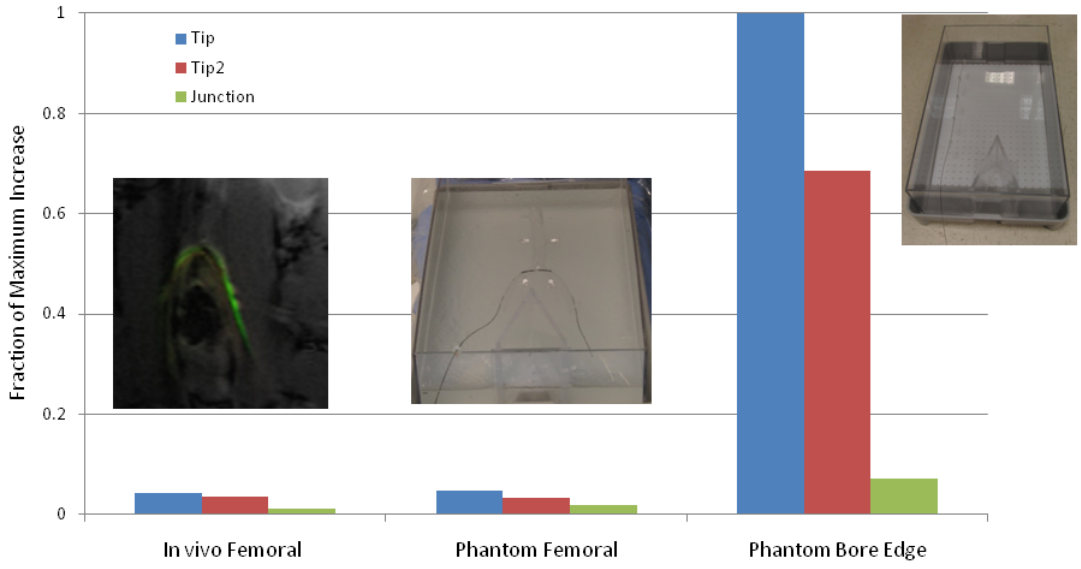

Figure 4.2.7. Realistic positioning in phantom and initial in vivo animal trials compared with phantom edge placement.

4.2.3 Discussion

Phantom testing demonstrated the importance of device positioning (horizontal offset and depth) on the level of heating observed and correlation to the predicted E-field and SAR distributions from simulation. Isocenter positioning was further inter-related

with maximum heating seen at varying insertion lengths which further reflects the changing current distribution phantom as its position in the phantom is moved. The trends we observed in device heating correlate with the simulated E-field distribution and the experimentally measured E-field distributions and corresponding implant heating recently described by Nordbeck and colleagues (130,131) for varying offsets and insertion lengths. Practical device testing and considerations with passive devices have also presented similar trends (132,133).

Critical insertion lengths not only were located in these high E-field region areas of the phantom but held for centrally placed wires as well. While the half-wave length in water with a dielectric of 80 like our phantom is approximately 26cm, the devices are comprised of different conductors and have thin layers (0.002-0.004") of exterior insulation with much lower dielectric constants which slightly increases the resonant length (Equation 4.2.2). Blood has a dielectric constant of 86 which is closely represented by the phantom formulation and a similar peak may be expected *in vivo* for certain insertion lengths.

Equation 4.2.2. Wavelength with varying dielectric.

$$\boldsymbol{\lambda} = \frac{\boldsymbol{\lambda_{air}}}{\sqrt{\boldsymbol{\varepsilon_r}}}$$

λ= wavelength
εr = diectric constant

Coaxial cable may have an appreciable change on guidewire heating in addition to signal loss and should be considered or eliminated if possible. This effect can be further influenced by the device insertion length and the circuitry used which may be altering the total electrical length of the wire. Certain lengths may cause the effective wire length to reach unfavorable multiples of a half-wavelength with increased heating. The cables themselves can act as linear or looped antennas depending on orientation

and interact with the B and E-fields that may extend beyond the confines of the transmit coil, particularly in short-bore magnets. At a minimum, the cables should contain cable traps or chokes like receive coil connectors to limit induced currents and having them act as antennas as well. As an alternative to the use of coaxial cables, we also developed an adapter that could connect the guidewire directly to the Siemens multi-channel preamplifier. The preamplifier has a flex connector which was customized to have a BNC connector input and the wire was then connected by a handle containing the circuitry which can rotate freely on the connecter for necessary torque application (Figure 4.2.8). This facilitated phantom testing where coaxial cable positioning and orientation may influence measured values particularly for device comparisons. The preamplifier and adapter could be covered by a sterile bag and positioned in the sterile field for use. Testing was performed to confirm that this preamplifier and adapter did not have an effect on device heating compared to the multi-channel preamplifier previously used.

Figure 4.2.8. Flexible adapter to preamplifier with guidewire handle to eliminate coaxial cable extension.

For the one-meter long guidewires tested, little impact was seen with changes to the externalized guidewire with the RF shielded or use of a floating trap. The RF shield does not prevent the RF exposure at the ends of the tube. For both options, with a large

portion of the guidewire inserted into the phantom, the externalized part only represents a small portion of wavelength in air (dielectric constant = 1) with the insulation only shortening that slightly. As with prevention of RF surface burns in patients, non-inserted portions of devices should be kept from the edge of the bore, particularly avoiding any contact with bore wall, and as midline as possible to avoid any potential interactions with the E-field. Again, this effect may be more pronounced in short-bore magnets depending on how much the E-field extends beyond the transmit coil end rungs. Operator contact could also slightly alter the device heating, particularly in heavily insulated wires.

In addition to being acutely sensitive to device placement, level of measured heating is also highly dependent on temperature sensor positioning. This critical sensor positioning has also been documented in the literature (134). We had reasonable repeatability in temperature sensor placement by marking the monitoring locations but that does not necessarily ensure proper positioning and measurement of the maximally heated point. With only a few millimeters difference in positioning of the sensors in the final example, a 30% difference was observed and it is unknown whether that represented the maximum. This motivated some of the work described in the section following to improve the characterization of the device heating profile particularly in these complex device constructions.

Whole body SAR values determined by calorimetry measurements were consistent for the scanner and phantom we used. Ensuring the correct coil file parameters was critical for this scanner estimation to be accurate. Additional considerations must be taken into account for the difference in applied power and SAR calculations that may exist between heating phantoms and animal or human measurements due to the variations in composition. The phantom is a homogeneous

solution whereas animal and human compositions are clearly not. This can impact the RF power penetration, reflection and distribution. Measures like the root-mean-square of B1 (B1rms) may provide a more conservative estimate of the power since there can be a large variation in SAR for a given B1 applied and will depend on the individual composition. Scanner manufacturers are now reporting these values as part of the new IEC standard development. The amount of power deposited should be matched as closely as possible or overestimated during phantom testing to determine the level of SAR amplification due to the device and further simulation can inform the relative values of local SAR in the phantom testing regions and actual human placements.

Despite the range of heating observed in the phantom with the typical edge offset heating given all these variables and their interdependence, minimal heating was observed with anatomic configurations which were also supported with initial *in vivo* guidewire positioning with temperature measurements. The edge of the phantom represents a high E-field environment that may not be experienced *in vivo*, particularly when the device is constrained to centrally located vasculature. Heating *in vivo* is also ameliorated by blood flow and temperature regulation. These are among the components we explored in the subsequent part.

4.3 *In vivo* heating evaluation

In this section, we aimed to better characterize and monitor potential device heating during normal use through *in vivo* studies in large swine. We demonstrated initial measurements in vivo with securely attached external temperature sensors but this precluded the use of many accompanying devices like small catheters and would not be feasible to allow regular use of the device with temperature monitoring. Our group has pursued modifying the device design to incorporate space for an internal temperature sensor which would allow real-time device temperature monitoring during regular device use first for evaluation in pivotal animal studies and then initial clinical trials as an additional safety measure and method to validate EM simulations for realistic trajectories in human models. Thermistors and thermocouples have been placed in functional devices such as EP catheters to monitor ablation temperatures including some demonstrations under MRI (135-137). These measurement techniques are less favorable in the MR environment but fiber-optic sensors like the ones used for the device testing described earlier now are available in sufficiently small constructions to be incorporated into the devices for a RF immune temperature measurement technique. We wanted to examine appropriate locations to monitor and whether the internal temperature measurements would provide a conservative measure of the external device temperature which would be in contact with the blood and tissue.

Providing a polyimide port for a temperature sensor on the insider or outside of the device during development could first provide a method to efficiently determine the complete heating profile by moving the sensor along the entire length of the device to determine appropriate monitoring locations during initial testing. Figure 4.3.1 shows a sample guidewire with a normal 0.035” external profile that has a temperature sensor

polyimide along the inner rod and proximal hub where the temperature sensor could be inserted and adjusted.

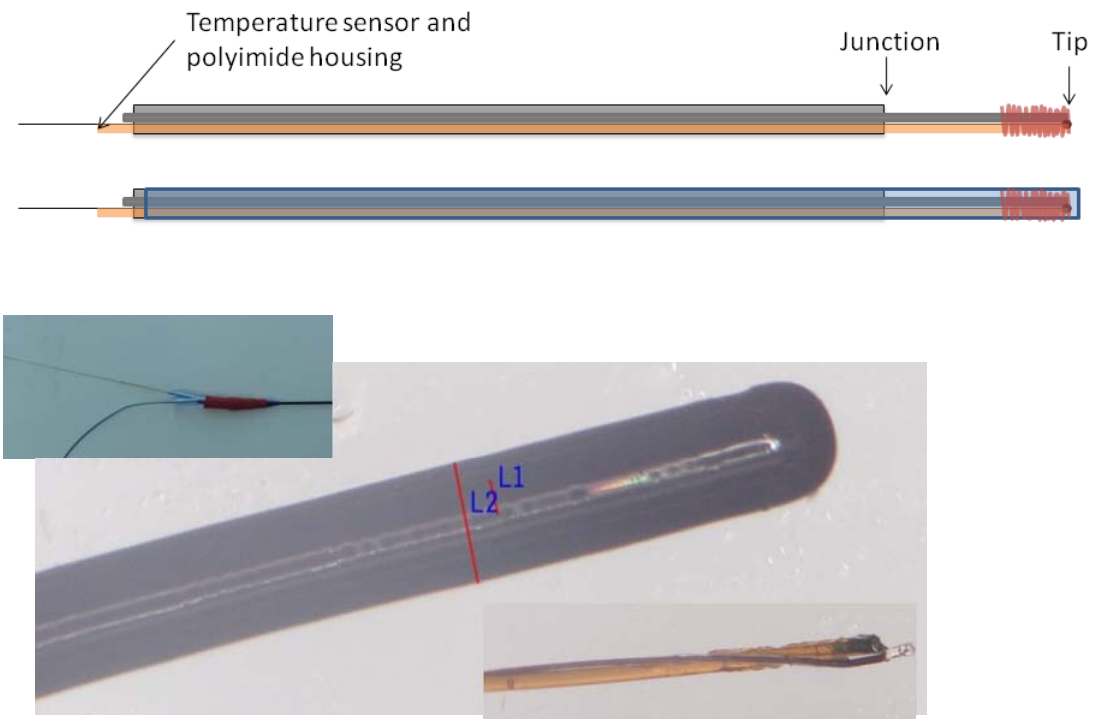

Figure 4.3.1. 0.035" Active guidewire with internal polyimide port aligned with the inner rod which is accessible proximally at the hub to move the sensor along the device.

In this part of the work, we present an analysis of the internal temperature monitoring approach and how it reflects external temperature measurements which would actually impact the local blood and tissue environment. We then demonstrate *in vivo* temperature monitoring with normal device use with an internal temperature sensor and explore the additional reduction in heating provided by blood flow with comparisons of *in vivo* and *in situ* measurements in swine.

4.3.1 Methods

Inner and outer device heating profiles and validation

Device heating profiles were determined to examine potential monitoring locations with the guidewire positioned in the phantom as described in the previous section. A 62.5 micron temperature sensor (Opsens, Quebec, CN) was placed in the internal polyimide tube all the way to the tip. Prior to any scanning, the temperature sensor first was moved along the entire length of the device to see the baseline fluctuations in phantom and air temperatures (Figure 4.3.2). The moving temperature sensor reflected variations in the ambient temperatures with the phantom slightly cooler than the air with a drop where the wire exited the phantom which is more watery on the surface with less gel and may experience evaporative cooling to cause the brief temperature drop.

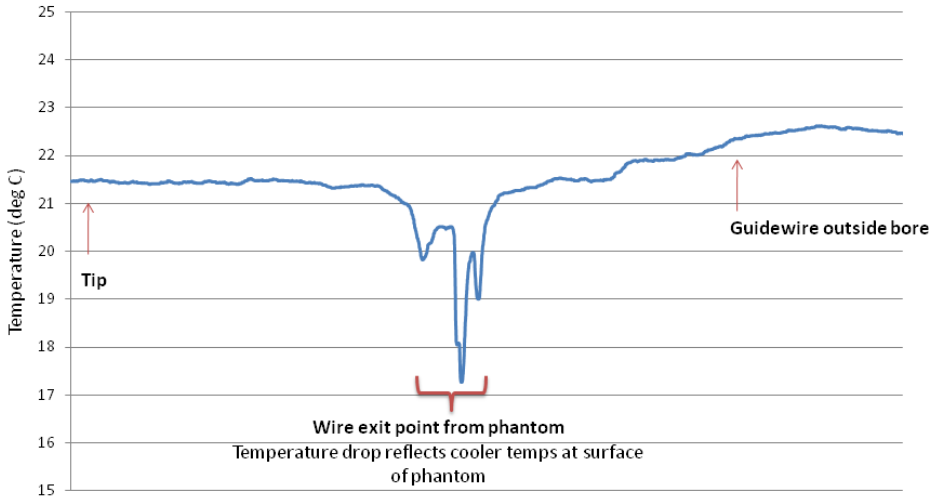

Figure 4.3.2. Absolute temperature profile reflecting ambient temperature along the wire in phantom prior to any scanning.

With the temperature sensor repositioned at the tip, scanning was started and once the temperature increase had reached a plateau, the sensor was pulled back at a near constant rate to determine the heating profile from the tip all the way through to the proximal connector end. Internal temperature profiles were also acquired with a catheter covering the proximal wire as would occur during a procedure.

Once this unmodified data had been acquired, a 0.010”ID/0.012”OD polyimide tube (MicroLumen, Tampa, FL) was affixed to the guidewire exterior with very thin heat shrink (0.00025” wall thickness, Advanced Polymer, Salem, NH) as seen in Figure 4.3.3.

Figure 4.3.3. Guidewire shaft with two polyimide ports placed on either side to measure external heating profile.

The guidewire was then replaced in the phantom at the same location and the temperature sensor moved along the internal and external polyimide tubing. The location of maximum heating was determined and marked for the both the inner and outer sensor locations. The sensors then were fixed at these locations before both were run with a 30 second baseline, 90 second of scanning and 30 follow-up. The marked locations on the sensor were compared with the two sensors and marked on the device. This procedure was followed for 3 different guidewires and one guidewire has 3 different

external polyimide tubings added at different positions along the circumference of the guidewire. Inner and outer measurements also were made at different applied power levels by changing the scan parameters. The outer/inner fraction was defined as the maximum outer heating divided by the maximum inner value.

In vivo temperature monitoring

A guidewire with an internal temperature sensor fixed at the maximum heating point was used for right and left heart catheterization in Yorkshire swine. A 100cm polymer catheter (Kumpe Access, Angiodynamics, Latham, NY) was used with the guidewire for positioning. Measurements were made throughout guidewire movement as well as testing performed at certain guidewire positions where the guidewire was held temporarily and a baseline was acquired, followed by the start and stop of a scanning interval to observe the temperature increase.

In vivo and *in situ* comparison

To examine the impact of blood flow and the potential heating that may be experienced *in vivo* in a low-flow area or occluded vessel, we conducted a comparison of the heating observed with the same device placement *in vivo* and then immediately after euthanasia. At the end of terminal experiments, the device with attached or embedded temperature sensor was positioned in the aorta or inferior vena cava and temperature acquisitions at 2 different flip angles were performed to artificially increase the power. The animal was euthanized in the scanner without any movement of the

animal or the device. The temperature acquisitions then were repeated. The heating curves and maximums reached were compared in the different conditions.

4.3.2 Results

Temperature Profiles

Moving the temperature sensor through the inner and outer polyimide tubes provided clear profiles of the areas of areas of device heating. The inner and outer profiles indicated the same regions of heating with higher values measured with the inner sensor. Figure 4.3.4 shows comparable internal and external temperature profile for the entire guidewire length.

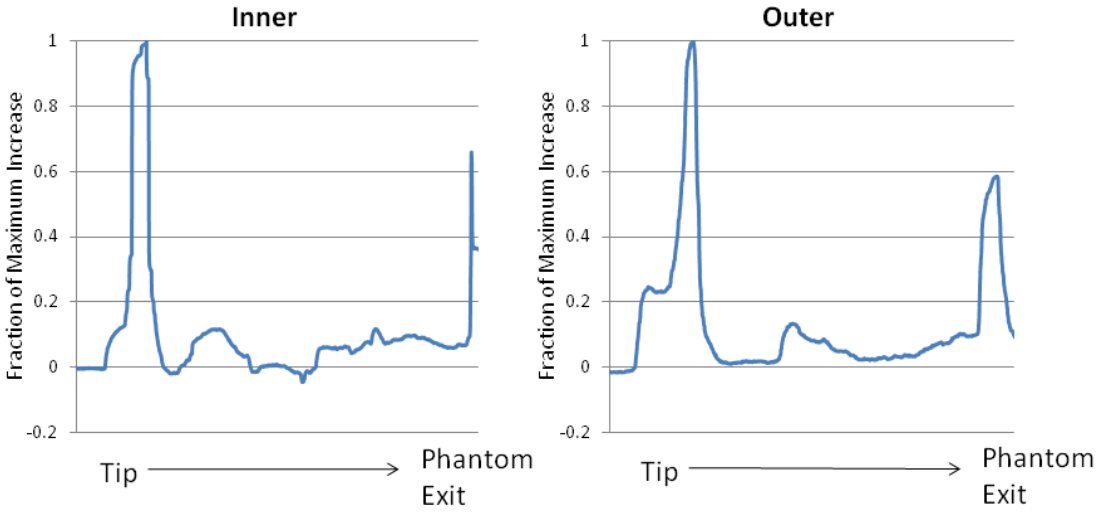

Figure 4.3.4. Inner and outer temperature profiles as the sensor is moved along the guidewire length.

The inner device profile did not change substantially with the catheter on the device other than slight changes in the relative heating of the junction and exit point of the phantom. Profiles from the tip through the junction are shown in Figure 4.3.5 for the bare guidewire in the phantom and with the wire extending 5cm beyond the end of the catheter. This was also done for the guidewire 15cm beyond the catheter with the same profile. Changes in device heating along the wire were observed on varying insertion length depending on the device construction with the most noticeable changes occurring with decreases at the wire end and relative increases in the heating at the hypotube junction and exit point of the phantom.

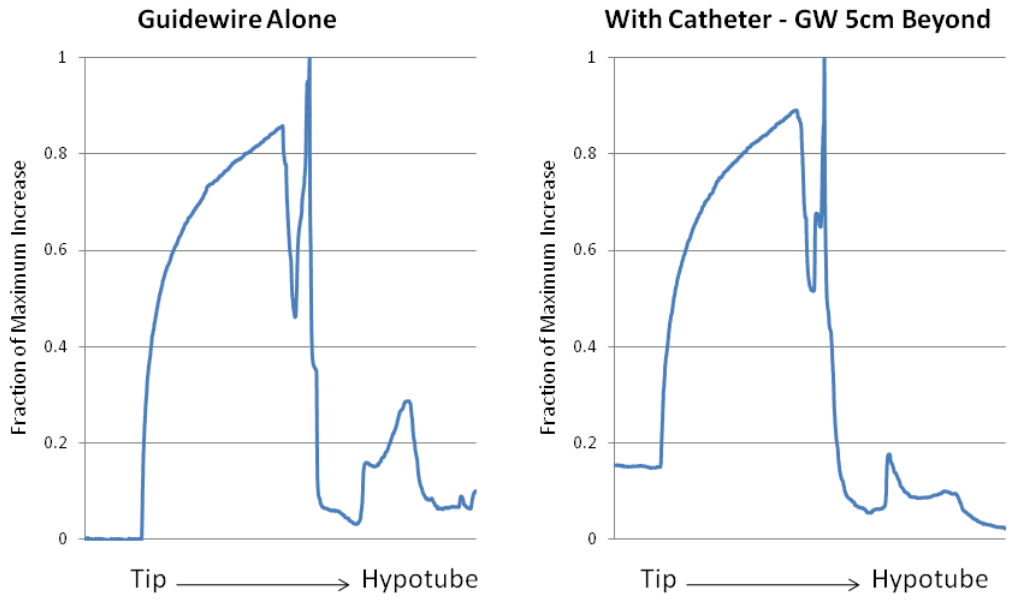

Figure 4.3.5. Distal heating profiles with and with a catheter.

Inner and Outer Comparison

The locations of maximum heating on the guidewire were the same for the inner and outer temperature profiles at the given placements with lower heating always observed with the outer temperature sensor. The shape of the heating curves did not differ in the initial rise other than the maximums achieved (Figure 4.3.6).

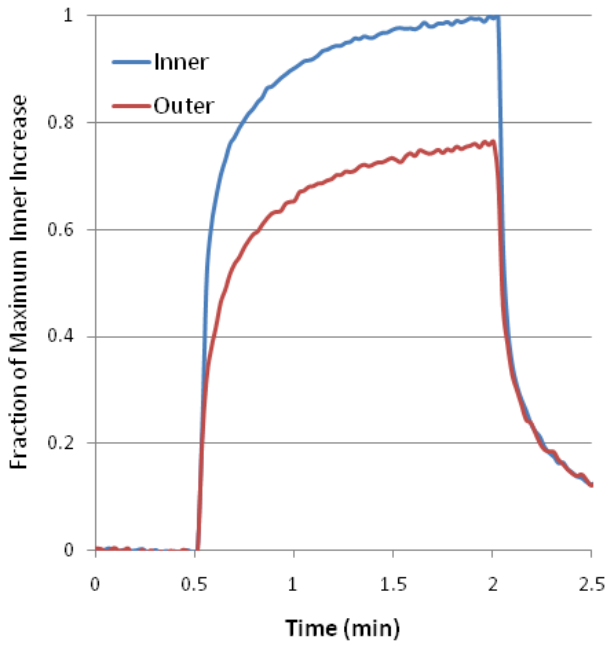

Figure 4.3.6. Simultaneous inner and outer temperature measurements at maximum point.

For the guidewire with 3 external polyimide locations tested, the fraction of outer to inner heating varied from 66 to 79%. The other 2 guidewires tested had slightly higher fractions near 80%. The outer/inner fraction averages and standard deviations are

shown in Table 4.3.1 for the 3 different polyimides in the same wire as well across 3 different wires.

Table 4.3.1. Outer/inner heating fraction.

	3 external polyimides on same guidewire	3 different guidewires
	Outer/Inner Fraction	
Average	0.74	0.81
Standard Dev	0.07	0.065

With variations in power applied, the maximum levels of inner and outer heating decreased as expected. The absolute difference between the two measures decreased linearly with applied power and maximum heating level (Figure 4.3.7). The relative fraction remained fairly constant with an average of 0.76 ± 0.04 in the guidewire tested at 6 different power levels.

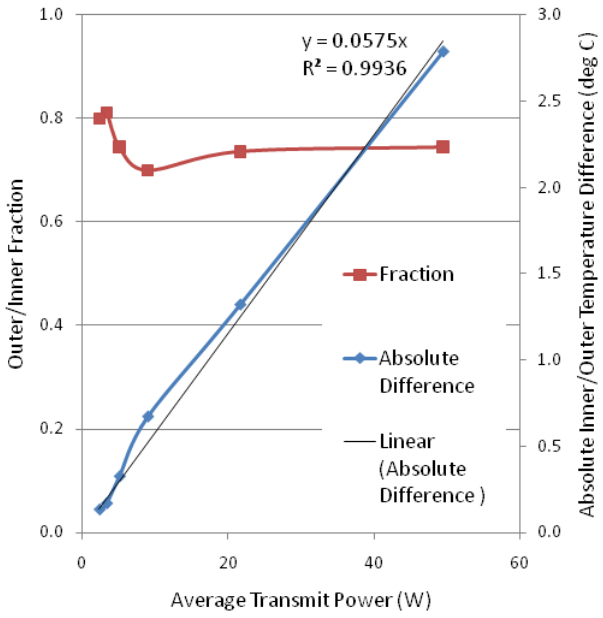

Figure 4.3.7. Outer-inner fraction and absolute difference for varying transmit power.

<u>*In vivo* temperature monitoring</u>

The guidewires with embedded temperature sensors were successfully used to access the right and left heart *in vivo* in swine with commercial polymer catheters. The temperature fiber did not impede device use or performance and the internal sensor provided constant temperature monitoring *in vivo* throughout the simulated procedures. Active devices require a connection to the scanner and the temperature fiber connection can be incorporated into the same handle for ease of use. Figure 4.3.8 shows a sample temperature recording with guidewire insertion into the vascular access sheath and blood pool.

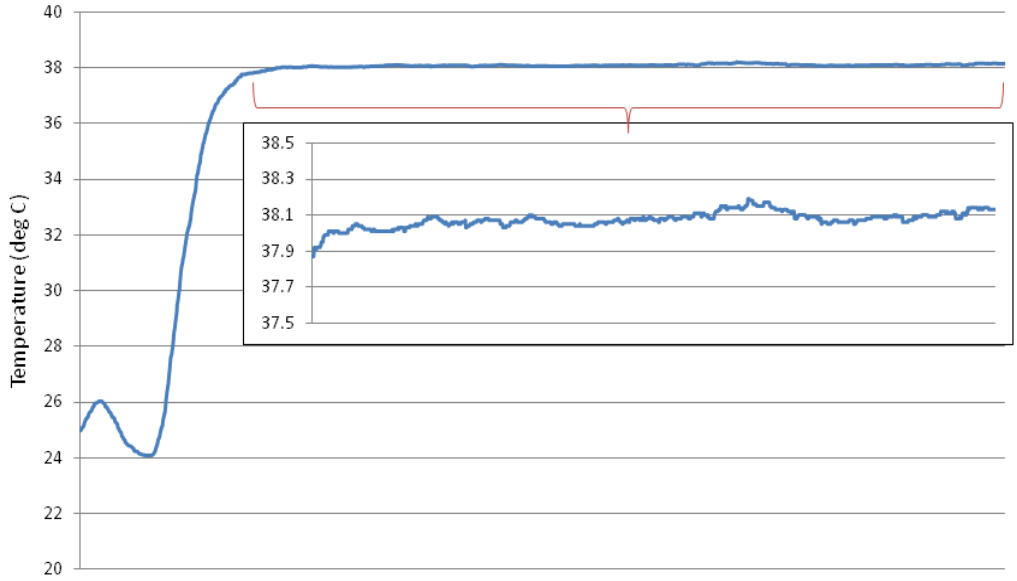

Figure 4.3.8. Temperature change measured as guidewire is inserted into sheath and into animal.

Several guidewires were tested *in vivo* with no appreciable heating beyond temperature fluctuations seen normally under normal scan conditions for placements in the aorta and IVC for right and left heart catheterization. With the central vessel locations and guidewire positioning, this lack of heating correlates with the typical E-field distribution at a minimum in the center of the bore and animal. By increasing the power and using devices with known unacceptable heating profiles, we were able to observe the continual temperature fluctuations throughout use and demonstrate the ability of the system to track temperature changes during *in vivo* use. Figure 4.3.9 shows the internal sensor temperature readings as the guidewire was moved from the end of the sheath, up the aorta, and into the left ventricle. Slight heating was observed when scanning was started and then variations with peaks and valleys seen as the guidewire was moved along its insertion.

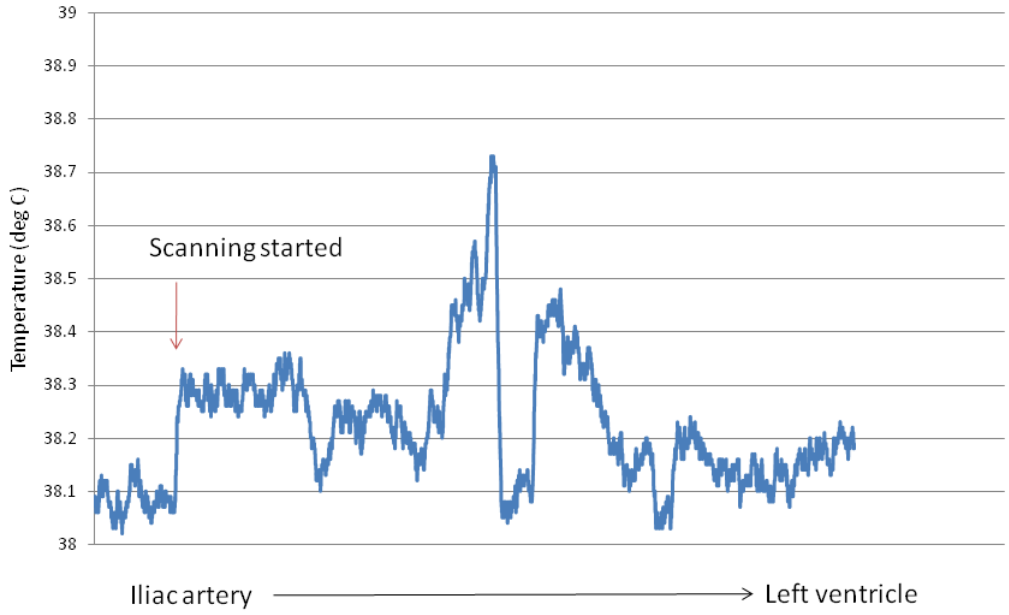

Figure 4.3.9. Temperature recording during LV entry with guidewire with known high heating.

With the guidewire in place around the aortic arch in the LV forming a curve, a temperature acquisition was run that did not produce appreciable heating beyond the normal temperature fluctuations which was consistent with the end of the moving profile seen above (Figure 4.3.10). These curvatures at the aortic arch, however, occurred with insertions lengths well beyond 60cm with the guidewire tip in the left ventricle.

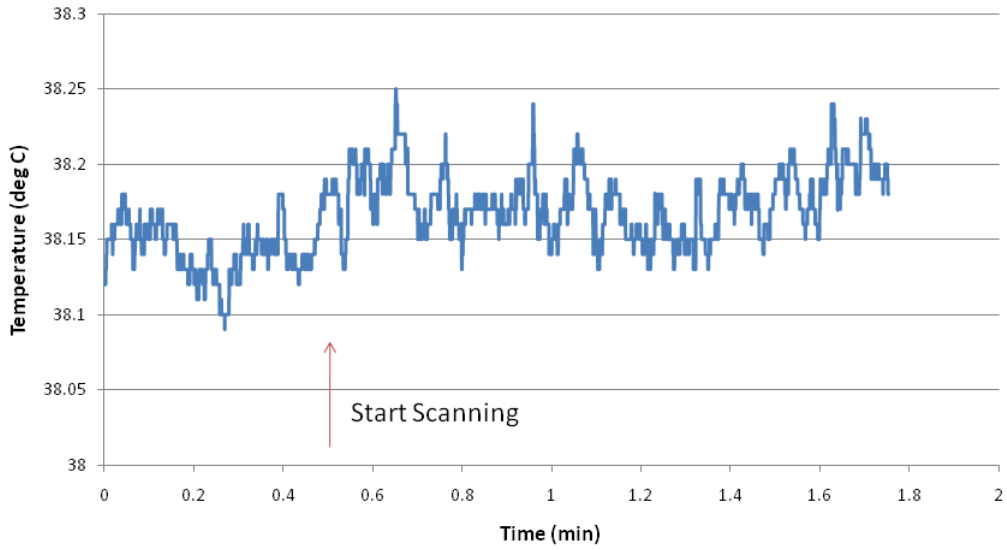

Figure 4.3.10. Temperature measurements with the guidewire positioned around the aortic arch into the LV with scanning for 1 minute.

Insertion lengths which produced higher heating in the phantom typically occurred in the most central placements of the large vessels. Fluctuations were also seen during aortic pullbacks in the devices with appreciable heating which may reflect these small increases at critical lengths. Less favorable placements with semi-loop configurations and superficial vessel locations produced little heating (<0.5°C) compared to higher values measured in offset phantom studies.

In vivo and *In situ* comparison

Temperature increases *in vivo* were on average half of those measured *in situ* immediately after euthanasia. This was consistent across guidewires and with the different input powers and maximum heating achieved (Table 4.3.2). There was no difference in the fraction seen in the guidewires placed in the aorta versus IVC.

Table 4.3.2. Maximum increases in vivo and in situ and fraction difference.

n=6	Max Increase *In vivo*	Max Increase I*n situ*	*In vivo/In situ* Fraction
Average	0.36	0.71	0.52
Std Dev	0.17	0.38	0.071

In both *in vivo* and *in situ* measurements, heating increased acutely and then steady state was readily reached. With continual scanning, the temperatures fluctuated around the maximum value without any further increases or observable gradual cooling (Figure 4.3.11).

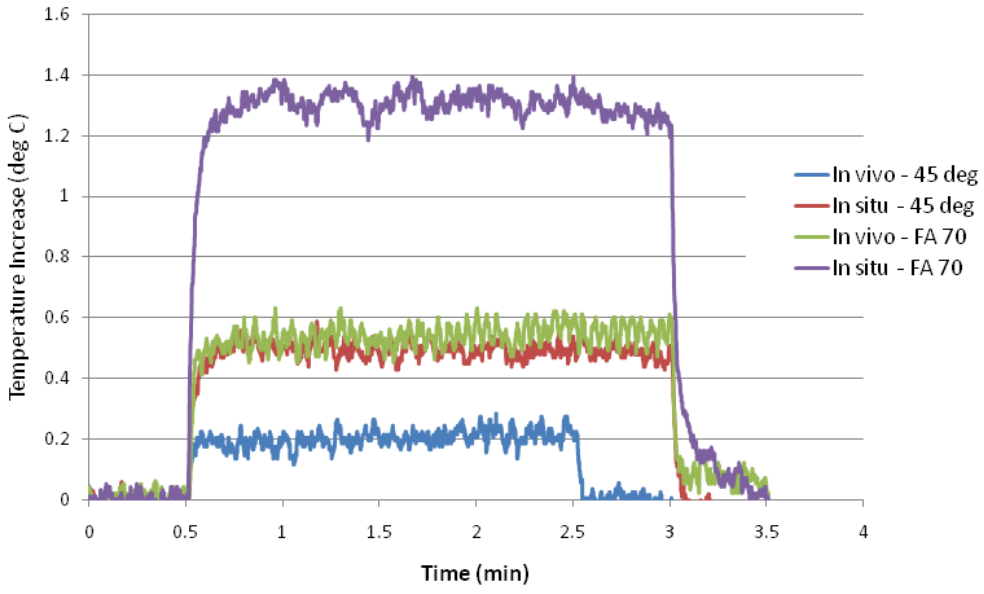

Figure 4.3.11. In vivo and in situ heating curves at varying flip angle.

4.3.3 Discussion

In this section, we presented an evaluation of inner temperature monitoring with inner and outer temperature sensor comparison and *in vivo* demonstration of temperature recordings. Moving the temperature sensor along the inside and outside of the device provides a more efficient and accurate method to fully characterize the device heating profile and determine the areas of maximum heating. In our experience, movement of the sensor by millimeters either direction of the peak points could have a significant effect on the values measured. In trying to compare device constructions or iterations, this helps ameliorate the concerns about exact temperature sensor placement during trials and the true maximum points can be found and tested. The approach of placing an external thin-walled tubing to enable the slidable temperature sensor could be adapted for testing of any device to determine the entire profile. Afterwards, the standard approach of placing temperature sensors at the specific points directly on the guidwire could be used for confirmatory testing. This would provide more reliable placement of these sensors and ensure that the proper spots are being monitored.

Another approach we initially tried to monitor heating along the entire device profile was liquid crystal heat-sensitive paint (Edmunds Scientific, Tonawanda, NY). This could be applied to the device with little increase in profile and changes color depending on the temperature reached. These paints, however, are generally water-soluble and would come off in phantom testing if not otherwise covered. Monitoring the color change during scanning is also challenging. Thermal paint or heat-sensitive paper may be useful for measurements where RF current is directly injected in the device in a bench-top testing method. MR based thermometry is a powerful tool for monitoring tissue temperatures in RF or cryoablation type therapies but is still technically challenging for device temperature monitoring. The phase based measurement is

typically limited to temperature resolutions of 2 degrees and would need to have high spatial resolution to observe the heating immediately at the wire. Additionally, the presence of the device in the imaging field can disrupt the homogenous field and accurate quantification of phase changes. Infrared imaging may be another possibility but typically measures surface temperatures so modifications are necessary to make measurements near the device.

We did observe slight differences in the temperature fractions measured with the three external sensors affixed to the same wire which could be attributed to several potential factors. While we are able to determine the maximum longitudinal point, there may be some asymmetry in the device heating depending on the heat source and its location relative to the midline of the device. Slight variations in the exact maximum point chosen could also contribute to this difference. Additionally, slight differences in the polyimide thickness or heat shrink surrounding could also cause small fluctuations. As shown, the circumferential maximum point also should be considered and tested with sensors around the outside along with the longitudinal position particularly when the maximum heating point source is unclear.

The points of maximum heating remained consistent for the conditions tested with and without the catheter and during failure states. This may not be the case in different device designs and must be considered. Additionally, device positioning, circuitry and connection status could alter the device heating profile depending on design. In these cases, the areas to monitor during *in vivo* use may not always been the maximum point under all conditions and monitoring the locations where differences in heating are the most dynamic and present the greatest risk of maximum heating likely is a better approach. In a loopless guidewire design, for example, the tip or incorporating a distal coil may results in the most variability in temperature measurements but the

junction has a background level of heating in all positioning that may on occasion exceed the tip levels when they drop considerably. However, this level of heating is relatively low even in extreme offsets.

The inner and outer temperature sensor comparison indicated for the conditions we tested that the heating measured inside the wire did not exceed the external measured values. This suggests that the inner temperature can be monitored with the expectation that the outer temperature which would impact the local blood and tissue environment would not exceed the recorded value. The fractional difference between these measurements was generally consistent for varying power levels but the absolute differences varied linearly with power applied and maximum increases. This might suggest a conductive heating model (Equation 4.3.1. Conductive heat transfer equation) where the fraction is dependent on the device construction which can alter the type (changing k) and thickness (d) of the insulation used and the characteristics of the heat generating point (A).

Equation 4.3.1. Conductive heat transfer equation

$$\frac{\Delta Q}{\Delta t} = \frac{kA}{d}(\Delta T)$$

ΔQ/Δt = rate of heat transfer
k = thermal conductivity
A = cross-sectional area of heat transfer
d = thickness
ΔT = temperature difference (T_{hot}-T_{cold})

Consequently*, in vivo*, without any device heating, the measurements by the internal temperature sensor actually may be slightly lower than the external blood temperature since the exterior temperature will likely be higher than the inner until the values

equilibrate or there is minimal device heating. Convective heat transfer from blood flow could further decrease the maximum levels of heating levels appreciated on the exterior by more quickly dissipating the heat at the guidewire surface which may further reduce the outer/inner fraction. The main risk if that this relationship could be altered by unintended insulation defects in the device at which point the device should be removed from use.

As discussed in the previous section, the local SAR environment is likely the most critical factor along with device insertion length and orientation relative to the tangential E-field. While we tested larger swine between 100-200 lbs for many of our heating studies to have similar power inputs and loading on the body coil, their shapes and composition differ from the human (Figure 4.3.12). Body habitus, fat versus muscle composition, lung shape, and positioning and size of vessels could all impact the local SAR environment.

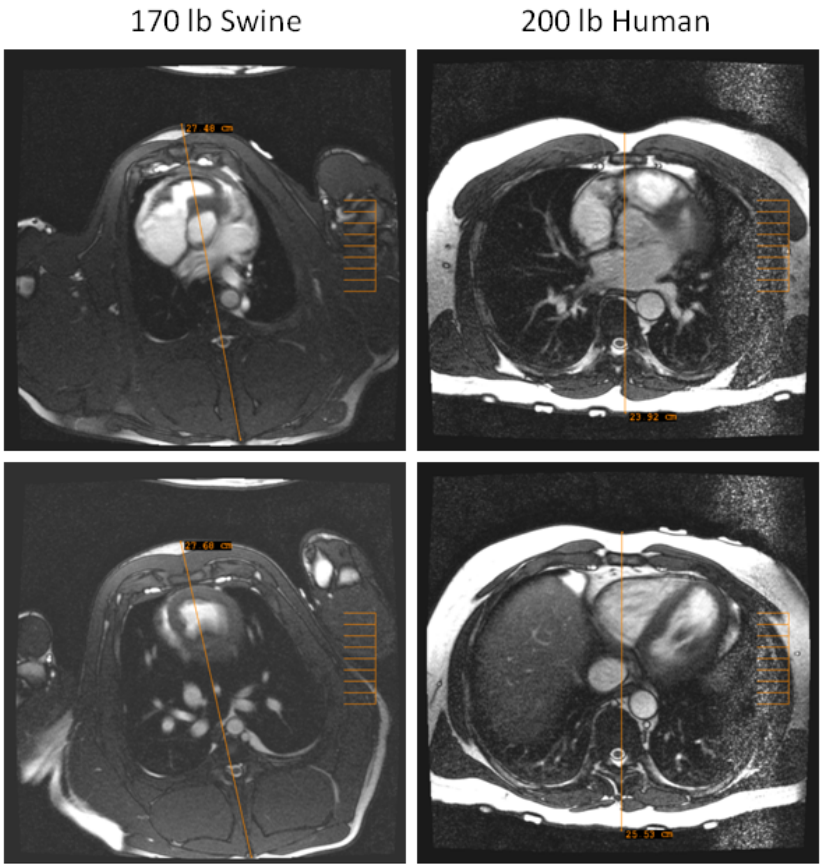

Figure 4.3.12. Cross-sectional images of swine and human chest at cardiac base (top) and apex (bottom) levels with differences in muscle/fat presence, anterior-posterior depth difference, and lung shape.

Fat provides a good insulator compared to the more conductive muscle to limit RF power penetration where as smaller vessels in a large lung field could concentrate the E field in that region. Additionally, anatomical differences could also translate into varying device positioning relative to the tangential E-field. Electromagnetic simulation could help to inform the impact of these differences and the extremes that must be considered with the internal temperature monitoring providing an additional ability for in vivo validation of simulation results in animal studies and initial clinical trials as well as an important safeguard.

Comparing *in vivo* and *in situ* heating measurements at the same location provided a fairly consistent 50% heat reduction with different levels of maximum heating and large vessel location. These measures were taken with the device in full flow areas of large vessels (aorta and IVC) which likely represent the maximum benefit that perfusion will have in additionally reducing any perceived heating. Since considerable heating wasn't seen with device use *in vivo*, these fractions also only represent behavior up to around 1 degree of heating *in situ*. They are consistent with computational studies of blood flow contributions which observed a similar 2-fold decrease with normal blood flow (138). Given the blood flow, these temperatures also are likely only seen in the immediate vicinity of the device and quickly dissipate into the vast heat sink of the blood pool with little impact on overall core temperature. We attempted to investigate the risk of vessel wall heating with device contact but high enough heating wasn't observed in vivo and testing with freshly explanted tissue in a phantom to produce higher heating still did not produce any histologic findings.

In summary an internal integrated temperature probe inside a conductive MRI guidewire appears to reflect external temperature measurements without impairing normal device use. *In situ* animal catheterization experiments model *in vivo* heating while suppressing the heat sink effect of flowing blood, and perhaps better model use-mode heating than *in vitro* measurements. These support follow-on engineering for continuous temperature monitoring as a strategy to help monitor safety of active MRI catheter devices.

4.4 Device Monitoring and Dynamic Scanner Feedback Control System

Under normal use, we have observed minimal or no heating in simulated use during phantom and *in vivo* animal testing. Proper device use and components in device and circuitry design are used to reduce the potential for radiofrequency (RF)-induced device heating (139,140) and enable safe device performance. Atypical device use, loss of device connection to the scanner, or device failure could possibly exceed such protection mechanisms in rare instances. Identifying these events rapidly and altering scan parameters to reduce transmit power when pausing scanning may be detrimental during an intervention could quickly mitigate the heating risk and provide an additional mechanism to ensure safe device use.

Reasonable increases in RF pulse width and reductions in flip angle can substantially reduce deposited power, the induced E-field and subsequent device heating while maintaining acceptable image quality. The applied RF energy produces a B1 magnetic field perpendicular to B0 in addition to an electric field parallel to B0. The flip angle produced by a RF transmit pulse is a function of its amplitude, B1, and time it is applied, or pulse width (Figure 4.4.1). Increases in flip angle are directly related to the length and amplitude of the RF pulse (Equation 4.4.1) and the E-field is proportional to the amplitude. The electric field is minimal at the center of the body transmit coil but increases radially outward with high fields also seen near the end-rungs and capacitors (141) (Equation 4.4.2). SAR follows the square of B1 amplitude and E-field intensity (Equation 4.4.3).

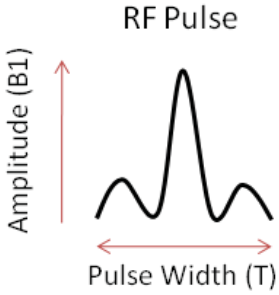

Figure 4.4.1. Diagram of RF pulse with amplitude and width.

Equation 4.4.1. Flip angle production from RF pulse characteristics.

$$\theta = \gamma \int_0^T B_1(t)dt$$

Equation 4.4.2. RF transmit induced electric field.

$$E(r) = \frac{1}{2}\omega r B_m$$

Equation 4.4.3. SAR calculation.

$$SAR = \frac{1}{2}\frac{\sigma}{\rho}E^2(r)$$

$$SAR\ \alpha \int_0^T B_1^2(t)\,dt$$

θ = flip angle
B_1 = amplitude of RF
E = associated E field
SAR = specific absorption rate
T = time RF applied
γ = gyromagnetic ratio
ω = angular frequency (2πf)
B_m = mean B1
σ = conductivity
ρ = density

Therefore, RF energy deposition decreases linearly with increasing RF pulse length and, additionally, the associated increase in sequence TR provides a further small reduction

in power. Figure 4.4.2 shows the average power applied as measured and reported by the scanner with varying flip angles and pulse width.

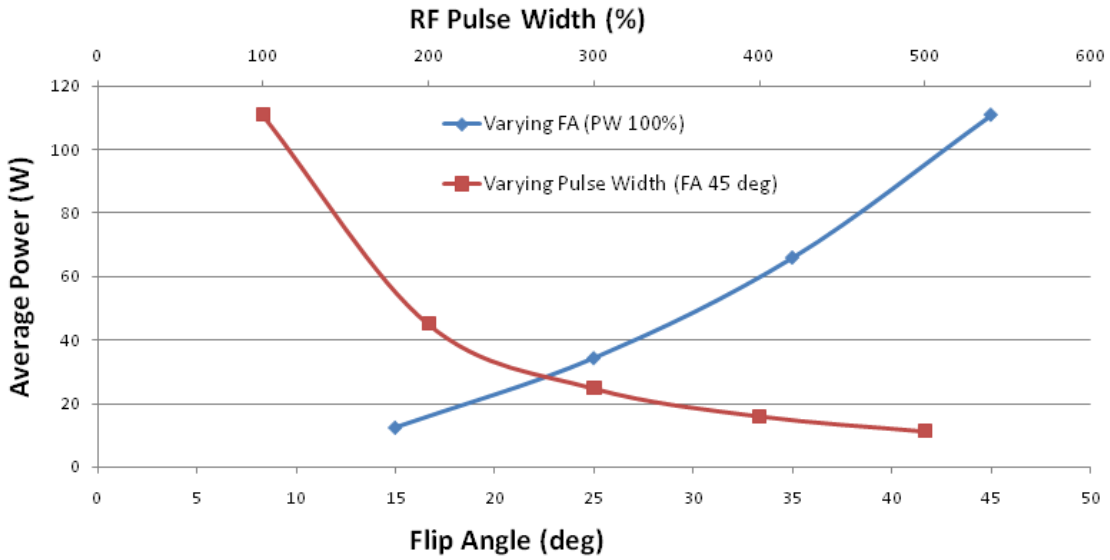

Figure 4.4.2. Average deposited power versus flip angle and pulse width (reported in %, 100% = original value (500 microsecond)).

The TR of a balanced SSFP sequence can be increased to ~5.5ms for a 5-fold lengthening of pulse width without incurring too many off-resonance artifacts for typical cardiovascular interventions.

In this work, we developed and demonstrate a system to monitor proper active device performance and provide an additional safeguard with dynamic scanner feedback control during MRI-guided interventions. Signal and noise levels from the device channel could indicate device connection and performance status which may result in an increased risk of device heating. Safety monitoring inputs such as temperature readings

described with the approach in the preceding part could further inform the proper operating status and appropriate scan parameters.

4.4.1 Methods

Sequence modifications and communication

A modified real-time balanced SSFP sequence was used which provided a brief sample device noise (RF transmit off) and then signal after a 2 degree non- selective pulse prior to each real-time slice acquisition to confirm device connection and signal. Additionally the sequence included a) features for real-time adjustment of RF pulse length and flip angle, and b) a “fail-safe”, which was automatically activated if the sequence was not perpetually informed that the active device was functioning appropriately. If the device or monitoring system became disconnected (and thus stopped sending data), the fail-safe would force the sequence into a “safe mode” with a long RF pulse (2500 microseconds) and a low flip angle (20 degrees) which decreases applied power almost 50-fold from normal acquisition parameters. *Sequence design and modifications done by Michael Hansen and J. Andrew Derbyshire.*

The noise and signal data were sent via a TCP/IP connection initiated by the scanner host to a custom LabVIEW (National Instruments, Austin, Texas) interface which monitored and analyzed the changes in device signal input and device temperature through a fiber optic sensor attached to an active device. The LabVIEW monitoring tool was programmed to send a reply to the scanner confirming proper performance and with any changes in pulse width or flip angle to the protocol control

according to device status and heating. An overview of the system architecture is shown in Figure 4.4.3.

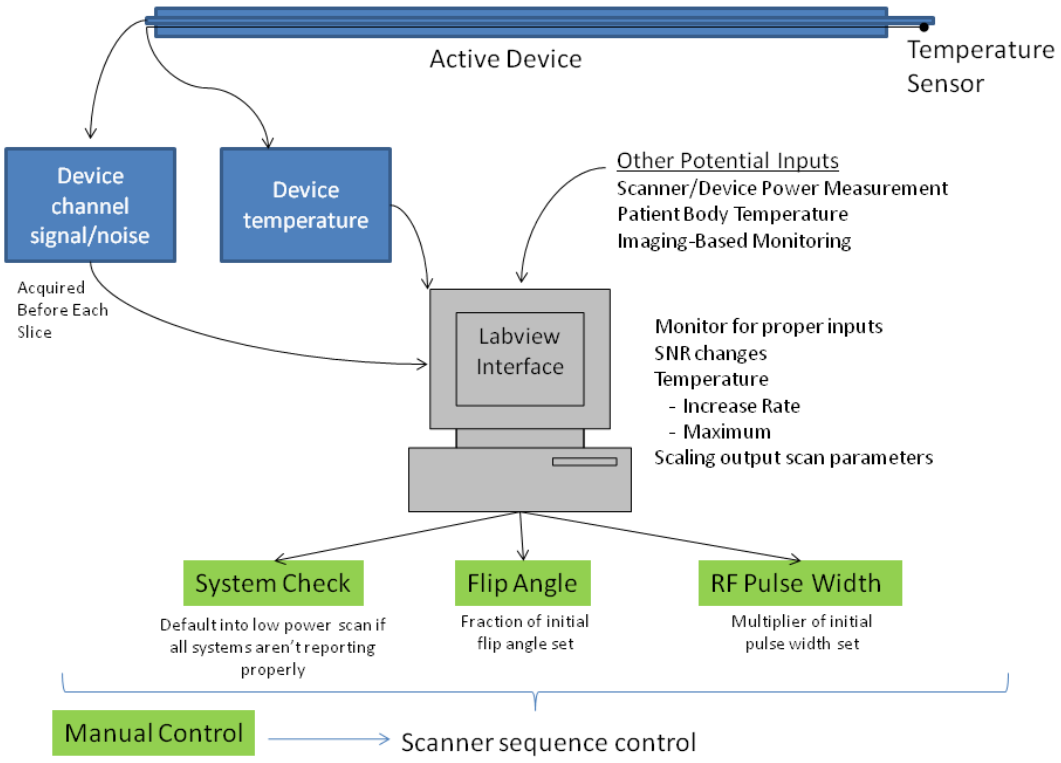

Figure 4.4.3. Overview of device monitoring and scanner feedback system design.

Temperature Acquisition and Processing

To input the temperature monitoring data to the LabVIEW interface an adapter was made to relay the analog output from the fiber-optic temperature signal conditioner (TempSens, Opsens, Quebec, CN) to a data acquisition board (PXI-6225, National Instruments, Austin, TX) for digitization. The interface was designed to be able to calculate a baseline temperature reading, increase from baseline, instantaneous

changes in successive temperature readings, and a linear rate of temperature increase from a moving window of the temperature data. Additional functions to filter the temperature signal where implemented with options for a moving average, smoothing, and a median filter. Figure 4.4.4 shows the temperature input and monitoring display of the system.

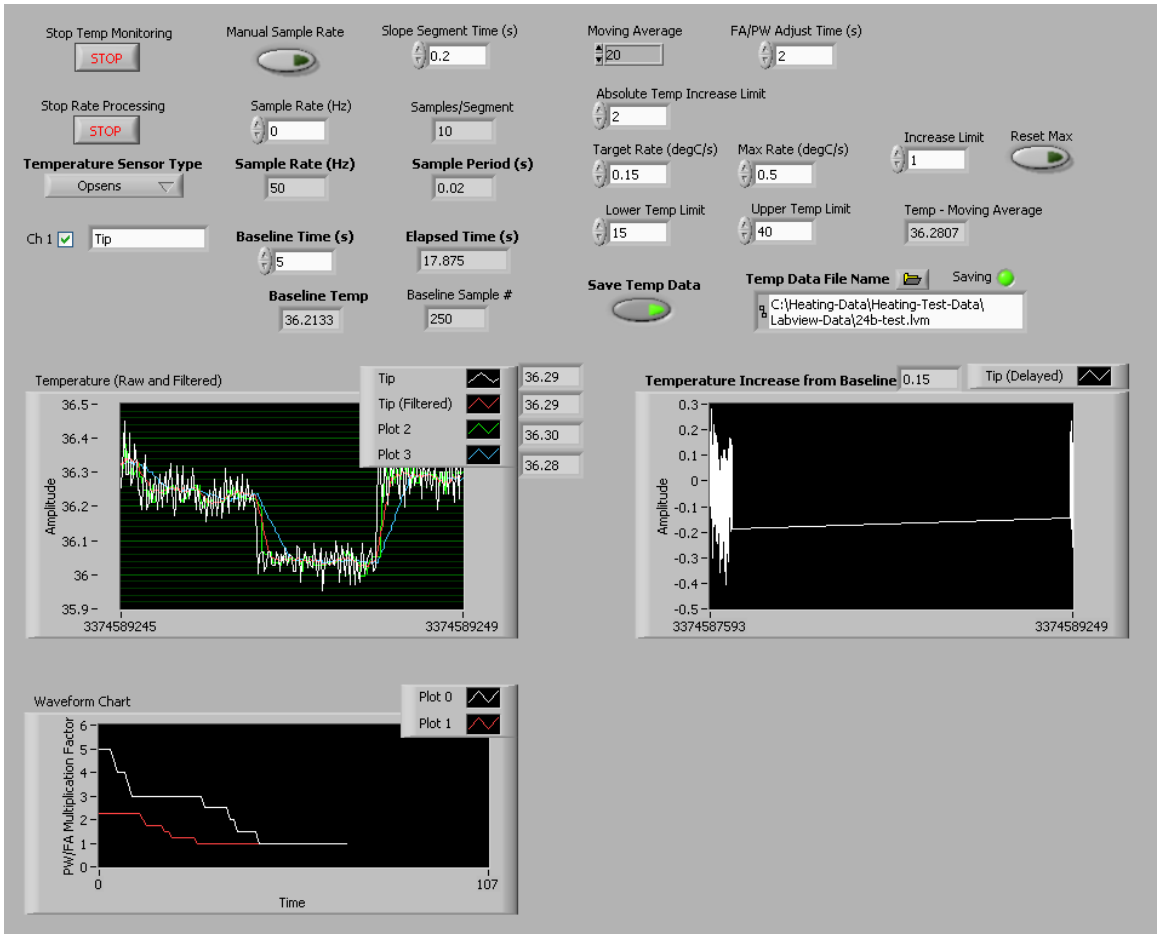

Figure 4.4.4. Temperature monitoring interface with temperature monitoring and gradually increasing power seen in FA and PW factor plot.

Phantom heating tests of active devices were used to determine acceptable initial temperature increase rates to maintain device temperature increases below desired limits and the impact of altering scan parameters on the temperature increases. To provide an accurate measure of the initial temperature increase slope, a LabVIEW program was used to collect and analyze the temperature data which incorporated a function sending a command to start the scanner at a specific timepoint after the baseline temperature acquisition window to ensure a consistent start of the applied power.

The temperature data input was used to determine the appropriate flip angle and pulse width to send back to the scanner. Depending on type of monitoring desired and limits selected, the program could be adjusted to alter the method of scan parameter control. To limit according to the rate of temperature increase rather than an absolute set-point, the increase rate was compared to a desired increase rate selected from the studies above to determine a power factor. The relationship between device heating and changes in flip angle and pulse width were used to determine the relationship between power factor and the corresponding adjustment in scan parameters which were outputted for communication prior to slice acquisition. The prior power factor was modified immediately if heating beyond the limits continued and could be adjusted to decrease appropriately if the calculated rates indicated a continual drop over a period of time inputted by the user. In another iteration, the flip angle and pulse width were continually increased from their default low-power values (FA 20° and PW 500%) until a given temperature limit was reached.

Device Signal Monitoring

For each device channel, the scanner acquired and sent 64 noise and signal samples over the TCP/IP connection. The root mean square of the signal and standard deviation of the noise were calculated and displayed in the LabVIEW interface. The fractional change in signal between each acquisition was also calculated continuously.

Signal and noise levels were measured with varying devices under different conditions to select appropriate limits for system response. Conditions tested included: device unplugged at connection to circuitry, component disconnected in circuitry, disconnected from preamplifier box, saturation pulse applied, and moving the guidewire in the field.

Additional System Controls

The interface was designed to immediately send a negative status report causing the scanner to default to the low power mode if any of the following instances occurred: (1) device signal/noise header and data was not fully received; (2) temperature data was not in range; (3) device signal dropped between during subsequent acquisitions in excess of user defined limit; and (4) temperature increase absolute value or rate exceeded user set limit. Alternatively, the scan parameters and operating status could be manually controlled with user controls in the interface and a switch from auto to manual mode. Figure 4.4.5 shows the display of the system checks, auto and manual controls, and signal/noise data. The sequence operation can also be paused through a command sent to the protocol control.

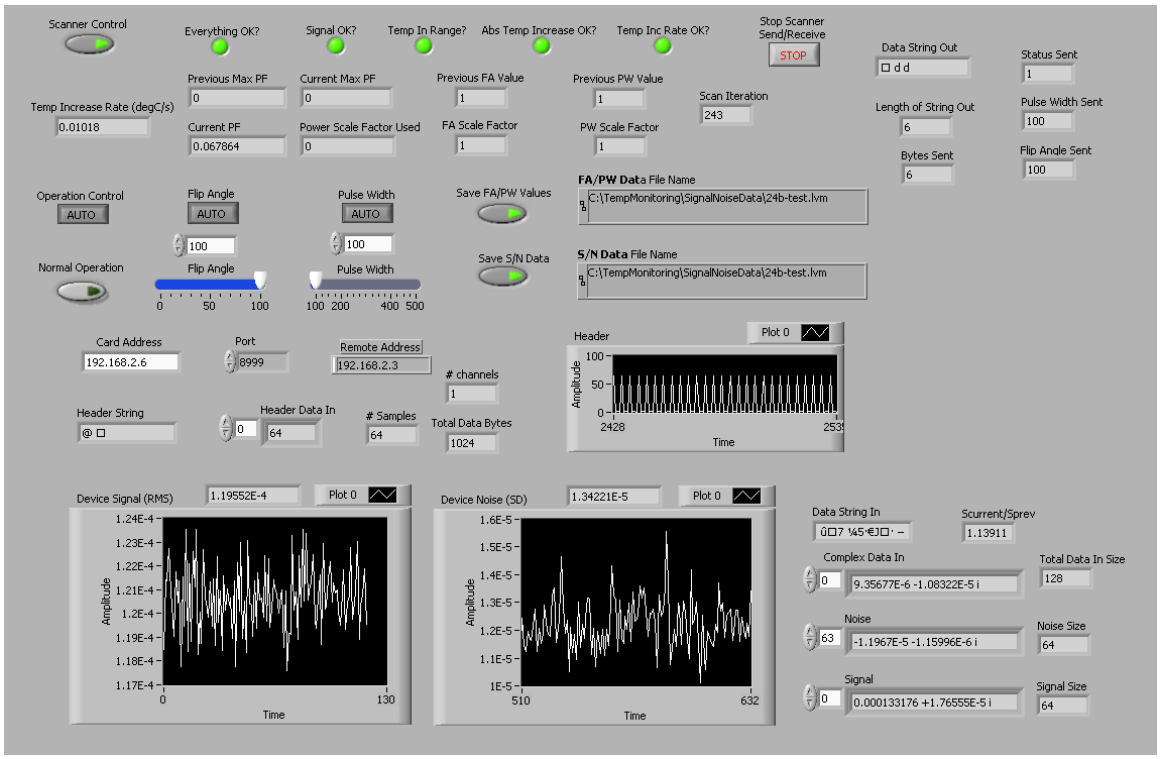

Figure 4.4.5. LabVIEW interface displaying status and device signal monitoring with both automatic and manual controls.

4.4.2 Results

The maximum temperature reached by a device closely correlated with the initial rate of temperature increase for varying flip angle and pulse width (Figure 4.4.6). This data provided the fit for the power factor scaling to determine appropriate scan parameter changes. With increasing pulse width, power and temperature increase dropped according to the pulse width increase factor to the four-thirds power. For flip angle, the power and temperature increases followed the square of flip angle as expected.

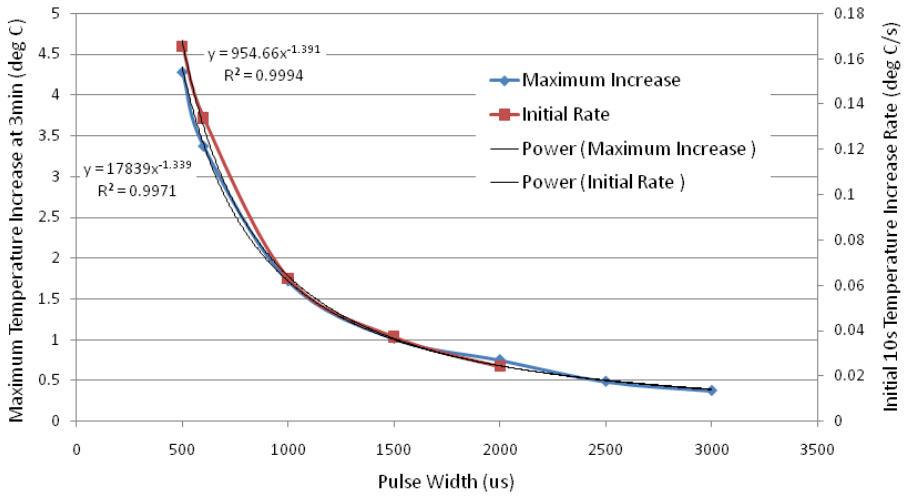

Figure 4.4.6. Temperature increase rate and maximum reached for varying pulse width with power fits.

Device signal and noise measurements decreased significantly when the device was unplugged either at the device connector (MMCX) or the connection of the circuitry to the preamplifier (BNC). Some signal was still appreciated with the MMCX unplugged as the circuitry contains some components which are tuned to 64 MHz and can act as an antenna. When a series component was disconnected in the circuit box, the signal also fell dramatically compared to three other measures in different configurations (Figure 4.4.7).

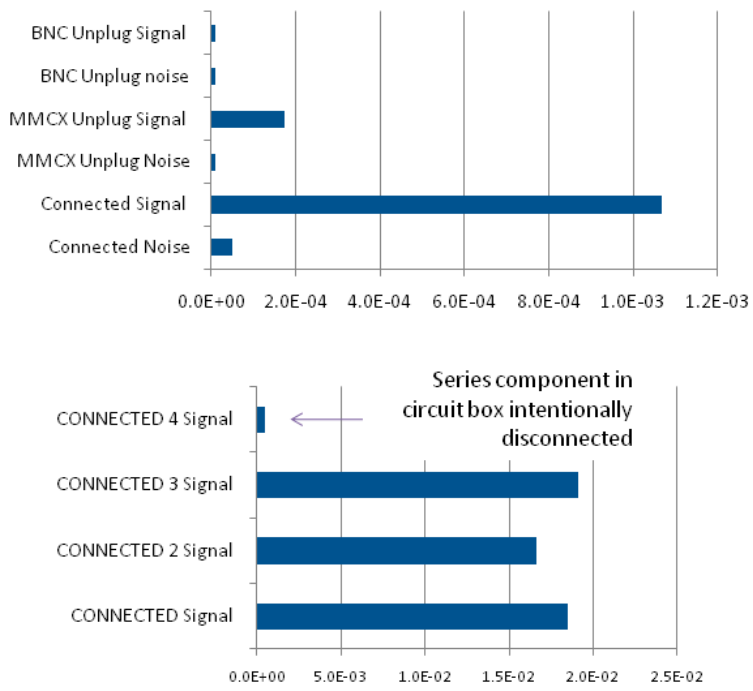

Figure 4.4.7. Device signal and noise measurements with varying connection states.

Varying scan parameters such as slice number did not significantly change the signal and noise measurements. The application of a saturation pulse resulted in a 50% reduction in measured signal but was still differentiable from the MMCX connection drop of over 90% of the previous signal value (Figure 4.4.8). Since the signal measurements come from the 2 degree pulse, the dynamic changes in flip angle and pulse width did not have a considerable effect. Subsequently, the fraction of current signal to prior signal selected as a cut-off was at least 1/3 to avoid falsely engaging the “fail-safe” with the use of imaging features like saturation pulses.

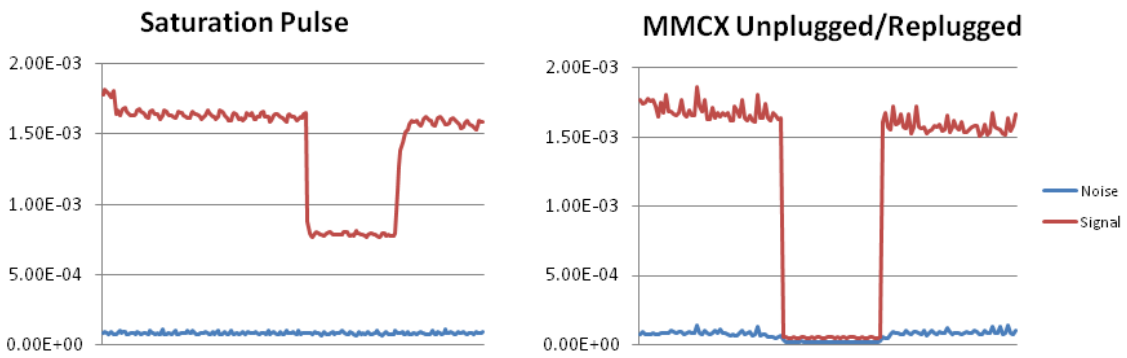

Figure 4.4.8. Signal and noise levels comparing saturation pulse application and sudden device connection.

The monitoring system quickly identified and triggered the scanner to a low power state before the next slice when device signal was suddenly lost, unacceptable temperature increases (absolute or rate) occurred, or any of the monitoring components were lost. Device heating was limited successfully by controlling the acceptable temperature increase rate and scaling the scan parameters accordingly. This is displayed in the temperature plots in Figure 4.4.9 where the same device was tested with and without the monitoring system active and the heating controlled by varying the pulse width up to 3 times the base value (changes reflected in temperature fluctuations). Minimal reductions in flip angle were then used if additional power drop was necessary to maintain the desired increase rate.

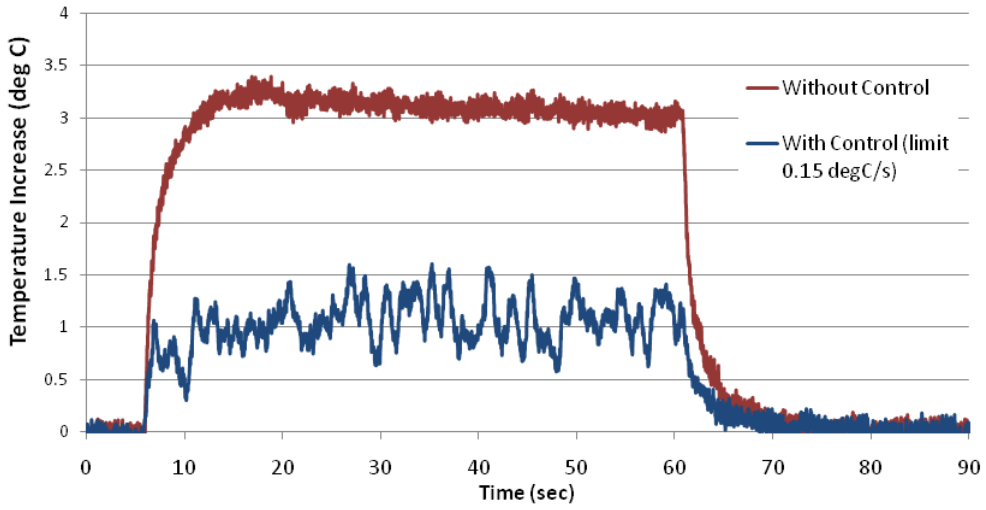

Figure 4.4.9. Device heating limited by controlling the acceptable temperature increase rate and varying PW and FA accordingly.

Unacceptable device heating also was controlled by slowly increasing the power until a fixed absolute temperature increase was reached. First the pulse width factor was dropped by a half-fraction from 5 to 3 and then the flip angle factor was brought towards 1 before the pulse width would decrease all the way to 1. The parameters changed according to a user-selected input of every 3 slice acquisitions. The difference in heating with the limited power is shown in Figure 4.4.10 with an extreme example of wire heating and the corresponding FA and PW plotted with the temperature increase.

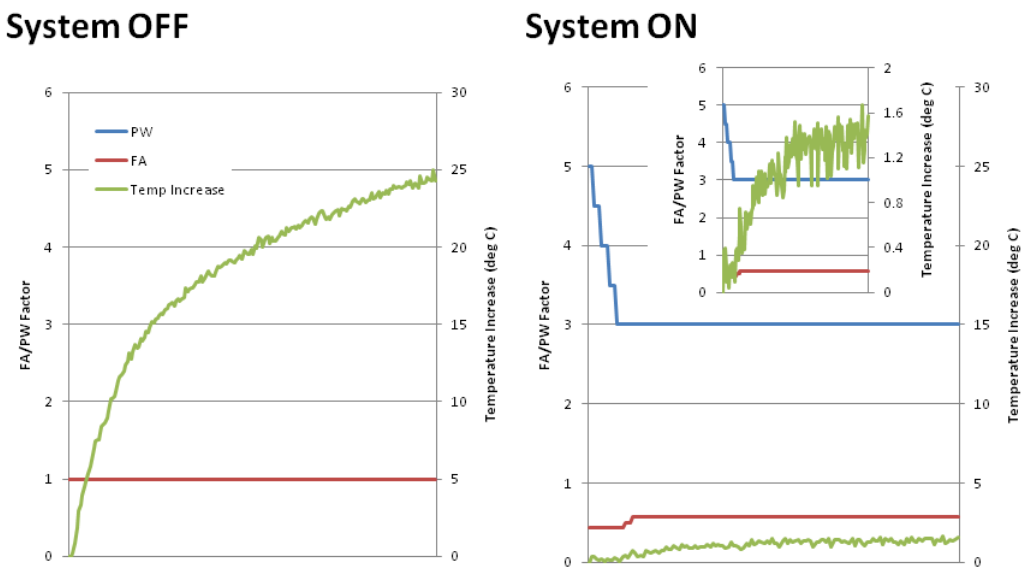

Figure 4.4.10. Example of system with progressively decreasing power until an absolute temperature limit was reached.

4.4.3 Discussion

With this system, we were able to monitor several aspects of proper device operation (signal, temperature changes) and dynamically alter scan parameters of flip angle and pulse width accordingly to adjust deposited power. Different parameter optimization strategies could be used to determine the appropriate operating conditions and ensure safe device use without having to immediately stop scanning which may be detrimental in the middle of a procedure. Ultimately this type of system also could be designed and incorporated into a program with just external temperature or other monitoring inputs which would run on the scanner host and avoid communication with another machine.

To maintain temperature increases such as below 2 degrees in a short time period by limiting the increase requires an increase rate of less than 0.2 degree Celsius

per second. Given the temperature sensor and signal conditioner accuracy of 0.3 degrees, this may not be the preferred method or a larger time scale of change needs to be considered. Considering this is a safety backup system that should only be engaged if necessary, we found that increasing the power slowly and ensuring that an absolute temperature level wasn't exceeded during the power ramp up likely a better approach. This approach may also be preferable during initial clinical testing where the device can be moved to different locations, including those that might be considered higher-risk for heating, and then scanning started with the gradual increase in power to assure that normal scan parameters are appropriate. The system was set-up to still respond to acute changes once the absolute threshold was achieved but the fluctuations while the device had acceptable absolute temperature readings would cause constant fluctuations in pulse width and flip angle values. Since the temperature data was acquired at a much higher rate than slice acquisition, we were also able to look at several temperature measurements and monitor the trends to limit the influence of the small point to point fluctuations. Determining a baseline *in vivo* may also be challenging with the device continually moving and if there are fluctuations in the local internal temperatures measured so a maximum temperature cut-off is likely preferred.

The signal measurements could drop naturally as the device is removed from the body or in areas where signal source is low. This is unlikely in a normal vascular intervention where the device is in the blood pool but could arise in other procedures. Removing the guidewire causes a slow reduction in signal (Figure 4.4.11) as opposed to a sudden drop if something is disconnected which was also factored into our response limit but be more difficult to differentiate when device signal received is already low.

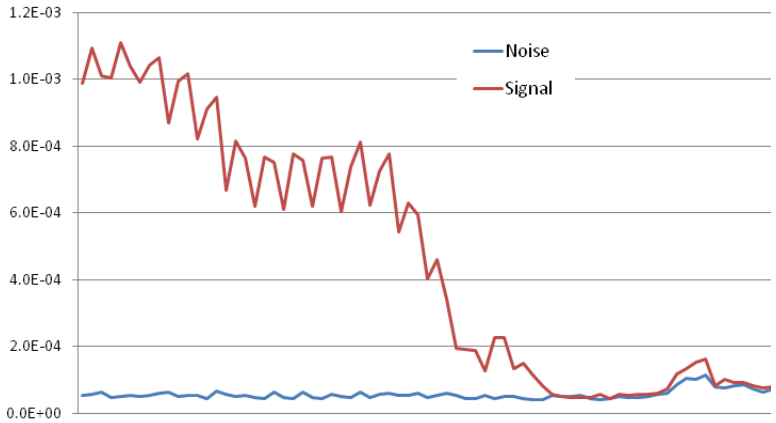

Figure 4.4.11. Signal and noise levels recorded as guidewire was pulled-back from the aorta and out the femoral access sheath.

In place of these signal and noise measurements at each slice, an alternate mechanism to determine device connection could also be used. A sensor could be incorporated in the circuit box to provide a visual cue to the operator that a power measurement is no longer detected and then that input provided to the scanner or system through an additional input. Similar to how surface coils are monitored, monitoring the current and response of the PIN diode in the detuning circuitry could also be performed.

We also conducted real-time imaging to ensure that scanning at the varying flip angle and pulse width parameters listed would be reasonable to guide procedures if a reduction in power is necessary. Three-fold increases in pulse width could permit anatomic and device visualization for procedural guidance with minimal increase in motion and flow artifacts (Figure 4.4.12).

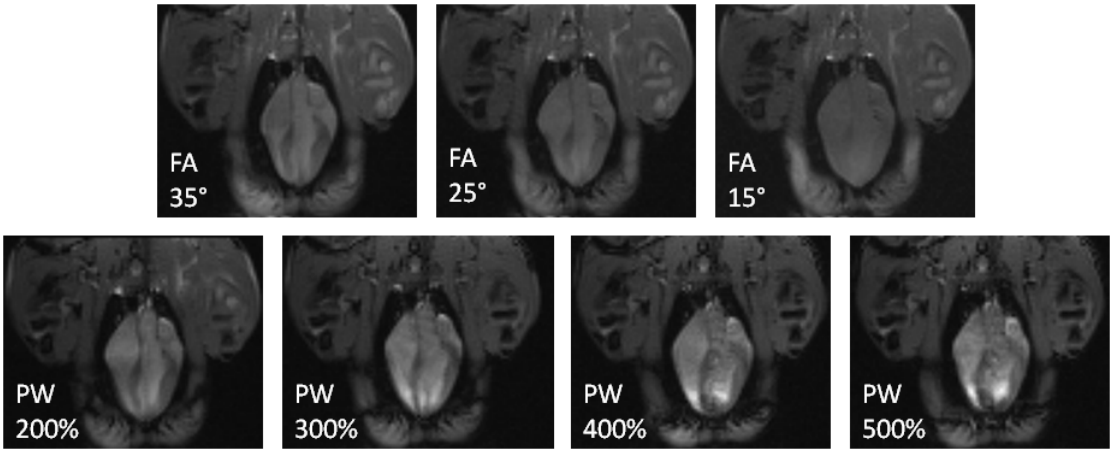

Figure 4.4.12. Sample cardiac images at varying flip angle and pulse width.

These become more pronounced with the longer TRs but image guidance is still sufficient to determine device position or physiological situation before pausing scanning to address the issue. With decreasing flip angle, contrast between the myocardium and blood pool decreases and is likely not sufficient below 20 degrees. Alternatively, other lower power sequences like GRE could be used to enable imaging at further decreased power limits than may be possible with SSFP.

While we have demonstrated the performance of this system with temperature monitoring, this system could also readily incorporate other potential inputs to monitor and control operating parameters as new measures of device safety are developed (142-145). Our group has started to examine the possibility of device-based RF power measurements. One of the methods to measure RF power is a thermal sensor where the incoming power is absorbed by a “dummy” load, typically a resistor, and the heat produced by the load is proportional to the power dissipated, regardless of frequency. We employed a 50 ohm resistor in series with the circuitry with a temperature sensor on the resistor to measure heat dissipation. Resistor heating followed the same heating

curves seen with the device temperature curves and increased with increasing scan power by varying flip angle. For varying device heating with altering device position, the resistor measures did not necessarily correlate with the device tip heating. In an instance where the tip heating decreased suddenly, the resistor heating actually increased (Figure 4.4.13). This could indicative of an impedance of the surrounding and the current is preferentially dissipated at the resistor rather than the guidewire tip or a shift occurs where the majority of current is on the externalized portion of the guidewire and dissipated at the resistor and insertion point rather than at the tip of the device.

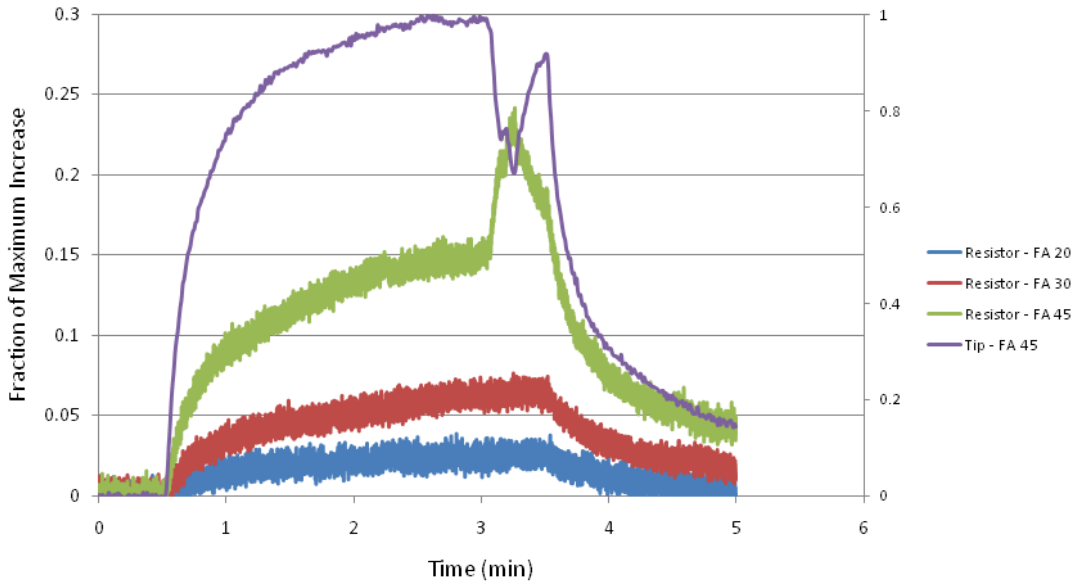

Figure 4.4.13. Resistor heating at various flips and corresponding tip heating at 45 degrees with sudden change reflected in both measures.

Imaging based device safety monitoring methods may also be possible. Reverse polarization imaging could provide an indication of device coupling that could result in an

unsafe condition (146). At minimum, some comparison between the forward and reverse polarized image would be necessary to indicate a loss of signal or change in device condition because the linear dipole or other coil designs normally can produce a linearly polarized field. MR thermometry is another available technique but the limitations discussed earlier make this challenging and unlikely for accurate real-time measurements with current techniques. Alternatively, the device could potentially be used to receive the signal immediately near the device for potential measurements with a limited field of view and rapid acquisitions.

4.5 Chapter Summary and Contributions

This chapter began with an evaluation of the important parameters in evaluating active MRI device safety which helped inform the development of improved methods to characterize the device heating profiles and provide a means for continual temperature monitoring. Inner and outer temperature measurements were compared and the utility of internal temperature measurements seen with in vivo temperature monitoring during simulated left and right heart catheterization. These components were then integrated into a system that was developed to monitor device status and dynamically alter scan parameters to enable a procedure to continue uninterrupted. Together these contributions help elucidate the key components to consider for RF device safety, provide an indication of heating observed in large animals with improved monitoring, and an additional backup control system for initial human clinical trials.

CHAPTER

5

MRI GUIDED CARDIOVASCULAR ACCESS

5.1 Introduction

Catheter access to blood vessels is necessary prior to any endovascular procedure. Initially this required surgical exposure and repair, but now typically is accomplished using direct palpation or anatomic landmarks. In difficult cases, such as patients with peripheral vascular atherosclerosis and obesity, adjunctive image guidance with X-ray fluoroscopy or ultrasound can be helpful. Standby X-ray is used frequently to confirm guidewire position before placing large introducer sheaths, especially when tactile feedback suggests an irregularity. Complications can arise from this seemingly simple procedure including vascular injury or mural disruption, hematoma, pseudoaneurysm. arteriovenous fistula, or life-threatening hemorrhage (147). Percutaneous vascular access can also be difficult in research animals such as swine with small or impalpable vessels requiring surgical exposure at some facilities.

The superior soft tissue visualization and multi-planar viewing capabilities of MRI is appealing to guide endovascular and minimally-invasive interventions. We are developing real-time MRI guidance for transcatheter procedures (148). Direct percutaneous vascular access inside the interventional MRI system would be an attractive alternative to access in the X-ray system followed by transfer to the MRI

system. MRI-guided vessel access could exploit the inherent vessel contrast and greater anatomic context of the vessel and its path.

The soft-tissue contrast of MRI could also allow operators to secure alternate access to the heart which may be required in certain cardiovascular diseases or procedures where traditional vascular access is insufficient. Percutaneous direct cardiac access through the chest wall can provide direct targeting for cardiac structures which may otherwise be extremely difficult to reach endovascularly due to their location and orientation, to a patient's aortic or other vascular disease, or device size or positioning constraints. Image guidance for such a procedure could allow targeting of the proper entry site and trajectory to avoid critical structures in the entry path with close monitoring of the procedure and cardiac structure and function.

In this work, we examined MRI guidance for three different type of cardiovascular access: (1) jugular vein; (2) transabdominal access of the hepatic and portal veins; and (3) transthoracic direct cardiac access, with pre-clinical demonstrations in swine. Animal experiment protocols were approved by the institutional animal care and use committee, according to contemporary NIH guidelines.

5.2 Jugular Access

In a porcine model of difficult vascular access, we tested the feasibility of MRI with narrow field of view to guide needle access to blood vessels. We hypothesized that real-time MRI needle and guidewire access to the jugular vein is feasible using reduced field-of-view techniques and active profiling needle devices. We compared a custom “active” profiling needle with commercial “passive” MRI-compatible needles in procedure time and number of passes. We also hypothesized that enhanced imaging guidance would enable novice operators to achieve access with proficiency similar to that of more experienced operators.

5.2.1 Methods

Vascular Access In vivo

The active needle was evaluated *in vivo* during real-time MRI-guided jugular vein access in swine. Animal experiment protocols were approved by the institutional animal care and use committee, according to contemporary NIH guidelines. Yorkshire farm pigs (mean 36.3 kg ± 7.8 kg) underwent mechanical ventilation with inhaled isoflurane.

Operators

We tested the ability of MRI to allow inexperienced operators to perform difficult vascular access by comparing novice (medical student), intermediate (fellow), and experienced (attending interventional cardiology) operators.

Jugular Vein Access

Jugular vein access in swine was selected as a model of difficult vascular access because pulses are typically not palpable, anatomic and radiographic landmarks are limited, and the veins readily spasm when irritated and collapse under superficial pressure (149). A total of 30 vessel access procedures were attempted (average vessel size 0.81 ± 0.09 cm), 17 with the active needle (average vessel size of passive needle attempts 0.80 ± 0.09 cm) and 13 with the passive needle (0.81 ± 0.10 cm). Most access attempts were to the external jugular vein, except in the larger animals where the internal was accessed to have similarly sized targets, since unlike humans, the external is larger and more superficial than the internal jugular (~0.4cm in diameter for the pigs used) and often used for catheterization in many animals (150). When possible, bilateral access was attempted in the same animal by a given operator for comparison of active and passive needle use as described later in this section.

To identify the vessel target and plan the desired trajectory and entry location, three orthogonal stacks of free-breathing, non-gated T2-weighted SSFP scout images were acquired of the neck region. From these images, an entry site was selected where a straight vessel segment was clearly visualized that was suitable for vascular access and that had limited tortuosity and bifurcations. A sample scout image for vessel identification and slice positioning is shown with the real-time 3D slice rendering in Figure 5.2.1.

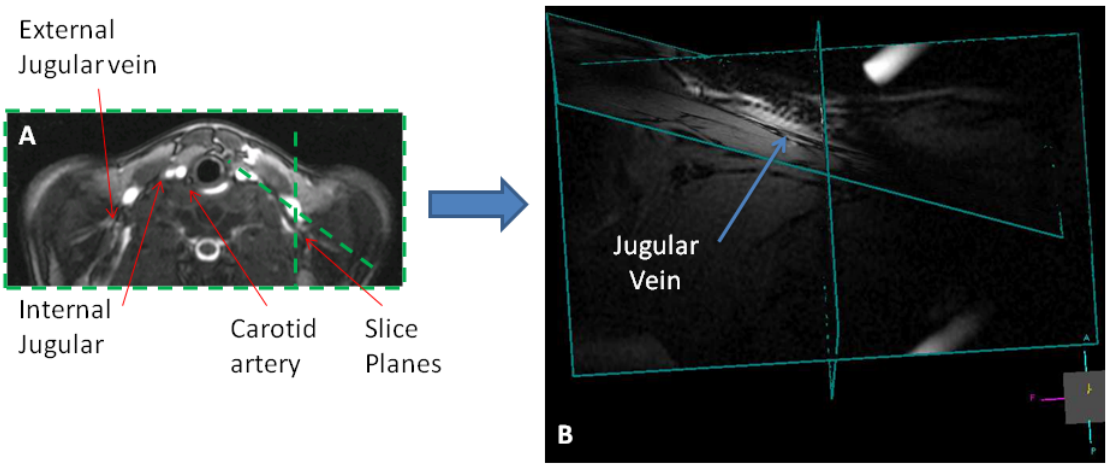

Figure 5.2.1. Procedure workflow. Scout images (A) used to identify vessel entry sites and then place real-time slices (B) with water-filled syringe identifying trajectory.

For better visualization of the vessel during the access procedure, the field of view was reduced without aliasing using a small 7 cm diameter loop coil (Siemens Medical, Erlangen, Germany). The coil was placed in a sterile bag and positioned by the operator just caudal to the desired access site. This allowed the field of view to be reduced to 229 x 135 mm without aliasing while maintaining the same matrix size, increasing the in-plane resolution to 1.2 x 0.94 mm and providing good signal with the close proximity of the coil to the relatively superficial target vessel (Figure 5.2.2).

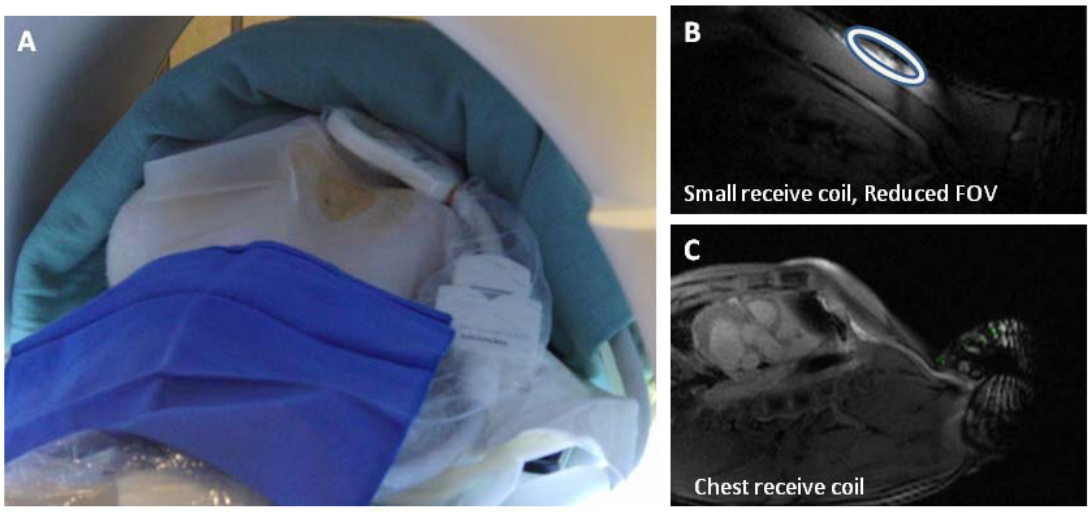

Figure 5.2.2. Access set-up and imaging. (A) Photo of neck access site, prepped with small loop coil in sterile bag. Examples of imaging with (B) and without (C) small loop coil and reduced field of view.

Two constantly updating perpendicular long-axis slices along the vessel were used in the sagittal and coronal directions to provide cranial-caudal, anterior-posterior, and right-left positioning of the needle relative to the target vessel. A third short axis slice perpendicular to the vessel was also used occasionally for positioning and to confirm vessel entry by the needle. The operator then used an MR visible pointer (finger, Gadolinium or water filled syringe, or active needle) at the animal's neck area to locate the desired entry point and needle trajectory. The scan positioning and targeting was adjusted during the procedure if necessary by an operator in the control room.

For the active needle, a device-only projection mode with non-slice selective imaging of the device channel only available in the real-time reconstruction system was used (6). This assisted initial trajectory planning to align the needle to the imaging slice

(Figure 5.2.3) and to identify efficiently the location and trajectory of the active needle if it was out of plane.

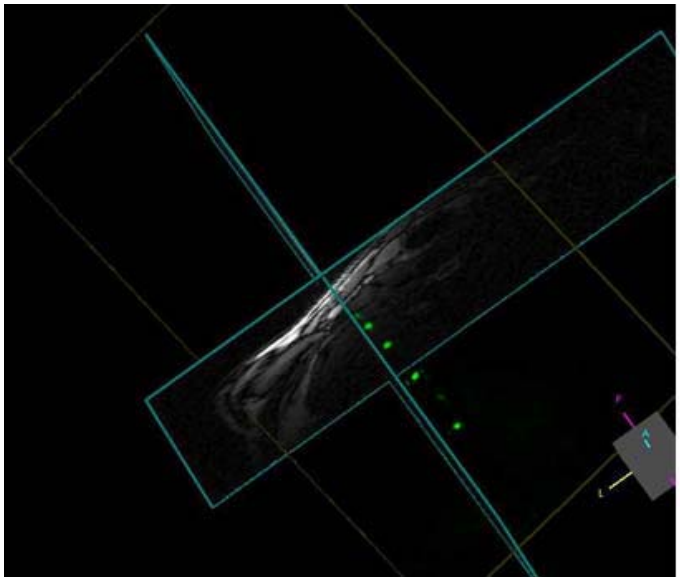

Figure 5.2.3. Device-only projection mode enables visualization of entire needle length to help align trajectory to imaging plane.

Previously-acquired time-resolved magnetic resonance angiograms were also available to assist in slice positioning and serve as a roadmap in the 3-D rendering in the real-time display (6) . Vessel entry was confirmed by imaging, by gadolinium 1% angiography, and by successful insertion of a guidewire into the lumen down towards the right heart. Finally, the needle was exchanged for a standard introducer sheath, securing access to the vessel.

Active and Passive Needle Comparison

Access was attempted bilaterally on a total of 12 animals with either the active needle design or the unmodified passively visualized needle, for a total of 24 access attempts. The planning and imaging approach described above was the same for the active and passive needle attempts, other than only the active needle being visible at skin entry. To minimize the influence of which needle (active, passive) or side (right, left) the operator started with, operators alternated both the type of device and the side that access was attempted initially.

Endpoints and Statistical Analysis

Needle puncture of the vessel with blood return and advancement of a guidewire for sheath exchange within 15 minutes of skin entry was defined as a *successful vascular access attempt*. Success rates, procedure time and number of passes needed to access the vessel were compared between attempts with the active and passive needles. *Procedure time* was considered from first skin puncture to successful placement of a wire into the vessel. A *needle pass* was defined by an attempted vessel puncture. The time-based success measures were not normally distributed, particularly given procedure failure. Therefore we used non-parametric, unpaired statistical tests (Fisher's Exact Rank for Success Rates and Mann-Whitney U for time and passes) to compare the procedure outcome measures for the active and passive needle attempts. Parameters are reported as mean ± one standard deviation with two-tailed P values reported and < 0.05 considered significant. We did not correct for multiple comparisons.

5.2.2 Results

Real-time MR imaging enabled careful selection of the skin and vessel target site and visualization of the vascular access and guidewire placement. Use of a small receive coil at the surface helped maintain the sterile field and allowed reduced field of view imaging without wrap-around artifacts for better visualization of the target vessel during the procedure. Representative procedure images with the skin trajectory and needle access with the active needle are shown in Figure 5.2.4.

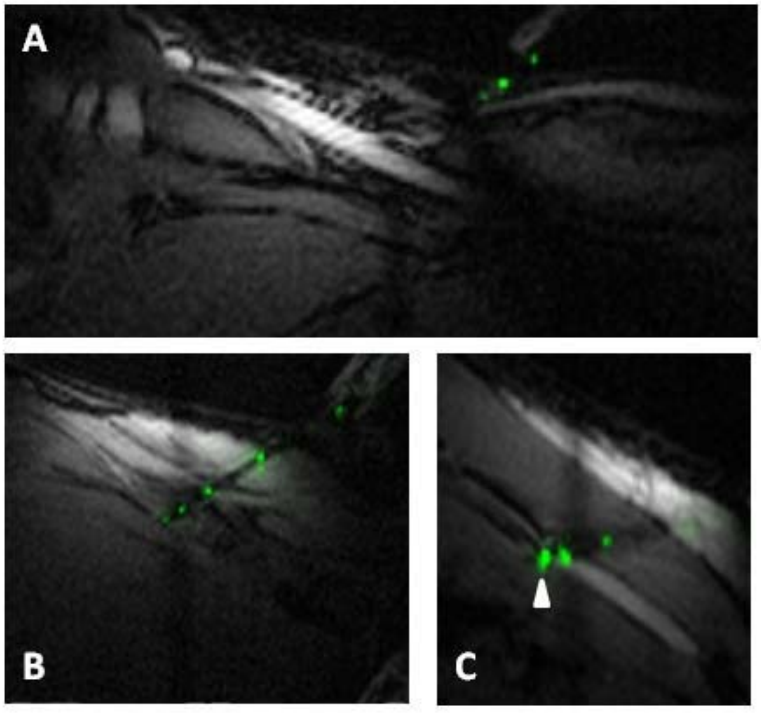

Figure 5.2.4. Active Needle in vivo. (A) Planning trajectory with needle on skin surface. (B) Entire needle length and tip location clearly visible. (C) Distal 2 markers seen in vessel.

The needle device performed as expected, allowing blood return, gadolinium angiography, and wire passage through the 0.035”-guidewire-compatible central lumen. Increase in coil signal was also apparent when the vessel was entered, corresponding to the increase in available signal source.

Operators were marginally more successful in achieving jugular vein access within the allocated 15 minutes using the actively visualized needle than the passive needle. Successful attempts using the active needle were shorter and with fewer needle passes than those using a passive needle. For all access attempts, 12 of 17 (71%) active attempts vs. 8 of 13 (62%) passive attempts were successful, p=0.71. The results for the subset of 12 animals with bilateral access attempted systematically in each animal are shown in Figure 5.2.5 where access was achieved in 10 out of 12 animals (83%) with the active approach and 7 of 12 (58%) for the passive, p=0.37. Among successful procedures, average time-to-access was shorter using the active needle (88 vs. 244 sec, p=0.022), and required fewer needle passes (4.5 vs. 9.1, p=0.028). Including all access attempts, and censoring failure attempts as time to access of = 900 sec and number of passes = 15 since rank-based statistics were used, the differences between active and passive approaches for number of passes (p = 0.019) and time to access (p=0.016) remained significant.

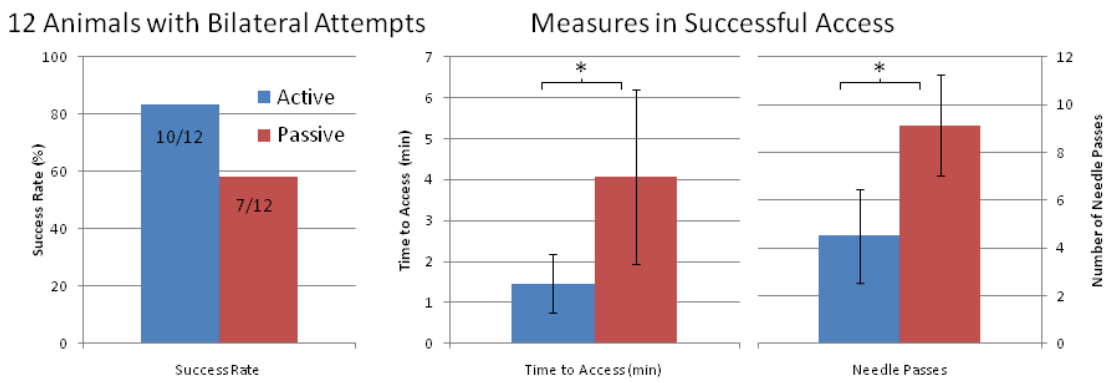

Figure 5.2.5. Access results in 12 animals with bilateral attempts comparing active and passive needles in success rate, time to access, and number of needle passes.

Operator experience did not have a clear impact on the success or duration of the access procedures although operator subsets were small (Figure 5.2.5). Results were more variable with the passive needle attempts than active needle ones. In the animals with bilateral attempts, intermediate and advanced operators were successful on all active attempts while the two failures by the novice occurred (1) in the first procedure and then (2) during a later attempt when wire placement was unsuccessful after vessel access (bleedback). Time to access and number of passes in the successful procedures with the active needle also did not correlate with experience and were similar between groups. For passive needle access, the novice operator was more successful and quicker than the intermediate and advanced operators which were more variable. Expert operators provided a subjective report that the MRI-compatible needles were less sharp, longer, and prone to bending compared with conventional steel x-ray access needles.

Table 5.2.1. Access results comparing novice, intermediate, and experienced operators for success rates, average time to access and needle passes with active and passive needle use.

		ACTIVE NEEDLE			PASSIVE NEEDLE		
	n	Success Rate (%)	Passes	Time (sec)	Success Rate (%)	Passes	Time (sec)
Novice	5	60	4.3 ± 1.5	99.0 ± 31.3	80	7.8 ± 3.2	228.3 ± 112.4
Intermediate	3	100	4.0 ± 2.6	94.3 ± 60.1	33	13.0	424.0
Advanced	4	100	4.8 ± 2.6	105.8 ± 54.1	50	13.5 ± 0.70	354.5 ± 98.3

5.2.3 Discussion

MRI-guided vascular access was accomplished with both actively and passively visualized MRI-compatible needles. When actively or passively visualized needles are perfectly aligned with the imaging plane (Figure 5.2.6) the tip position is evident. However, in our experience with a slightly longer (15 cm) and more flexible needle, this was not always the case and accounted for much of the extra time spent during the passive needle attempts. Several algorithms to better track passively visualized devices including needles are under development (151) which may assist the procedure.

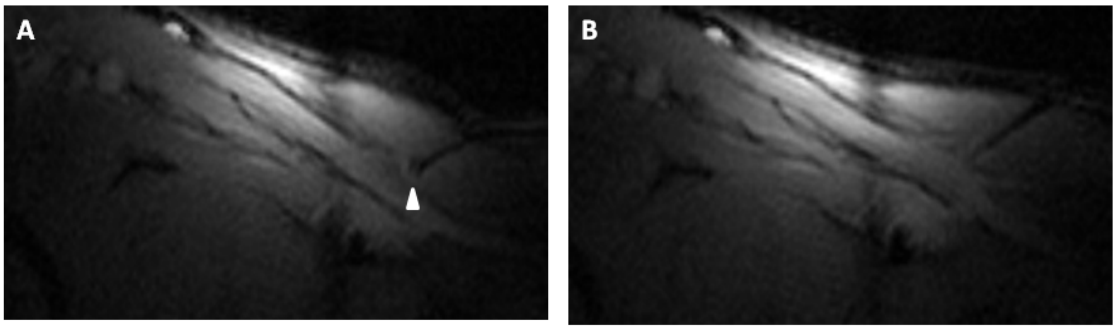

Figure 5.2.6. Passive Needle in vivo. Exact tip location is visible when aligned in plane (A) but difficult to locate if part of the needle is out of plane (B).

MR imaging provided greater information to the operator about desirable vessel entry site and multi-planar views of the vessel and needle position typically unavailable with other imaging modalities. This enhanced imaging may have assisted operators with little to no experience to successfully achieve vascular access by providing a greater anatomic context and proper needle positioning and approach to the vessel. In our experience, the operator's technique had the biggest impact on successful outcomes, particularly with the passive needle. Maintaining a good long-axis imaging slice of the target vessel and aligning the needle accordingly along that trajectory greatly simplified the procedure. This approach required minimal movement of the imaging slices and time spent searching for the needle location. It also helped ensure that the operator did not take an oblique angle to the vessel that may cause later difficulty in passing a guidewire or sheath.

Use of the active needle and device only projection mode facilitated aligning the needle to the appropriate slice and trajectory before skin entry as described in the methods. We also pursued the use of a needle guide and MRI-compatible device holder to help the operator identify and maintain the device positioning. A photo of the arm and

holder set-up is seen in Figure 5.2.7 with accompanying MR imaging. This helped align the needle to the long-axis slice along the vessel and water-filled needle guide was apparent on MR imaging which could be used with either the active or passive needles. Without finer manipulation of the holder at the distal end, it was slightly more challenging to change the angulation of the needle as necessary during the procedure for vessel entry and subsequent wire exchange.

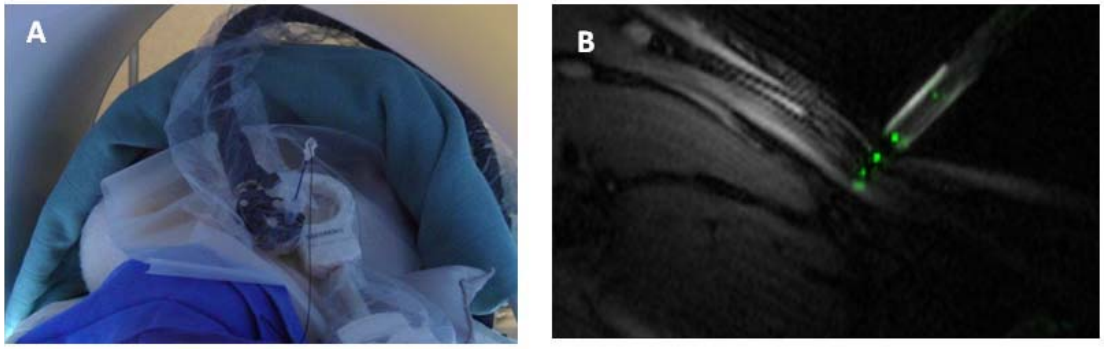

Figure 5.2.7. Device holder and needle guide. Photo of set-up in (A) with needle guide appearance with active needle seen on real-time MR imaging in (B).

The minimal difference between novice and more experienced operators in achieving access, particularly with the passive needle, also may be attributed to those less familiar with access and other adjunct imaging being more likely to follow the imaging planes and technique described above to orient the needle trajectory in long-axis rather than approaches used with other imaging like ultrasound.

MRI also offers other potential enhancements that might simplify complex procedures, monitor complications and confirm procedure success. Previously acquired MR angiograms may provide enhanced roadmaps combined with real-time imaging slices in the 3D-visualization window (Figure 5.2.8).

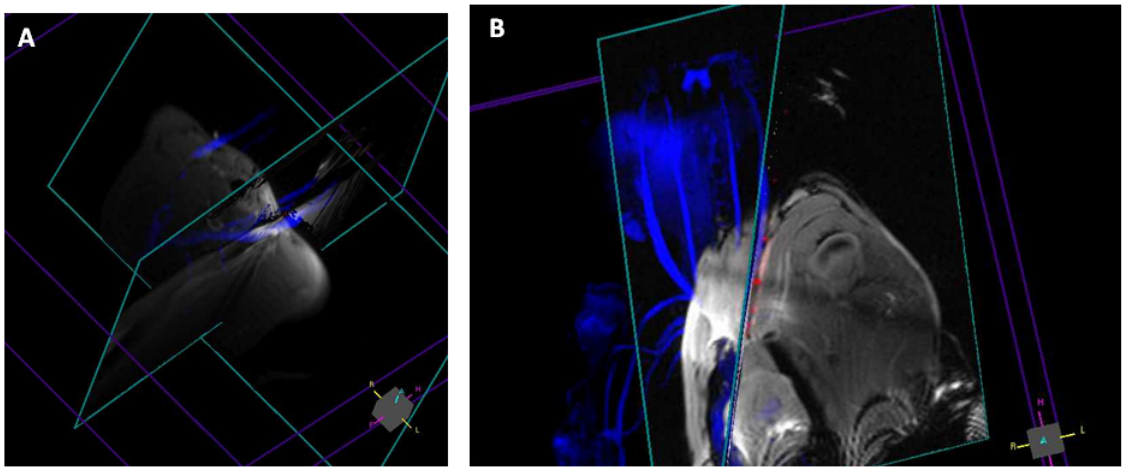

Figure 5.2.8. MR angiograms of neck vasculature displayed as dynamic MIP in real-time system 3D display.

Fluid accumulation or extravascular hematomas can be quickly recognized and treated without delay typical of X-ray workflows to administer exogenous contrast. Avoiding inadvertent needle entry to bystander structures could potentially reduce complications. In our experience, we observed one intraprocedure hematoma formation after unsuccessful needle passage but no inadvertent carotid punctures. Selective gadolinium injections after imaging saturation permit additional confirmation of vessel entry.

Procedural performance could be improved with superior vessel and device visualization. In addition to the material considerations mentioned, tip location and

targeting accuracy are limited during the procedure by the distance between the start of the coil and the true needle end necessitated by the long bevel. Visualization of the signal can appear larger than the needle size which may make targeting small vessels for access more challenging. Tracking may assist in the localization but millimeter-scale errors are still possible and the coil is not located exactly at the end of the needle tip. Signal can also be lacking in low signal tissues where an internal signal source may be necessary. As with any active device in the MR environment, RF safety and heating must be considered. Detuning during RF transmission and cable traps are already used to reduce the coupling to the high-power RF B1 deposition. Further design modifications could also be employed to reduce the heating risk in these short needle type devices.

In addition to a more defined device appearance, improvement of the real-time vessel imaging would further facilitate this procedure. We improved the small vessel imaging in real-time using a small local receive coil to permit a reduced field of view but spatial and temporal resolution closer to that of ultrasound would make the MRI-guided approach more comparable, particularly for smaller vessels. Alternate non-cartesian trajectories like radial or spiral may allow increased temporal resolution to observe vessel deformation and then greater spatial resolution could permit targeting of smaller vessels. The logistics of the MR environment are more complicated than alternate imaging techniques (ultrasound, X-ray) but the neck was relatively accessible and this would permit vascular access in a procedure already being performed in the interventional MRI environment.

5.3 Transhepatic Vascular Access

Transhepatic access can be used when typical venous access is not available or insufficient such as in small pediatric patients with venous occlusion for multiple procedures (152-154). Clinically, this is performed under X-ray with progressive needle advancement and contrast injection or with limited views under ultrasound guidance (155). This approach can also enable alternate approaches to procedures like TIPS where PIPS or percutaneous intrahepatic portosystemic shunts have been attempted in place of the transjugular approach with x-ray, ultrasound and electromagnetic tracking guidance (156-158). The easily visualization of vascular structures with MRI could allow a more targeted approach for these procedures avoiding contrast and x-ray exposure and clearly identifying and avoid nearby soft-tissue structures. We hypothesized that MRI guidance could facilitate percutaneous transhepatic access to the hepatic and portal veins.

5.3.1 Methods

MR Imaging and Active Devices

All imaging and interventions were performed in a short, wide bore Siemens Espree 1.5T MRI scanner (Siemens Medical Solutions, Erlangen, Germany) with surface body matrix receive coils (TIM) in addition to the independent active device channels. Access was achieved beneath the abdominal coil or through one of the coil openings Real-time balanced steady-state free precession (SSFP) imaging (TR = 3.67 ms, TE = 1.23ms, ST 6mm, FA 45°, matrix 192x144, FOV 340x255mm) with a separate real-time reconstruction and display system (6) was used.

Liver Imaging and Trajectory Planning

Accessible hepatic and portal vein branches were identified on MR imaging that could be reached from an anterior, sub-xyphoid approach in swine. Sample vessel imaging is seen in Figure 5.3.1.

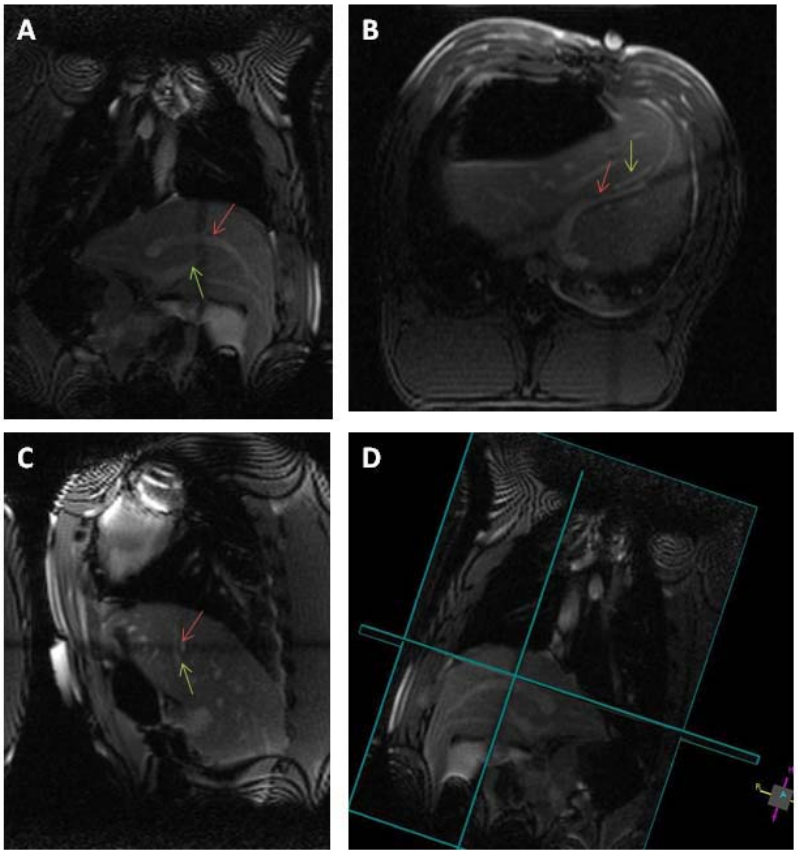

h

Figure 5.3.1. Target liver vessels seen in coronal (A), transverse (B), and sagittal (C) views displayed with relative 3D positioning in (D). Red arrow indicates hepatic vein branch and yellow arrow shows portal vein branch.

The active needle was used for access of the hepatic vessels. Trajectories were selected to avoid the rib cage, stomach, gall bladder and central portions of the portal vein which may be extrahepatic.

5.3.2 Results

The abdominal access point was selected to enter sub-xyphoid and avoid puncturing the stomach seen in black on the imaging. The needle positioning was then redirected after entry as necessary to reach the desired vessel. A small branch of the portal vein was successfully accessed with Gadolinium injection and wire placement for confirmation (Figure 5.3.2).

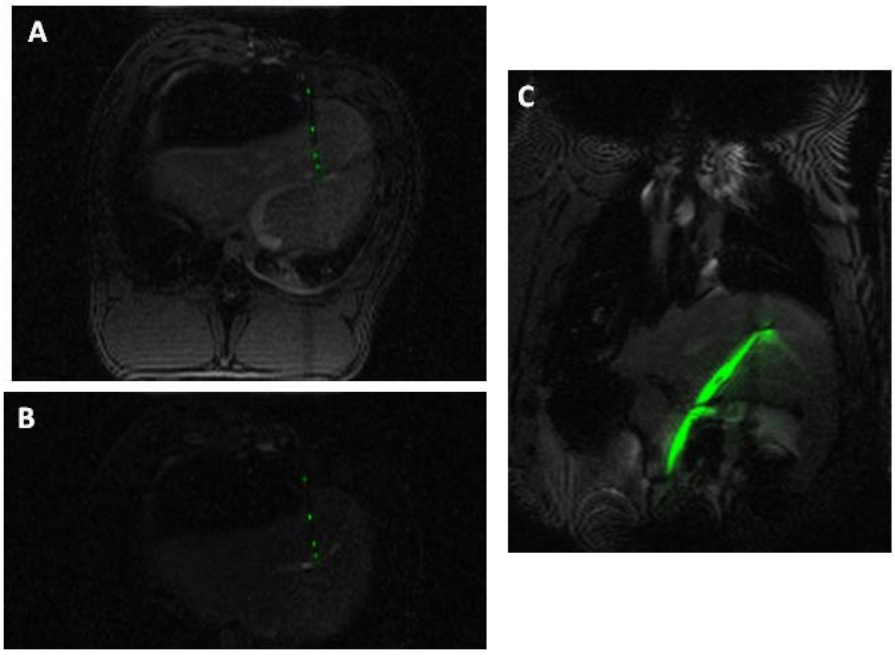

Figure 5.3.2. Success portal vein branch access. Needle entry position seen in (A) with subsequent Gd injection (B) and wire passage (C) for confirmation.

The active needle tip visualization provided valuable positioning assistance and clear indication of hepatic vein access. Figure 5.3.3 shows the approach to the hepatic vein where the tip of the needle traveled inferior of the vessel out of plane which was evident by the lack of the closely located distal marker points. This was corrected to readjust the path to successfully puncture the vessel.

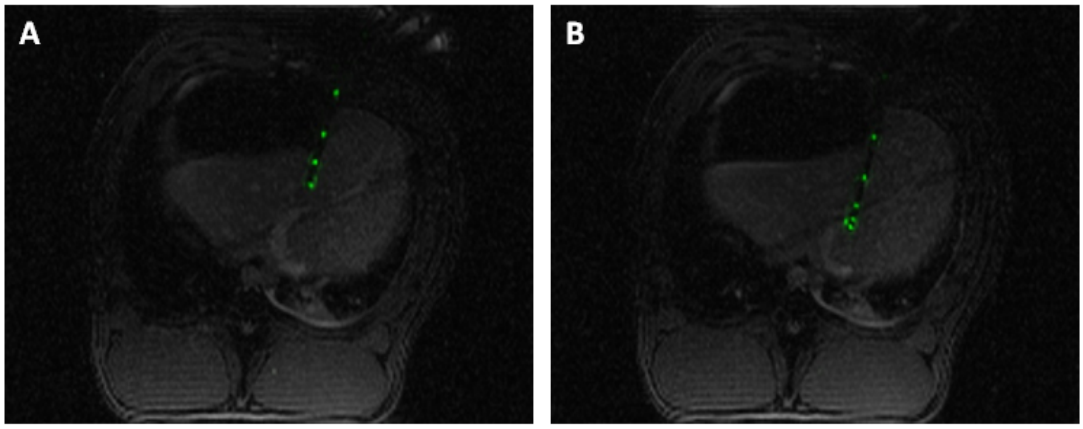

Figure 5.3.3. Active needle facilitating hepatic vein access. Needle tip was out of plane in (A) but positioning was corrected and vessel accessed in (B).

The presence of the distal marker points in the coronal view of the vessel provided confirmation of vessel entry in addition to Gd injection through the needle and wire passage into the IVC (Figure 5.3.4).

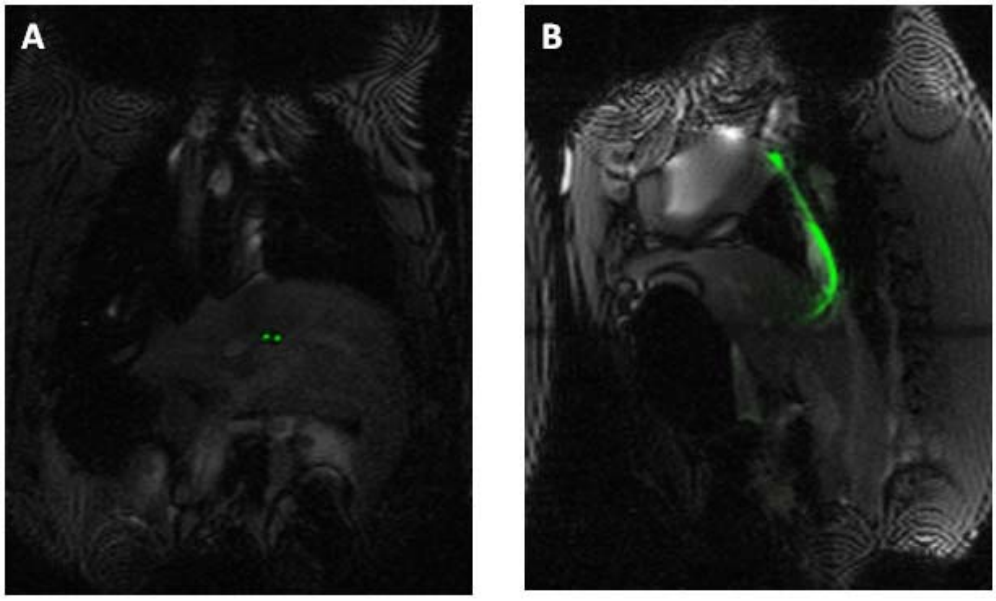

Figure 5.3.4. Confirmation of hepatic vein access. Distal markers are seen in coronal view of hepatic vein branch (A) and wire passage into IVC towards the right heart (B).

5.3.3 Discussion

In this part we were able to apply the capabilities of MRI and the approaches developed in jugular aspect of this work to enable more complex vascular access. MRI guidance provided clear imaging of the hepatic vasculature. This procedure as well as TIPS and other vascular liver interventions could benefit from additional MR angiograph roadmaps similar to those seen for jugular access. For these procedures, they can provide the locations of neighboring vascular and ductal structures that may be at risk during the procedure like the hepatic artery and bile duct. Figure 5.3.5 shows an example of the 3D rendered MIPS of the hepatic and portal veins and hepatic artery (159). Additionally, a magnetic resonance cholangiogram (MRCP) could be acquired and displayed as well to outline the ductal paths and gall bladder.

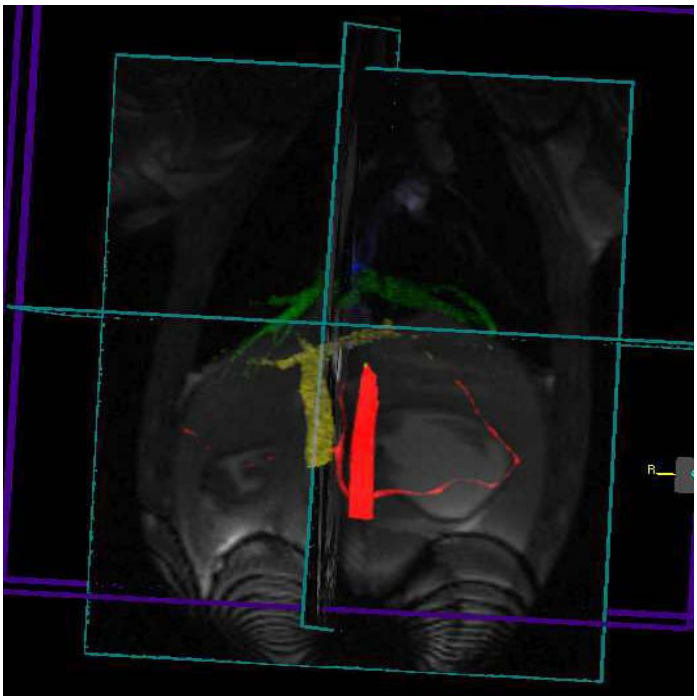

Figure 5.3.5. 3D Rendered MIPS of hepatic veins and artery with real-time slices for enhanced guidance.

The greater anatomic context enabled a targeted approach from the abdominal wall to the target vessel. Upon entry the rightward portion of the stomach was avoided and the needle could be clearly directed towards the target vessel. Access with a passive needle may have been possible with the contrast against the liver parenchyma but these were typically long trajectories and the needle could easily go out of plane as was demonstrated by the earlier figure with the active needle tip placement. Shorter trajectories may also be possible depending on the approach and usingthe initial MR imaging to evaluate target vessels and the paths to them.

5.4 Transthoracic Direct Cardiac Access

Percutaneous direct cardiac access through the chest wall can provide direct targeting for cardiac structures which may difficult to reach endovascularly. We hypothesized that image guidance provided by MRI for percutaneous cardiac access could allow targeting of the proper entry site and trajectory to avoid critical structures in the entry path with close procedural and functional cardiac monitoring. Using MRI guidance, we demonstrated a planned and monitored procedure to right and left ventricular puncture in swine using a closed chest transthoracic approach.

5.4.1 Methods

Animal experiment protocols were approved by the institutional animal care and use committee. Yorkshire farm pigs underwent mechanical ventilation with inhaled isoflurane.

MR Imaging and Active Devices

Body flex and spine array coils were used for receive and access was achieved beneath the chest coil or through one of the coil openings.

MR Angiogram (MRA) 3D Rendering

MRA was acquired with a breath-held 3D FLASH sequence with the following parameters: TR = 3.08 msec, TE = 1.02 msec, FA = 25°, FOV = 400 × 400 mm, and

voxel size =1.6 × 1.0 × 1.6 mm. Dicoms were exported to the real-time reconstruction system where they are dynamically rendered as a maximum intensity projection (MIP) in the 3D rendering window with the real-time imaging slices.

Black-blood Ventricular Septal Defect Roadmap

Roadmap displaying the ventricular septal defect target location was a dark-blood prepped 4-chamber turbo-spin echo (TSE) acquisition (TR = 700 msec, TE = 33 msec, FA = 180 degrees, ST = 5 mm, FOV = 340 mm x 276 mm, and Matrix = 256 x 154, Acceleration 2).

Myocardial Delayed Enhancement 3D Rendering

A stack of delayed enhancement images of the myocardium were acquired 10 minutes after Gadolinium administration with the following parameters: FOV 340x276, ST 8mm, TR 700 ms, TE 3.23 ms, FA 25 deg, TI 300 ms, matrix 255x192, BW 140 Hz/Px. The myocardium was manually segmented in Syngo software (Siemens) and display adjusted to show the enhanced areas. The images were then displayed in the 3D rendering window as a dynamic MIP as described previously for the MRA.

Direct Cardiac Access

Closed-chest perventricular cardiac access was attempted to the right and left ventricle using the actively visualized needle. In planning the trajectory, we employed both real time imaging views and previously acquired MR roadmaps and angiograms to

select an appropriate entry site and path to the desired target. An access trajectory and corresponding imaging planes were selected that would allow safe needle entry and avoid critical structures. An MR visible marker (syringe w/water or Gadolinium) or the active needle could be visualized externally to identify and align to the selected trajectory. Right ventricular access was performed through the right ventricular free wall through an intercostal space parasternally (Figure 5.4.1).

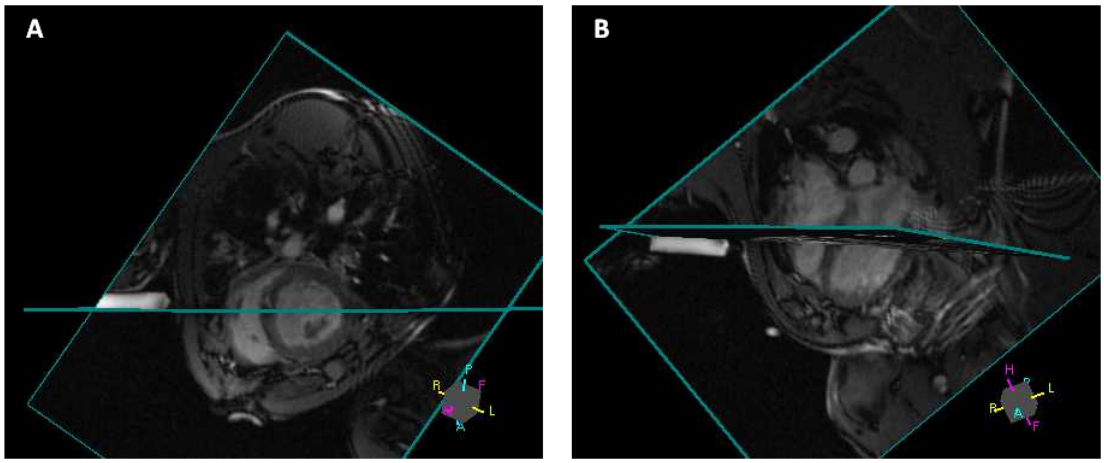

Figure 5.4.1. Right ventricle access trajectory in short-axis (A) and angled coronal (B) views.

Apical access to the left ventricle was attempted from a sub-xyphoid approach for targeting aortic and mitral valve structures (Figure 5.4.2). Depending on the orientation of the heart and placement of the apex, the chest wall could be entered from either the right or left sides of the xiphoid and angled accordingly.

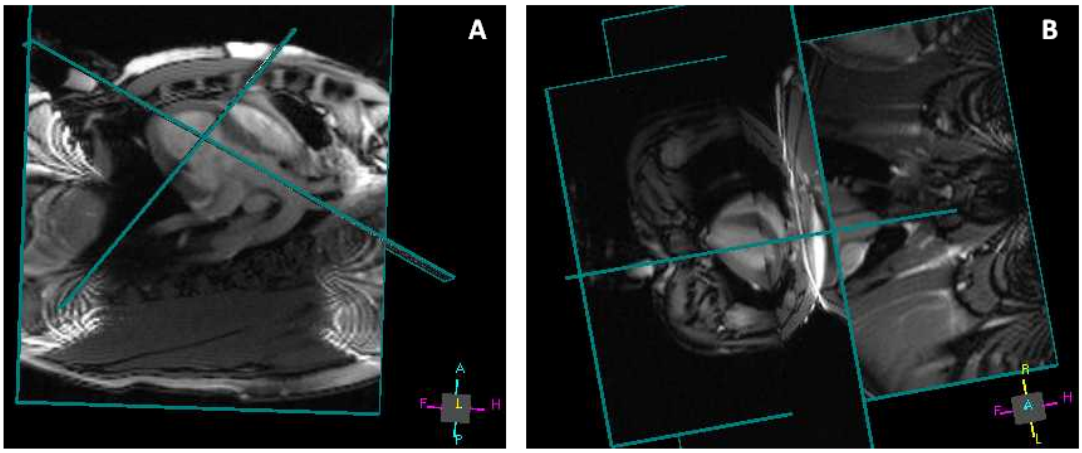

Figure 5.4.2. Left ventricle apical access trajectory in sagittal (A) and angled coronal (B) views.

The marker then was replaced with active needle to reconfirm the trajectory and prepare for access (Figure 5.4.3).

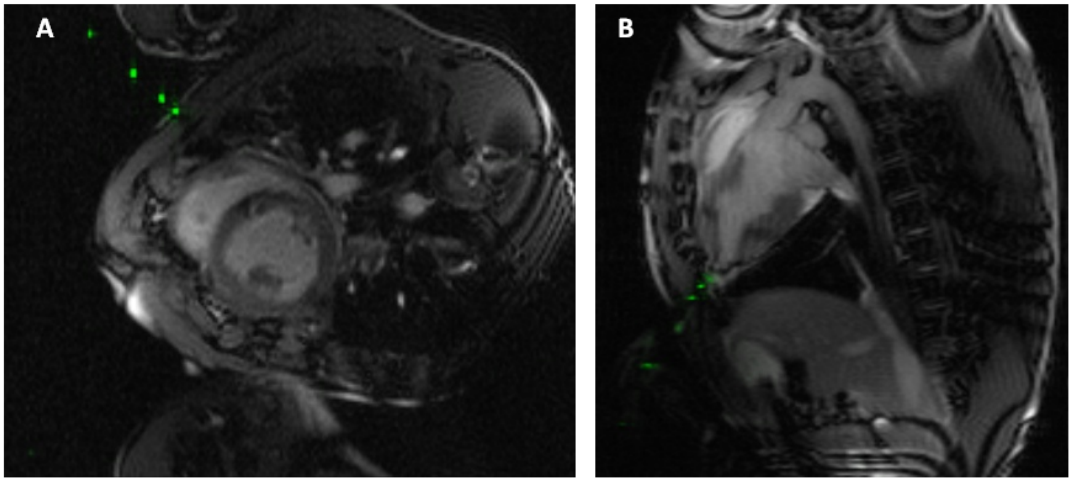

Figure 5.4.3. Active needle trajectory before entry to RV (A) and LV (B).

Slight adjustments to the trajectory were made if necessary due to limitations on rib space or xyphoid positioning. Two real-time imaging long-axis slices along the needle provided positioning during entry. A short-axis slice was used to monitor cardiac function and entry of the needle into the proper chamber. Cardiac access was confirmed visually on MR by needle location in the appropriate ventricle, with aspiration of blood through the needle and non-selective saturation followed by Gadolinium injection through the needle. After acute non-survival procedures and after follow-up for survival procedures, the explanted hearts were examined for damage to surrounding tissues during needle entry.

Pericardiocentesis

The fluid-filled pericardial space was approached with the active needle in a similar approach as the direct cardiac puncture and position was confirmed with gadolinium injection or guidewire placement. Fluid was then drained through the needle or replaced with a guidewire exchange for a pericardial drain.

5.4.2 Results

An initial needle trajectory was selected prior to skin puncture from an accessible entry location and adjusted as necessary during passage through the chest wall and into the heart based on the real-time imaging information.

To avoid damaging structures such as the internal thoracic (mammary) arteries while entering the chest wall, they were displayed as MRA MIP in the 3D display window with the real-time slices. Right-left positioning was adjusted to prevent possible puncture

which was typically lateral to the RIMA for RV access and medial to both vessels in LV access (Figure 5.4.4).

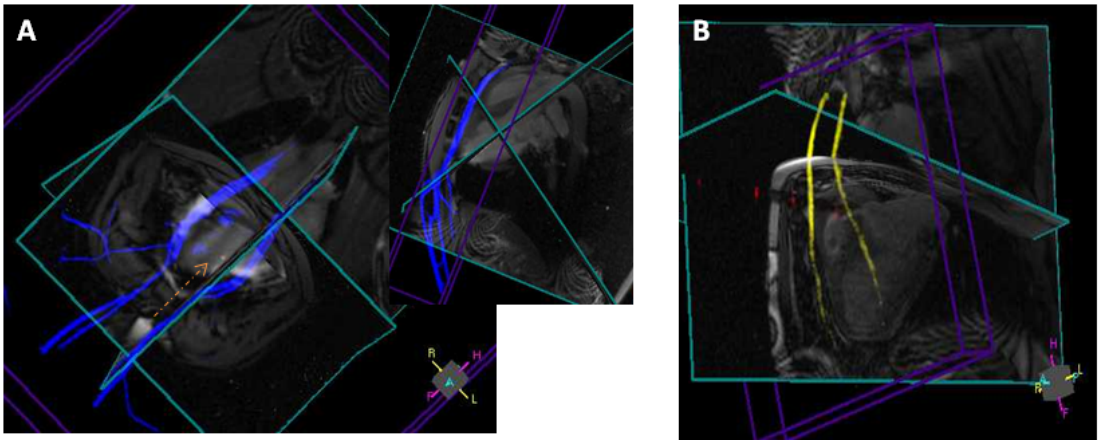

Figure 5.4.4. Internal thoracic artery MRA displayed in 3D rendering with slice positioning for LV (A) and RV (B) access.

For right ventricle puncture, the entry level was selected based on real-time imaging planes and available intercostal entry space to stay below the atrioventricular valve plane and minimize lung traversal. Imaging also helped to confirm that the angle of the needle and tip maintained a trajectory towards the apex of the heart rather than angled up towards the tricuspid valve. Figure 5.4.5 shows an example of right ventricle puncture with the active needle and the multiple views along the needle trajectory available to the operator. We monitored access in two views as can be seen to allow positioning manipulation if needed.

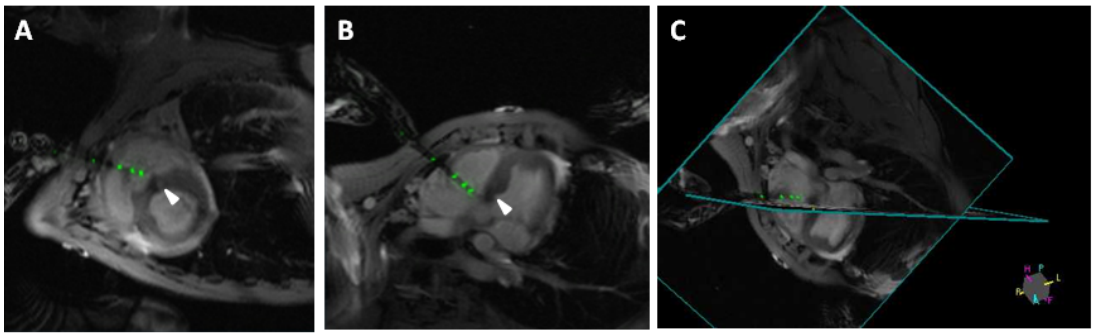

Figure 5.4.5. RV access shown in multiple views and 3D display targeting defect marked by white arrowhead. Lung traversal was minimized and angulation of needle up towards AV valve was observed and could be corrected.

Sample target pathology, a muscular ventricular septal defect, was displayed clearly in previously acquired black blood image roadmaps in the 3D display window along with real-time imaging slices in which the defect also was apparent. Initial chest wall entry placement was aimed to the defect when possible and adjustments were made during needle passage into the ventricle to reach the defect (Figure 5.4.6). In this case, the needle trajectory aimed directly at the defect in the interventricular septum.

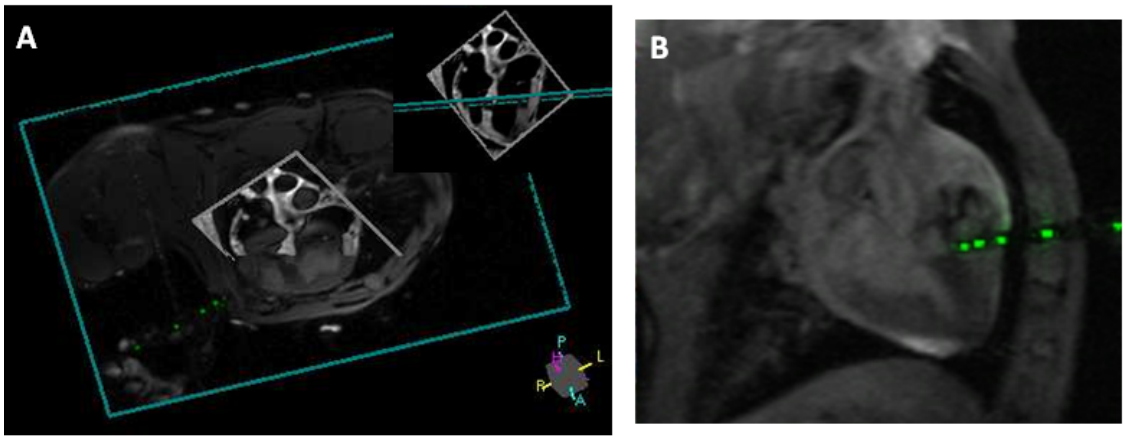

Figure 5.4.6. Targeting muscular VSD with blackblood roadmap to help align initial trajectory (A) and aiming needle at defect in (B).

Left ventricle access was typically approached just lateral to the true cardiac apex and angled to reduce the myocardial path length. During entry into the left ventricle, care was taken to avoid inadvertent puncture of the papillary muscles, particularly posterior. These were visible on scout imaging and real-time slices so an angle was chosen to enter the left ventricle between the papillary muscle and interventricular septum. The needle tip was carefully advanced and positioned also to not risk puncturing the septum while directing the needle towards the LV outflow tract. The needle was also directed to target mitral or aortic structures (Figure 5.4.7).

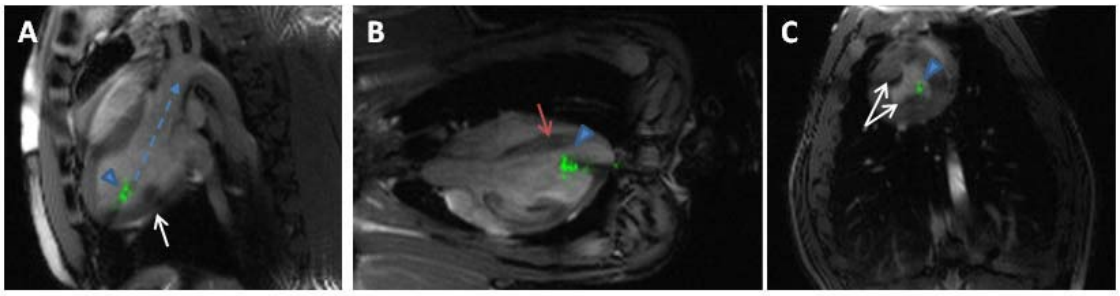

Figure 5.4.7. LV access while targeting aortic valve (A) and avoiding the interventricular septum (B) and papillary muscles (C). White arrow – papillary muscle. Red arrow – interventricular septum. Arrowhead – needle tip.

In cases where a previous area of scar from myocardial infarction was targeted, the real-time MRI slices demonstrated the thin walled regions which were additionally confirmed by the 3D rendering of the prior delayed enhancement acquisitions (Figure 5.4.8).

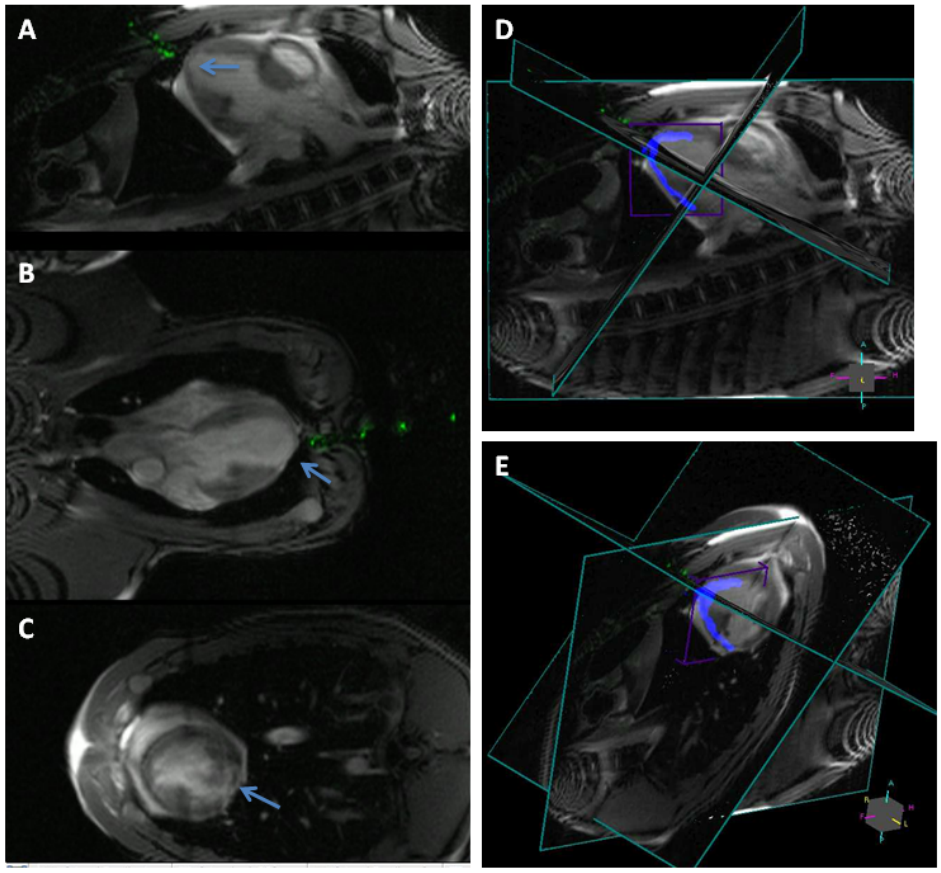

Figure 5.4.8. Targeting infarcted region of LV. Thinned region seen on real-time slices (A-C), marked by blue arrow and corresponding delayed enhancement seen on 3D rendering (D,E), displayed in blue.

Real-time MRI with the active needle also permitted successful pericardial and pleural fluid drainage. Fluid signal was apparent on MR imaging and the operator was able to select an appropriate needle path particularly in effusions that were not global nor uniform around the heart (Figure 5.4.9).

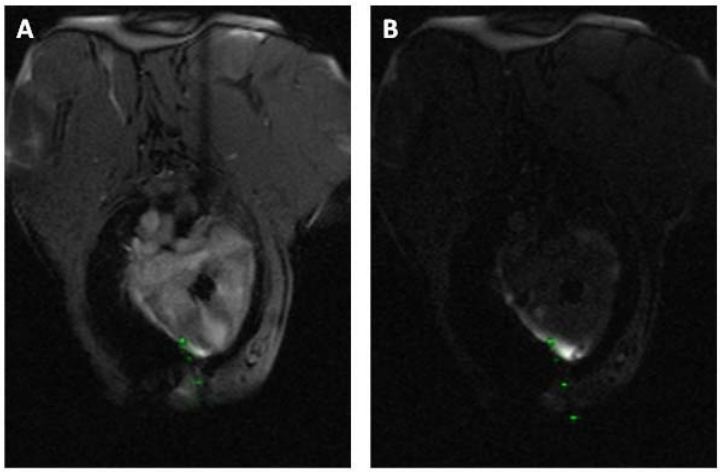

Figure 5.4.9. Pericardial access. Accessing the lateral pericardial space (A) with injection of Gadolinium to confirm entry (B).

5.4.3 Discussion

MR imaging enabled careful planning of a preferred trajectory for transthoracic cardiac puncture. We utilized several different MR acquisition techniques including real-time imaging, MR angiography, and other specialized acquisitions to create clear roadmaps. The greater anatomic information helped the operator avoid important vascular and valvular structures along the path. During the access procedure, changes in needle positioning were quickly identified in the real-time imaging from its active signal and the ability to use features like device-only projection mode to quickly locate the needle tip.

Some perventricular procedures have been attempted with open-chest and hybrid surgical approaches (160) or closed-chest under X-ray (161). These represent potential applications for the MRI-guided approach and demonstrate the advantages of it. Surgical chest wall access can cause considerable pain and convalescence for the

patient. X-ray provides very little information about the cardiac anatomy other than contrast shadows. Structural heart disease and electrophysiology procedures can gain tremendous benefit from MRI for imaging of anatomic targets and employ this approach to safely reach them if alternative cardiac access is desired. This approach is also used selectively for catheterization access in patients with prosthetic heart valves with limited X-ray and ultrasound guidance and multiple punctures have been shown to increase the risk of complications (162,163). Superior image guidance and precise needle positioning could enable single-pass access. In most of the access procedures we performed, only one myocardial wall pass was required other than instances where the trajectory was altered enough by the natural needle movement to warrant repositioning. Aside from cardiac procedures, other non-traditional cardiovascular access sites could be pursued under MRI guidance. Translumbar aortic punctures may also be feasible.

We initially tried to achieve cardiac access using a commercially available passive needle but found this unsatisfactory with current devices and imaging tools. Passive devices typically rely on signal voids to be seen so the ability to visualize these passive artifacts is limited. In some of the trajectories used for right ventricle access, the needle artifact was quite prominent due to the perpendicular position relative to the bore of the magnet. Figure 5.4.10 shows an example of RV access attempted with a passive needle and the post-mortem examination which showed inadvertent puncture of the interventricular septum beneath the tricuspid valve.

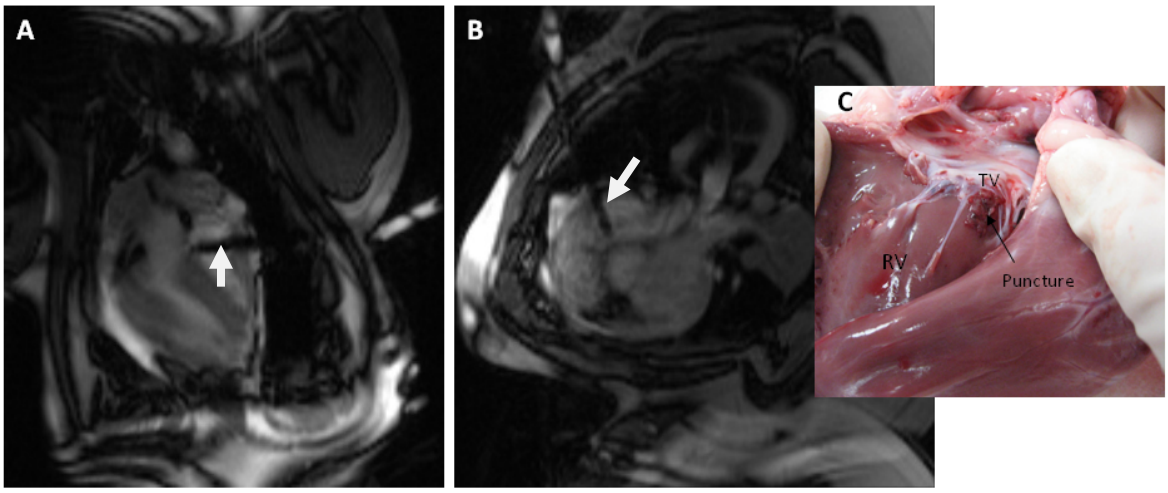

Figure 5.4.10. RV access with passive needle. Needle tip position is unclear in both slice views (A, B) which resulted in advertent septal puncture evident in post-mortem examination (C).

Furthermore, the additional time necessary to identify needle location, particularly in off-target punctures, as seen in the jugular access portion of this work may be detrimental in this high-risk location with considerable cardiac and respiratory motion. Improving the conspicuity of passive device signals and developing tracking algorithms may help and permit these devices to be used (164,165). Active device safety is also an active area of research as discussed earlier where interrupted transmission lines and optical approaches may help ensure safe devices.

For safe percutaneous cardiac access, avoidance of the coronay arteries is also critical. Spatial and temporal resolution limitations of MRI make coronary imaging limited with this technique but this could be addressed with the use of fusion of complementary alternate image guidance. CT coronary angiography can provide non-invasive three-dimensional imaging of the coronary arteries. A CT study conducted prior to the MR

procedure could be co-registered with the real-time MRI and serve as a roadmap to avoid injuring these vessels (121).

Information from MRI also is limited in the lung traversal part of this approach because of the lack of proton-containing signal. The needle can typically still be visualized in these low signal areas but the addition of an inherent signal source may be superior. Other than incorporating optical visualization through an endoscope or similar, there is not a particularly good method for lung tissue imaging. Additionally, while we attempt to minimize passage through lung tissue and have not experienced specific lung problems, approaches may need to be pursued such as using sealed ports or intentional lung collapse prior to prevent potential pneumothorax.

MRI also permits close monitoring and potential for quick intervention if necessary. Cardiac motion was followed on the imaging slices, particularly in the short-axis view which was dedicated primarily to cardiac monitoring. As seen in Figure 5.4.11, any pericardial or pleural fluid accumulations could be rapidly identified and also treated as the pericardiocentesis example shows.

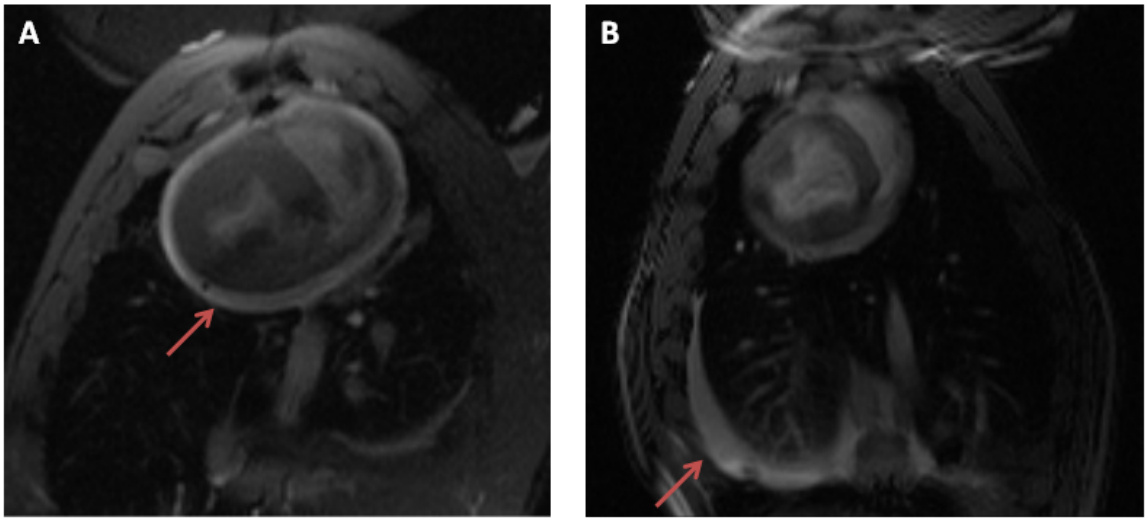

Figure 5.4.11. Complication monitoring taking advantage of inherent MRI contrast. Pericardial (A) and pleural (B) fluid accumulation can be easily recognized and treated.

MRI techniques such as tagging or myocardial velocimetry could also be used to evaluate the impact of this procedure on regional wall motion.

Pericardiocentesis is performed clinically with a blind approach or with X-ray or ultrasound imaging to guide or confirm pericardial puncture. MRI offers superior visualization of the pericardial fluid accumulation and its specific distribution without any exogenous contrast. While global effusions may be readily accessible from any approach, reaching an area of isolated fluid can be more difficult without adequate imaging.

5.5 Chapter Summary and Contributions

In this work, we first demonstrated successful real-time MRI guided vascular access in swine. MRI-guided vascular access could enable procedures to be performed entirely in the MR suite with greater anatomic information. Access was achieved with a newly developed active visualization needle and passive comparator using reduced field of view imaging. Compared with a passive needle, the active “profiling” needle had a signal profile that permitted rapid and clear device and tip localization and which resulted in higher success rates and shorter procedures. Operator experience did not significantly impact success rate; by contrast, operator technique in selecting and following trajectory plans proved important.

This approach also permitted more complex percutaneous cardiovascular access where enhanced image guidance is necessary for such procedures to be performed safely. MRI guidance enabled a planned and closely monitored approach for more challenging cardiovascular access. Transhepatic vascular access built on the experience from jugular access and used the unique vessel contrast of MRI to efficiently access the hepatic and portal veins in swine.

For direct cardiac access, targeting both right and left ventricle access in swine, skin to cardiac entry trajectories were selected based on previously acquired MRI roadmaps in conjunction with real-time imaging to minimize path lengths, avoid critical structures, and target distinct pathologies. Real-time MRI with an actively visualized needle enabled continual monitoring of needle position and adjustment of the path as necessary. MRI also permitted pericardial puncture for pericardiocentesis, particularly in localized effusions. Overall our active needle combined with real-time MRI provided a

versatile tool for conventional and novel cardiovascular access that may have utility in non-surgical treatments for cardiovascular disease.

CHAPTER

6

CONCLUSION

6.1 Project Summary

This work provided a comprehensive look at the different components necessary to bring MRI-guided cardiovascular interventions closer to a clinical reality. In the first part, we address the lack of compatible devices and demonstrated how local coil designs could be implemented in functional devices with active visualization to permit evaluation of several different cardiovascular interventions. An active needle with elongated loop coil provided clear tip positioning and markers of needle shaft positioning and depth. For better visualization of cardiac occluder delivery, incorporating the device in a loopless delivery cable design gave the operator greater confidence in device deployment and positioning. In exploring extra-anatomic bypass procedures like TIPS, a concentric nitinol hypotube design formed the components of a loopless antenna to provide the ability to position and advance an excimer laser while visualizing device curvature and orientation. We also developed methods to evaluate these devices and their imaging performance to accurately guide interventions. We then demonstrated their utility *in vivo* during deployment in preclinical feasibility experiments.

Having developed a set of MRI devices, we also undertook experiments to understand further the parameters that impact the safety of these devices, and then set about to develop a feedback system to control or mitigate heating. Through initial

phantom studies, we were able to identify key parameters and important considerations for future device evaluation of RF safety. Effects of device positioning were demonstrated in addition to the variability that could be introduced with accessory devices like coaxial cable during phantom testing. Evaluations of SAR enlightened considerations for testing conditions to simulate realistic power deposition to correlate to *in vivo* use. By incorporating internal temperature sensors into device prototypes, we were then able to evaluate this potential monitoring technique as a method to more accurately characterize the heating profiles of complex devices and provide a unique temperature monitoring ability. We also used this approach for evaluating device heating *in vivo* and *in situ* in large animals to demonstrate the level of heating in simulated use conditions and the contribution of blood flow to heat dissipation. The temperature tracking and additional device monitoring capabilities then were incorporated into a dynamic scanner feedback control system to offer added patient safety during initial clinical trials.

In the final part of this work, we demonstrated the utility of MRI guidance to enable traditional and complex cardiovascular access. For central vessel access, we developed an imaging approach and procedure workflow to enable vascular access within the MRI suite. Comparison of actively and passively visualized needles during jugular access in swine revealed the benefit of active visualization in slightly improving success rates with significant reductions in the procedure time and number of needle passes. Enhanced imaging guidance also enabled less experienced operators to have similar outcomes as those who regularly achieve vascular access. Similar approaches were used with the active needle and MRI guidance to permit trajectory planning and closely monitored complex cardiovascular access with transabdominal hepatic vascular access and transthoracic direct cardiac access. Successful access was performed to

the hepatic and portal veins using the active needle with MRI informing the approach with constant visualization of the vessels without the need for contrast and ability to avoid inadvertent puncture of other nearby structures. Direct cardiac access to the right and left ventricles were performed with a planned approach that allowed safe entry to the heart. This may offer a potential alternative to surgical access for a variety of structural heart and other interventions where current endovascular approaches are insufficient.

Together, this work provided the requisite actively visualized devices, considered device safety and approaches to improved testing and monitoring, and finally demonstrated and evaluated the ability of MRI guidance with active devices to perform traditional and novel cardiovascular procedures.

6.2 Future Directions

Interventional MRI device development will continue to benefit from further improvement in manufacturing techniques and more important, continued miniaturization of electronic components for active device development. While cell phone, RF identification, and other communication technologies have substantially reduced the size of many commercially available elements, they are often still too big for devices that might fill constructions that are as small as 1 mm or less in the case of guidewires. Microfabrication techniques can produce relatively low-cost coils with embedded tuning components and potentially offer miniaturized transmission lines with switches, traps, or other components to further ensure safe device performance in the MRI environment (166-168). Incorporating distal on board preamplifiers and optical converters could enable optical transmission to the scanner and reduce challenges with wire lengths and coupling. Novel polymer constructions could also help limit the need for conductive materials used in traditional devices like guidewires and catheters. Image-based visualization techniques could also change the requirements for device characteristics and consequently design.

With these continual advances in device design and manufacturing, device safety will continue to improve as well. The experimental testing methods have evolved with increased understanding of the factors in play and we have reported additional methods to improve this approach. The experimental data in phantom and in vivo studies can be used to further advance the development and validation of electromagnetic simulation techniques. Simulation can be computationally extensive and time-consuming as a result but also could allow investigation of numerous variables in a controlled test method. Current simulations, however, must make many simplifications which can limit

their utility and miss important considerations. With further development of this simulation data, the experimental data we generated and approach to dynamically evaluate measured heating will serve as valuable components in validating these methods. Other promising approaches to reducing device and implant heating under investigation include parallel transmission and control of the B and E field distributions and device coupling which could help reduce heating potential (169). More sophisticated monitoring systems building upon the one described in this work also could be implemented for normal device use.

MRI guided procedures will continue to benefit from the continued work in real-time MRI acquisition and reconstruction. Parallel imaging with multi-channel coils and efficient reconstruction approaches can provide greater temporal resolution particularly beneficial for delicate cardiac procedures (170). Improved spatial resolution would provide enhanced guidance for targeting procedures to small targets. The unique direct cardiac access approach we presented requires a reliable percutaneous closure method for the access site whose deployment could also be informed by MRI guidance as shown with the demonstration of the VSD occluder apical delivery. Selecting the proper targets for this technology is also critical for its successful implementation. Many cardiovascular imaging techniques are available and constantly being developed and improved to guide less invasive procedures. One must consider the features of each to determine the best modality for the desired procedure and the components that are necessary for its success. Together, these can offer patients safe and efficacious procedures with better outcomes, faster recovery and improved quality of life.

REFERENCES

1. Hurst JW. History of cardiac catheterization In: King SBI, Douglas JSJ, eds. Coronary Arteriography and Angioplasty. New York McGraw-Hill 1985.

2. Kwong RY. Cardiovascular Magnetic Resonance Imaging Springer, 2007.

3. Griswold MA, Jakob PM, Heidemann RM, et al. Generalized autocalibrating partially parallel acquisitions (GRAPPA). Magn Reson Med 2002;47:1202-10.

4. Kellman P, Epstein FH, McVeigh ER. Adaptive sensitivity encoding incorporating temporal filtering (TSENSE). Magn Reson Med 2001;45:846-52.

5. Pruessmann KP, Weiger M, Scheidegger MB, Boesiger P. SENSE: sensitivity encoding for fast MRI. Magn Reson Med 1999;42:952-62.

6. Guttman MA, Ozturk C, Raval AN, et al. Interventional cardiovascular procedures guided by real-time MR imaging: an interactive interface using multiple slices, adaptive projection modes and live 3D renderings. J Magn Reson Imaging 2007;26:1429-35.

7. Santos JM, Wright GA, Pauly JM. Flexible real-time magnetic resonance imaging framework. Conf Proc IEEE Eng Med Biol Soc 2004;2:1048-51.

8. Schirra CO, Weiss S, Krueger S, et al. Toward true 3D visualization of active catheters using compressed sensing. Magn Reson Med 2009;62:341-7.

9. George A, Derbyshire J, Saybasili H, et al. Fast, Robust 3D Visualization and Automatic Slice Repositioning ("Snap-To") for MR-Guided Interventions Using Active Device "Profiling". ISMRM 17th Annual Scientific Meeting Honolulu, HI 2009.

10. Elgort DR, Wong EY, Hillenbrand CM, Wacker FK, Lewin JS, Duerk JL. Real-time catheter tracking and adaptive imaging. J Magn Reson Imaging 2003;18:621-6.

11. Patil S, Bieri O, Jhooti P, Scheffler K. Automatic slice positioning (ASP) for passive real-time tracking of interventional devices using projection-reconstruction imaging with echo-dephasing (PRIDE). Magn Reson Med 2009.

12. Kantor HL, Briggs RW, Balaban RS. In vivo 31P nuclear magnetic resonance measurements in canine heart using a catheter-coil. Circ Res 1984;55:261-6.

13. Hurst GC, Hua J, Duerk JL, Cohen AM. Intravascular (catheter) NMR receiver probe: preliminary design analysis and application to canine iliofemoral imaging. Magn Reson Med 1992;24:343-57.

14. Martin AJ, Plewes DB, Henkelman RM. MR imaging of blood vessels with an intravascular coil. J Magn Reson Imaging 1992;2:421-9.

15. Omary RA, Green JD, Schirf BE, Li Y, Finn JP, Li D. Real-time magnetic resonance imaging-guided coronary catheterization in swine. Circulation 2003;107:2656-9.

16. Serfaty JM, Yang X, Foo TK, Kumar A, Derbyshire A, Atalar E. MRI-guided coronary catheterization and PTCA: A feasibility study on a dog model. Magn Reson Med 2003;49:258-63.

17. Spuentrup E, Ruebben A, Schaeffter T, Manning WJ, Gunther RW, Buecker A. Magnetic resonance--guided coronary artery stent placement in a swine model. Circulation 2002;105:874-9.

18. Manke C, Nitz WR, Djavidani B, et al. MR imaging-guided stent placement in iliac arterial stenoses: a feasibility study. Radiology 2001;219:527-34.

19. Elgort DR, Hillenbrand CM, Zhang S, et al. Image-guided and -monitored renal artery stenting using only MRI. J Magn Reson Imaging 2006;23:619-27.

20. Raman VK, Karmarkar PV, Guttman MA, et al. Real-time magnetic resonance-guided endovascular repair of experimental abdominal aortic aneurysm in swine. J Am Coll Cardiol 2005;45:2069-77.

21. Eggebrecht H, Kuhl H, Kaiser GM, et al. Feasibility of real-time magnetic resonance-guided stent-graft placement in a swine model of descending aortic dissection. Eur Heart J 2006;27:613-20.

22. Raval AN, Telep JD, Guttman MA, et al. Real-time magnetic resonance imaging-guided stenting of aortic coarctation with commercially available catheter devices in Swine. Circulation 2005;112:699-706.

23. Krueger JJ, Ewert P, Yilmaz S, et al. Magnetic resonance imaging-guided balloon angioplasty of coarctation of the aorta: a pilot study. Circulation 2006;113:1093-100.

24. Raval AN, Karmarkar PV, Guttman MA, et al. Real-time magnetic resonance imaging-guided endovascular recanalization of chronic total arterial occlusion in a swine model. Circulation 2006;113:1101-7.

25. Anderson KJ, Leung G, Dick AJ, Wright GA. Forward-looking intravascular orthogonal-solenoid coil for imaging and guidance in occlusive arterial disease. Magn Reson Med 2008;60:489-95.

26. Kee ST, Ganguly A, Daniel BL, et al. MR-guided transjugular intrahepatic portosystemic shunt creation with use of a hybrid radiography/MR system. J Vasc Interv Radiol 2005;16:227-34.

27. Arepally A, Karmarkar PV, Weiss C, Atalar E. Percutaneous MR imaging-guided transvascular access of mesenteric venous system: study in swine model. Radiology 2006;238:113-8.

28. Raval AN, Karmarkar PV, Guttman MA, et al. Real-time MRI guided atrial septal puncture and balloon septostomy in swine. Catheter Cardiovasc Interv 2006;67:637-43.

29. Elagha AA, Kocaturk O, Guttman MA, et al. Real-time MR imaging-guided laser atrial septal puncture in swine. J Vasc Interv Radiol 2008;19:1347-53.

30. Buecker A, Spuentrup E, Grabitz R, et al. Magnetic resonance-guided placement of atrial septal closure device in animal model of patent foramen ovale. Circulation 2002;106:511-5.

31. Rickers C, Jerosch-Herold M, Hu X, et al. Magnetic resonance image-guided transcatheter closure of atrial septal defects. Circulation 2003;107:132-8.

32. Schalla S, Saeed M, Higgins CB, Weber O, Martin A, Moore P. Balloon sizing and transcatheter closure of acute atrial septal defects guided by magnetic resonance fluoroscopy: assessment and validation in a large animal model. J Magn Reson Imaging 2005;21:204-11.

33. Kuehne T, Yilmaz S, Meinus C, et al. Magnetic resonance imaging-guided transcatheter implantation of a prosthetic valve in aortic valve position: Feasibility study in swine. J Am Coll Cardiol 2004;44:2247-9.

34. McVeigh ER, Guttman MA, Lederman RJ, et al. Real-time interactive MRI-guided cardiac surgery: aortic valve replacement using a direct apical approach. Magn Reson Med 2006;56:958-64.

35. Bracken JA, Komljenovic P, Lillaney PV, Fahrig R, Rowlands JA. Closed-bore XMR (CBXMR) systems for aortic valve replacement: x-ray tube imaging performance. Med Phys 2009;36:1086-97.

36. Lederman RJ, Guttman MA, Peters DC, et al. Catheter-based endomyocardial injection with real-time magnetic resonance imaging. Circulation 2002;105:1282-4.

37. Corti R, Badimon J, Mizsei G, et al. Real time magnetic resonance guided endomyocardial local delivery. Heart 2005;91:348-53.

38. Kraitchman DL, Heldman AW, Atalar E, et al. In vivo magnetic resonance imaging of mesenchymal stem cells in myocardial infarction. Circulation 2003;107:2290-3.

39. Barbash IM, Leor J, Feinberg MS, et al. Interventional magnetic resonance imaging for guiding gene and cell transfer in the heart. Heart 2004;90:87-91.

40. Dick AJ, Guttman MA, Raman VK, et al. Magnetic resonance fluoroscopy allows targeted delivery of mesenchymal stem cells to infarct borders in swine. Circulation 2003;108:2899-904.

41. Saeed M, Martin A, Jacquier A, et al. Permanent coronary artery occlusion: cardiovascular MR imaging is platform for percutaneous transendocardial delivery and assessment of gene therapy in canine model. Radiology 2008;249:560-71.

42. Andreassi MG, Ait-Ali L, Botto N, Manfredi S, Mottola G, Picano E. Cardiac catheterization and long-term chromosomal damage in children with congenital heart disease. Eur Heart J 2006;27:2703-8.

43. Vano E, Gonzalez L, Fernandez JM, Haskal ZJ. Eye lens exposure to radiation in interventional suites: caution is warranted. Radiology 2008;248:945-53.

44. Goldstein JA, Balter S, Cowley M, Hodgson J, Klein LW. Occupational hazards of interventional cardiologists: prevalence of orthopedic health problems in contemporary practice. Catheter Cardiovasc Interv 2004;63:407-11.

45. Razavi R, Hill DL, Keevil SF, et al. Cardiac catheterisation guided by MRI in children and adults with congenital heart disease. Lancet 2003;362:1877-82.

46. Muthurangu V, Taylor A, Andriantsimiavona R, et al. Novel method of quantifying pulmonary vascular resistance by use of simultaneous invasive pressure monitoring and phase-contrast magnetic resonance flow. Circulation 2004;110:826-34.

47. Kuehne T, Yilmaz S, Schulze-Neick I, et al. Magnetic resonance imaging guided catheterisation for assessment of pulmonary vascular resistance: in vivo validation and clinical application in patients with pulmonary hypertension. Heart 2005;91:1064-1069.

48. Kuehne T, Saeed M, Higgins CB, et al. Endovascular stents in pulmonary valve and artery in swine: feasibility study of MR imaging-guided deployment and postinterventional assessment. Radiology 2003;226:475-81.

49. Khambadkone S, Coats L, Taylor A, et al. Percutaneous pulmonary valve implantation in humans: results in 59 consecutive patients. Circulation 2005;112:1189-97.

50. Tzifa A, Krombach GA, Kramer N, et al. Magnetic Resonance-Guided Cardiac Interventions Using Magnetic Resonance-Compatible Devices: A Preclinical Study and First-in-Man Congenital Interventions. Circ Cardiovasc Interv.

51. Tzifa A, Razavi R. Test occlusion of Fontan fenestration: unique contribution of interventional MRI. Heart.

52. Dickfeld T, Calkins H, Zviman M, et al. Anatomic stereotactic catheter ablation on three-dimensional magnetic resonance images in real time. Circulation 2003;108:2407-13.

53. Kolandaivelu A, Zviman MM, Castro V, Lardo AC, Berger RD, Halperin HR. Noninvasive assessment of tissue heating during cardiac radiofrequency ablation using MRI thermography. Circ Arrhythm Electrophysiol;3:521-9.

54. Dickfeld T, Kato R, Zviman M, et al. Characterization of radiofrequency ablation lesions with gadolinium-enhanced cardiovascular magnetic resonance imaging. J Am Coll Cardiol 2006;47:370-8.

55. McGann CJ, Kholmovski EG, Oakes RS, et al. New magnetic resonance imaging-based method for defining the extent of left atrial wall injury after the ablation of atrial fibrillation. J Am Coll Cardiol 2008;52:1263-71.

56. Nordbeck P, Bauer WR, Fidler F, et al. Feasibility of Real-Time MRI With a Novel Carbon Catheter for Interventional Electrophysiology. Circ Arrhythmia Electrophysiol 2009;2:258-267.

57. Susil RC, Yeung CJ, Halperin HR, Lardo AC, Atalar E. Multifunctional interventional devices for MRI: a combined electrophysiology/MRI catheter. Magn Reson Med 2002;47:594-600.

58. Dukkipati SR, Mallozzi R, Schmidt EJ, et al. Electroanatomic mapping of the left ventricle in a porcine model of chronic myocardial infarction with magnetic resonance-based catheter tracking. Circulation 2008;118:853-62.

59. Nazarian S, Kolandaivelu A, Zviman MM, et al. Feasibility of real-time magnetic resonance imaging for catheter guidance in electrophysiology studies. Circulation 2008;118:223-9.

60. Gutierrez LF, Silva R, Ozturk C, et al. Technology preview: X-ray fused with magnetic resonance during invasive cardiovascular procedures. Catheter Cardiovasc Interv 2007;70:773-82.

61. de Silva R, Gutierrez LF, Raval AN, McVeigh ER, Ozturk C, Lederman RJ. X-ray fused with magnetic resonance imaging (XFM) to target endomyocardial injections: validation in a swine model of myocardial infarction. Circulation 2006;114:2342-50.

62. Ratnayaka K, Raman VK, Faranesh AZ, et al. Antegrade percutaneous closure of membranous ventricular septal defect using X-ray fused with magnetic resonance imaging. JACC Cardiovasc Interv 2009;2:224-30.

63. Tronnier VM, Wirtz CR, Knauth M, et al. Intraoperative diagnostic and interventional magnetic resonance imaging in neurosurgery. Neurosurgery 1997;40:891-902.

64. Weiss CR, Nour SG, Lewin JS. MR-guided biopsy: a review of current techniques and applications. J Magn Reson Imaging 2008;27:311-25.

65. Rieke V, Butts Pauly K. MR thermometry. J Magn Reson Imaging 2008;27:376-90.

66. Smith KA, Carrino J. MRI-guided interventions of the musculoskeletal system. J Magn Reson Imaging 2008;27:339-46.

67. Cleary K, Melzer A, Watson V, Kronreif G, Stoianovici D. Interventional robotic systems: applications and technology state-of-the-art. Minim Invasive Ther Allied Technol 2006;15:101-13.

68. Rubin DL, Ratner AV, Young SW. Magnetic susceptibility effects and their application in the development of new ferromagnetic catheters for magnetic resonance imaging. Invest Radiol 1990;25:1325-32.

69. Bakker CJ, Hoogeveen RM, Weber J, van Vaals JJ, Viergever MA, Mali WP. Visualization of dedicated catheters using fast scanning techniques with potential for MR-guided vascular interventions. Magn Reson Med 1996;36:816-20.

70. Omary RA, Unal O, Koscielski DS, et al. Real-time MR imaging-guided passive catheter tracking with use of gadolinium-filled catheters. J Vasc Interv Radiol 2000;11:1079-85.

71. Miquel ME, Hegde S, Muthurangu V, et al. Visualization and tracking of an inflatable balloon catheter using SSFP in a flow phantom and in the heart and great vessels of patients. Magn Reson Med 2004;51:988-95.

72. Kozerke S, Hegde S, Schaeffter T, Lamerichs R, Razavi R, Hill DL. Catheter tracking and visualization using 19F nuclear magnetic resonance. Magn Reson Med 2004;52:693-7.

73. Magnusson P, Johansson E, Mansson S, et al. Passive catheter tracking during interventional MRI using hyperpolarized 13C. Magn Reson Med 2007;57:1140-7.

74. Dharmakumar R, Koktzoglou I, Tang R, Harris KR, Beohar N, Li D. Off-resonance positive contrast imaging of a passive endomyocardial catheter in swine. Phys Med Biol 2008;53:N249-57.

75. Edelman RR, Storey P, Dunkle E, et al. Gadolinium-enhanced off-resonance contrast angiography. Magn Reson Med 2007;57:475-84.

76. Krueger S, Schmitz S, Weiss S, et al. An MR guidewire based on micropultruded fiber-reinforced material. Magn Reson Med 2008;60:1190-6.

77. Mekle R, Hofmann E, Scheffler K, Bilecen D. A polymer-based MR-compatible guidewire: a study to explore new prospects for interventional peripheral magnetic resonance angiography (ipMRA). J Magn Reson Imaging 2006;23:145-55.

78. Dumoulin CL, Souza SP, Darrow RD. Real-time position monitoring of invasive devices using magnetic resonance. Magn Reson Med 1993;29:411-5.

79. Ocali O, Atalar E. Intravascular magnetic resonance imaging using a loopless catheter antenna. Magn Reson Med 1997;37:112-8.

80. Kuehne T, Fahrig R, Butts K. Pair of resonant fiducial markers for localization of endovascular catheters at all catheter orientations. J Magn Reson Imaging 2003;17:620-4.

81. Quick HH, Zenge MO, Kuehl H, et al. Interventional magnetic resonance angiography with no strings attached: wireless active catheter visualization. Magn Reson Med 2005;53:446-55.

82. Eggers H, Weiss S, Boernert P, Boesiger P. Image-based tracking of optically detunable parallel resonant circuits. Magn Reson Med 2003;49:1163-74.

83. Wong EY, Zhang Q, Duerk JL, Lewin JS, Wendt M. An optical system for wireless detuning of parallel resonant circuits. J Magn Reson Imaging 2000;12:632-8.

84. Celik H, Uluturk A, Tali T, Atalar E. A catheter tracking method using reverse polarization for MR-guided interventions. Magn Reson Med 2007;58:1224-31.

85. Bock M, Wacker FK. MR-guided intravascular interventions: techniques and applications. J Magn Reson Imaging 2008;27:326-38.

86. Ratnayaka K, Faranesh AZ, Guttman MA, Kocaturk O, Saikus CE, Lederman RJ. Interventional cardiovascular magnetic resonance: still tantalizing. J Cardiovasc Magn Reson 2008;10:62.

87. Dukkipati SR, Mallozzi R, Schmidt EJ, et al. Electroanatomic Mapping of the Left Ventricle in a Porcine Model of Chronic Myocardial Infarction With Magnetic Resonance-Based Catheter Tracking. Circulation 2008.

88. Quick HH, Kuehl H, Kaiser G, Bosk S, Debatin JF, Ladd ME. Inductively coupled stent antennas in MRI. Magn Reson Med 2002;48:781-90.

89. Kanal E, Shellock FG, Talagala L. Safety considerations in MR imaging. Radiology 1990;176:593-606.

90. Hill DL, McLeish K, Keevil SF. Impact of electromagnetic field exposure limits in Europe: is the future of interventional MRI safe? Acad Radiol 2005;12:1135-42.

91. Kanal E, Borgstede JP, Barkovich AJ, et al. American College of Radiology White Paper on MR Safety. AJR Am J Roentgenol 2002;178:1335-47.

92. Dempsey MF, Condon B, Hadley DM. Investigation of the factors responsible for burns during MRI. J Magn Reson Imaging 2001;13:627-31.

93. Ham CL, Engels JM, van de Wiel GT, Machielsen A. Peripheral nerve stimulation during MRI: effects of high gradient amplitudes and switching rates. J Magn Reson Imaging 1997;7:933-7.

94. Bottomley PA, Redington RW, Edelstein WA, Schenck JF. Estimating radiofrequency power deposition in body NMR imaging. Magn Reson Med 1985;2:336-49.

95. Shellock FG, Schaefer DJ. Radiofrequency Energy-Induced Heating during Magnetic Resonance Procedures: Laboratory and Clinical Experiences In: Shellock FG, ed. *Magentic Resonance Procedures: Health Effects and Safety*, 2001:62.

96. Athey TW. Current FDA guidance for MR patient exposure and considerations for the future. Ann N Y Acad Sci 1992;649:242-57.

97. Smith CD, Nyenhuis JA, Kildishev AV. Health Effects of Induced Electric Fields: Implications for Metallic Implants In: Shellock FG, ed. *Magentic Resonance Procedures: Health Effects and Safety*, 2001:405-406.

98. Konings MK, Bartels LW, Smits HF, Bakker CJ. Heating around intravascular guidewires by resonating RF waves. J Magn Reson Imaging 2000;12:79-85.

99. Liu CY, Farahani K, Lu DS, Duckwiler G, Oppelt A. Safety of MRI-guided endovascular guidewire applications. J Magn Reson Imaging 2000;12:75-8.

100. Nitz WR, Oppelt A, Renz W, Manke C, Lenhart M, Link J. On the heating of linear conductive structures as guide wires and catheters in interventional MRI. J Magn Reson Imaging 2001;13:105-14.

101. Ladd ME, Quick HH. Reduction of resonant RF heating in intravascular catheters using coaxial chokes. Magn Reson Med 2000;43:615-9.

102. Seeber DA, Jevtic J, Menon A. Floating shield current suppression trap Concepts in Magnetic Resonance Part B: Magnetic Resonance Engineering 2004;21B:26-31.

103. Weiss S, Vernickel P, Schaeffter T, Schulz V, Gleich B. Transmission line for improved RF safety of interventional devices. Magn Reson Med 2005;54:182-9.

104. Weiss S, Wirtz D, David B, et al. In vivo evaluation and proof of radiofrequency safety of a novel diagnostic MR-electrophysiology catheter. Magn Reson Med.

105. Hillenbrand CM, Elgort DR, Wong EY, et al. The bazooka coil: a novel dual-purpose device for active visualization and reducation of cable currents in electrically conductive endovascular instruments. . ISMRM 13th Scientific Meeting & Exhibition Miami, Florida 2005:197.

106. Venook R, Overall W, Pauly J, SCott CG. Reducing and monitoring resonant heating in MR guidewires ISMRM 14th Scientific Meeting & Exhibition. Seattle, Washington 2006:2037.

107. Fandrey S, Weiss S, Muller J. Development of an active intravascular MR device with an optical transmission system. IEEE Trans Med Imaging 2008;27:1723-7.

108. Ladd ME, Erhart P, Debatin JF, Romanowski BJ, Boesiger P, McKinnon GC. Biopsy needle susceptibility artifacts. Magn Reson Med 1996;36:646-51.

109. Constantinides CD, Atalar E, McVeigh ER. Signal-to-noise measurements in magnitude images from NMR phased arrays. Magn Reson Med 1997;38:852-7.

110. Henkelman RM. Measurement of signal intensities in the presence of noise in MR images. Med Phys 1985;12:232-3.

111. George AK, Derbyshire JA, Saybasili H, et al. Visualization of active devices and automatic slice repositioning ("SnapTo") for MRI-guided interventions. Magn Reson Med;63:1070-9.

112. Frahm C, Gehl HB, Melchert UH, Weiss HD. Visualization of magnetic resonance-compatible needles at 1.5 and 0.2 Tesla. Cardiovasc Intervent Radiol 1996;19:335-40.

113. Lewin JS, Duerk JL, Jain VR, Petersilge CA, Chao CP, Haaga JR. Needle localization in MR-guided biopsy and aspiration: effects of field strength, sequence design, and magnetic field orientation. AJR Am J Roentgenol 1996;166:1337-45.

114. Kee ST, Rhee JS, Butts K, et al. 1999 Gary J. Becker Young Investigator Award. MR-guided transjugular portosystemic shunt placement in a swine model. J Vasc Interv Radiol 1999;10:529-35.

115. Reichenbach JR, Wurdinger S, Pfleiderer SO, Kaiser WA. Comparison of artifacts produced from carbon fiber and titanium alloy needles at 1.5 T MR imaging. J Magn Reson Imaging 2000;11:69-74.

116. Thomas C, Rempp H, Springer F, et al. First performance evaluation of new 3D MRI fluoroscopy system for MRI-guided musculoskeletal interventions in high field Seventh Interventional MRI Symposium Baltimore, MD 2008.

117. Muller-Bierl BM, Martirosian P, Graf H, et al. Biopsy needle tips with markers--MR compatible needles for high-precision needle tip positioning. Med Phys 2008;35:2273-8.

118. Gohde SC, Pfammatter T, Steiner P, Erhart P, Romanowski BJ, Debatin JF. MR-guided cholecystostomy: assessment of biplanar, real-time needle tracking in three pigs. Cardiovasc Intervent Radiol 1997;20:295-9.

119. Leung DA, Debatin JF, Wildermuth S, et al. Real-time biplanar needle tracking for interventional MR imaging procedures. Radiology 1995;197:485-8.

120. Ratnayaka K, Saikus CE, Faranesh AZ, et al. Closed Chest Transthoracic Perventricular Ventricular Septal Defect Closure Under Real-time MRI Society for Cardiovascular Magnetic Resonance Scientific Sessions Phoenix, AZ 2010:O24.

121. Barbash IM, Saikus CE, Faranesh AZ, et al. Direct Percutaneous Left Ventricular Access and Closure Using Real-Time MRI SCMR Scientific Sessions Nice, France 2011.

122. Lu W, Pauly KB, Gold GE, Pauly JM, Hargreaves BA. SEMAC: Slice Encoding for Metal Artifact Correction in MRI. Magn Reson Med 2009;62:66-76.

123. Garcia-Pagan JC, Caca K, Bureau C, et al. Early use of TIPS in patients with cirrhosis and variceal bleeding. N Engl J Med;362:2370-9.

124. Park SM, Nyenhuis JA, Smith CD, et al. Gelled Versus Nongelled Phantom Material for Measurement of MRI-Induced Temperature Increases with Bioimplants IEEE Transactions on Magnetics 2003;39:3367-71.

125. ASTM. Standard Test Method for Measurement of Radio Frequency Induced Heating On or Near Passive Implants During Magnetic Resonance Imaging 2009.

126. Amjad A, Kamondetdacha R, Kildishev AV, Park SM, Nyenhuis JA. Power Deposition Inside a Phantom for Testing of MRI Heating IEEE Trans Magnetics 2005;41:4185-4187.

127. Kocaturk O, Kim AH, Saikus CE, et al. Active two-channel 0.035" guidewire for interventional cardiovascular MRI. J Magn Reson Imaging 2009;30:461-5.

128. Kainz W, Fidler F, Bobgan J, et al. Variation of whole body averaged phantom specific absorption rate (SAR) in seven different 1.5 T MR systems 19th International Zurich Symposium on Electromagnetic Compatibility Singapore 2008.

129. NEMA. Characterization of the Specific Absorption Rate for Magnetic Resonance Imaging Systems 2008.

130. Nordbeck P, Ritter O, Weiss I, et al. Impact of imaging landmark on the risk of MRI-related heating near implanted medical devices like cardiac pacemaker leads. Magn Reson Med.

131. Nordbeck P, Fidler F, Weiss I, et al. Spatial distribution of RF-induced E-fields and implant heating in MRI. Magn Reson Med 2008;60:312-9.

132. Tong N, Shmatukha A, Asmah P, Stainsby J. Practical aspects of MR imaging in the presence of conductive guide wires. Phys Med Biol;55:N13-22.

133. Martin AJ, Baek B, Acevedo-Bolton G, Higashida RT, Comstock J, Saloner DA. MR imaging during endovascular procedures: an evaluation of the potential for catheter heating. Magn Reson Med 2009;61:45-53.

134. Mattei E, Triventi M, Calcagnini G, et al. Temperature and SAR measurement errors in the evaluation of metallic linear structures heating during MRI using fluoroptic probes. Phys Med Biol 2007;52:1633-46.

135. Josephson ME. Clinical cardiac electrophysiology: techniques and interpretations Lippincott Williams & Wilkins 2008.

136. Hoffmann BA, Koops A, Rostock T, et al. Interactive real-time mapping and catheter ablation of the cavotricuspid isthmus guided by magnetic resonance imaging in a porcine model. Eur Heart J;31:450-6.

137. Schmidt EJ, Mallozzi RP, Thiagalingam A, et al. Electroanatomic mapping and radiofrequency ablation of porcine left atria and atrioventricular nodes using magnetic resonance catheter tracking. Circ Arrhythm Electrophysiol 2009;2:695-704.

138. Athey TW. A model of the temperature rise in the head due to magnetic resonance imaging procedures. Magn Reson Med 1989;9:177-84.

139. Bottomley PA, Kumar A, Edelstein WA, Allen JM, Karmarkar PV. Designing passive MRI-safe implantable conducting leads with electrodes. Med Phys;37:3828-43.

140. Viohl I, Lardo A, Tully S, Karmarkar P, Bottomley PA. The efficacy of decoupling methods to minimize RF heating due to internal conducting devices used in MRI. International Society for Magnetic Resonance in Medicine Tenth Scientific Meeting & Exhibition. Honolulu, Hawaii 2002.

141. Schaefer DJ. Health Effects and Safety of Radiofrequency Power Associated with Magnetic Resonance Procedures. In: Shellock FG, ed. *Magentic Resonance Procedures: Health Effects and Safety*, 2001:62.

142. Celik H, Sengezer N, Akin B, et al. Safe Deep Brain Stimulator MR Imaging Experiments Using Fiber Optic Current Monitoring Feedback System ISMRM 18th Scientific Meeting & Exhibition Stockholm, Sweden 2010:3897.

143. Nordbeck P, Weiss I, Ehses P, et al. Measuring RF-induced currents inside implants: Impact of device configuration on MRI safety of cardiac pacemaker leads. Magn Reson Med 2009;61:570-8.

144. Graesslin I, Weller J, Koken P, Smink J, Annighoefer B, Krueger S. Continuous Monitoring of RF-safety for Implantable MR-conditional Devices ISMRM 17th Scientific Meeting & Exhibition Honolulu, HI 2009:4793.

145. Zanchi MG, Venook R, Pauly JM, Scott GC. An optically coupled system for quantitative monitoring of MRI-induced RF currents into long conductors. IEEE Trans Med Imaging;29:169-78.

146. Overall WR, Pauly JM, Stang PP, Scott GC. Ensuring safety of implanted devices under MRI using reversed RF polarization. Magn Reson Med;64:823-33.

147. Samal AK, White CJ. Percutaneous management of access site complications. Catheter Cardiovasc Interv 2002;57:12-23.

148. Saikus CE, Lederman RJ. Interventional cardiovascular magnetic resonance imaging: a new opportunity for image-guided interventions. JACC Cardiovasc Imaging 2009;2:1321-31.

149. Swindle M. Surgery, Anesthesia, and Experimental Techniques in Swine Ames, Iowa: Iowa State University Press, 1998.

150. Flournoy WS, Mani S. Percutaneous external jugular vein catheterization in piglets using a triangulation technique. Lab Anim 2009;43:344-9.

151. Koktzoglou I, Li D, Dharmakumar R. Dephased FLAPS for improved visualization of susceptibility-shifted passive devices for real-time interventional MRI. Phys Med Biol 2007;52:N277-86.

152. McLeod KA, Houston AB, Richens T, Wilson N. Transhepatic approach for cardiac catheterisation in children: initial experience. Heart 1999;82:694-6.

153. Shim D, Lloyd TR, Cho KJ, Moorehead CP, Beekman RH, 3rd. Transhepatic cardiac catheterization in children. Evaluation of efficacy and safety. Circulation 1995;92:1526-30.

154. Johnson JL, Fellows KE, Murphy JD. Transhepatic central venous access for cardiac catheterization and radiologic intervention. Cathet Cardiovasc Diagn 1995;35:168-71.

155. Johnston TA, Donnelly LF, Frush DP, O'Laughlin MP. Transhepatic catheterization using ultrasound-guided access. Pediatr Cardiol 2003;24:393-6.

156. Levy EB, Zhang H, Lindisch D, Wood BJ, Cleary K. Electromagnetic tracking-guided percutaneous intrahepatic portosystemic shunt creation in a swine model. J Vasc Interv Radiol 2007;18:303-7.

157. Raza SA, Walser E, Hernandez A, Chen K, Marroquin S. Transhepatic puncture of portal and hepatic veins for TIPS using a single-needle pass under sonographic guidance. AJR Am J Roentgenol 2006;187:W87-91.

158. Banovac F, Levy EB, Lindisch DJ, Pearce A, Onda S, Clifford M. Feasibility of percutaneous transabdominal portosystemic shunt creation. Surg Radiol Anat 2002;24:217-21.

159. Saybasili H, Faranesh AZ, Saikus CE, Ozturk C, Lederman RJ, Guttman MA. Interventional MRI using multiple 3D angiography roadmaps with real-time imaging. J Magn Reson Imaging;31:1015-9.

160. Amin Z, Gu X, Berry JM, Titus JL, Gidding SS, Rocchini AP. Perventricular [correction of Periventricular] closure of ventricular septal defects without cardiopulmonary bypass. Ann Thorac Surg 1999;68:149-53; discussion 153-4.

161. Hsieh CH, Thomas SP, Ross DL. Direct transthoracic access to the left ventricle for catheter ablation of ventricular tachycardia. Circ Arrhythm Electrophysiol;3:178-85.

162. Semple T, McGuinness JB, Gardner H. Left heart catheterization by direct ventricular puncture. Br Heart J 1968;30:402-6.

163. Pitta SR, Cabalka AK, Rihal CS. Complications associated with left ventricular puncture. Catheter Cardiovasc Interv;76:993-7.

164. Patil S, Bieri O, Jhooti P, Scheffler K. Automatic slice positioning (ASP) for passive real-time tracking of interventional devices using projection-reconstruction imaging with echo-dephasing (PRIDE). Magn Reson Med 2009;62:935-42.

165. Strehl W, Rothgang E, Gilson W, Kirchberg KJ, Hornegger J, Lorenz C. A Passive, Image-Based Navigation Tool for Real-time MR-Guided Percutaneous Interventional Procedures ISMRM 18th Scientific Meeting & Exhibition. Stockholm, Sweden 2010:969.

166. Syms RR, Young IR, Ahmad MM, Rea M. Thin-film Catheter-Based RF Detector System. ISMRM 18th Scientific Meeting & Exhibition. Stockholm, Sweden 2010:425.

167. Anders J, SanGiorgio P, Boero G, Deligianni X, Patil S, Scheffler K. An integrated CMOS detector for MR image guided interventions ISMRM 18th Scientific Meeting & Exhibition. Stockholm, Sweden 2010:1857.

168. Woytasik M, Ginefri J-C, Raynaud J-S, et al. Characterization of flexible RF microcoils dedicated to local MRI Microsyst Technol 2007;13:1575-1580.

169. Etezadi-Amoli M, Stang P, Zanchi MG, Pauly JM, Scott GC, Kerr AB. Controlling induced currents in guidewires using parallel transmit ISMRM 18th Scientific Meeting & Exhibition. Stockholm, Sweden, 2010:777.

170. Larkman DJ, Nunes RG. Parallel magnetic resonance imaging. Phys Med Biol 2007;52:R15-55.